Title
Characterization of Substituted Radicals by Multi-Edge Femtosecond X-Ray Transient Absorption Spectroscopy

Author
YANG, ZHEYUE

Publication Date
2018

Peer reviewed|Thesis/dissertation

Characterization of Substituted Radicals by Multi-Edge Femtosecond X-Ray Transient Absorption Spectroscopy

by

Zheyue Yang

A dissertation submitted in partial satisfaction of the

requirements for the degree of

Doctor of Philosophy

in

Chemistry

in the

Graduate Division

of the

University of California, Berkeley

Committee in charge:

Professor Stephen R. Leone, Chair

Professor Daniel M. Neumark

Professor Roger Falcone

Fall 2018

Characterization of Substituted Radicals by Multi-Edge Femtosecond X-Ray Transient Absorption Spectroscopy

Abstract

Characterization of Substituted Radicals by Multi-Edge Femtosecond X-Ray Transient Absorption Spectroscopy

by

Zheyue Yang

Doctor of Philosophy in Chemistry

University of California, Berkeley

Professor Stephen R. Leone, Chair

Femtosecond x-ray transient absorption spectroscopy is used in conjunction with selective bond breaking to characterize the electronic structures of substituted radicals. By utilizing the Ã band photodissociation of iodides, a series of carbon-centered radicals is produced and their frontier molecular orbitals are probed via core-level transitions by x-ray photons produced through high harmonic generation, whose limit has been extended to 390 eV with the apparatus detailed in the second chapter.

Two types of substituted radicals are studied in this work to demonstrate substitution effects: halogenated radicals and alkyl substituted radicals. The third chapter focuses on the halogenated radicals, in particular $\cdot CH_2Cl$ and $\cdot CH_2Br$, which are produced under ultraviolet radiation of CH_2ICl and CH_2IBr, respectively. The $\cdot CH_2Cl$ radical is probed via the carbon K edge and the chlorine $L_{2,3}$ edges to reveal the electron withdrawing effect impacting different atoms in the photodissociation of CH_2ICl. Core-level transitions in $\cdot CH_2Br$ are studied in comparison to $\cdot CH_3$ and $\cdot CH_2Cl$ to understand possible stabilization of the frontier molecular orbital by π bonding and the strength of such stabilization. The fourth chapter turns to the alkyl substituted radicals, where the methyl, ethyl, isopropyl and tert-butyl radical are produced from methyl, ethyl, isopropyl and tert-butyl iodide, respectively. While the characteristic carbon 1s→σ*(C-I) transition takes place in the parent iodides at similar energies, the transition from carbon 1s to the frontier singly occupied molecular orbital differs drastically in the radicals. This can be explained by either a significant change in the carbon 1s orbital of the radicals because of methyl substitution or complications due to vibrational excitation. The results point to new directions for core-level theoretical investigations.

To my parents

Contents

List of Figures

List of Tables

Acknowledgements

Reflecting on the past five and a half years in Berkeley, first and foremost I would like to thank my advisor Professor Stephen Leone for giving me the opportunity to join his group and learn about this exciting field. Steve has been a supportive mentor all the time and guided me to think about research creatively and critically. His dedication to research as well as teaching continues to inspire me. I also appreciate Professors Richard Saykally, William Lester, Charles Harris, Daniel Neumark and Roger Falcone for taking their time to be on my qualifying exam and/or thesis committee.

The work presented in this dissertation would not have been possible without help of many other people, especially my colleagues in the Leone Group. I am grateful to Mihai Vaida who patiently taught me all the principles and fundamentals in lab and tolerated my incessant basic questions. I am also hugely indebted to Aditi Bhattacherjee, Kirsten Schnorr and Andrew Attar who were extremely welcoming and helpful when I had difficulty transitioning to new projects. Michael Epshtein and Chris Tian Xue have been amazing lab mates and I cherish the time we struggled through failure of instrument and experiments.

It has been a pleasure for me to get to know so many amazing people here, including Natalie Gibson and Lucas Carneiro who joined the Leone Group at the same time with me and survived the classes and the qualifying exam together, Denisia Popolan-Vaida, Allison Pymer, Chang-Ming Jiang, Lauren Borja, Henry Timmers, Mazyar Sabbar, Erika Warrick, Marieke Jager, Scott Cushing, Chris Kaplan, Ashley Fidler, Hung-Tzu Chang, Yuki Kobayashi, Kristina Chang, Ilana Porter, Bethany Lamoureux, Andrew Ross and Lou Barreau who were enlightening in the science discussions we had as well as generously lent me their lab tools from time to time.

Lastly, I want to express my gratitude to my parents who has been encouraging and supporting me unconditionally. There were numerous times over the years I was feeling hopeless and they gave me the strength to hold on and look forward.

Chapter 1. Introduction to Core Level Radical Spectroscopy

1.1 Radicals

Radicals, the group of molecular entities with an unpaired electron,[1] hold the key to numerous chemical reactions and thus have long been intriguing to chemists. They form important intermediates in chemical reactions and their stability can greatly impact reaction mechanisms and branching pathways.[2-5] Free radicals, with few exceptions,[6-7] are in general difficult to maintain for investigation, due to their reactivity and short lifetimes. Hence, fully understanding the geometry and the electronic structures of radicals has been an obstacle, especially with heavily substituted radicals.

The frontier molecular orbital of a radical is characterized by a half-filled orbital, or singly occupied molecular orbital (SOMO). In the simplest carbon-containing radical $\cdot CH_3$, which has a planar structure, its SOMO resembles the atomic 2p orbital of carbon as shown in Figure 1.1. However, as the methyl radical is substituted, its planar geometry may change as well as the substitution can greatly affect the orbital character of the SOMO. Several factors influencing the SOMO include resonance stabilization, hyperconjugation[8] and π backbonding[9].

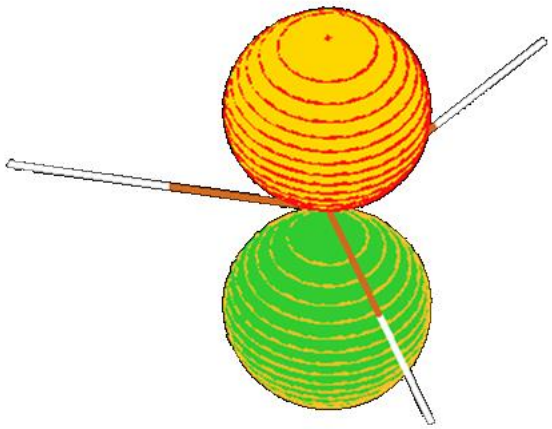

Figure 1.1 The frontier singly occupied molecular orbital (SOMO) of the methyl radical ($\cdot CH_3$), which resembles the atomic carbon 2p orbital.

Two types of substituted radicals are studied in this dissertation: one is halogenated radicals and the other, alkyl substituted radicals.

Halogenated radicals are common intermediates and byproducts in combustion and atmospheric processes. For example, the CH_2Cl radical has been proposed, with various mechanisms, to be an inhibitor in the combustion of chlorinated fuels,[10] an origin of soot formation,[11] as well as key to stratospheric processes such as ozone depletion,[12] in addition to marine decomposition where boundary aqueous layers react with these radicals to a non-negligible extent.[13]

Alkyl substitution is another fundamental class of substituents. From a planar geometry in $\cdot CH_3$ to a slightly non-planar geometry in tert-butyl radical, the increasing stability has invoked research into their structures, ionization energies and valence absorption spectra.[14-16] However, results are often convoluted with higher-lying states in the valence shell and complication within the ionic states. Therefore it is crucial to resolve how the SOMOs of the radicals are changed by substitution from a fundamental perspective, and core-level spectroscopy will provide such insights.

1.2 Core Level Spectroscopy

With the advent of synchrotron facilities[17-18] and table top extreme ultraviolet (XUV)/x-ray sources,[19-20] core-level spectroscopy has become a novel tool to study electronic structures and molecular dynamics.[21-22] Core-level transitions take place in inner shells whose nomenclature is based on the principle quantum number of the core orbital, e.g. K edge for 1s, L_1 for 2s, $L_{2,3}$ for 2p and $M_{4,5}$ for 3d. As the wavefunctions of core orbitals are more localized, their energy levels are much more separated than those of the valence orbitals. Table 1.1 lists some common core shell energy levels[23-25] that will be discussed in this dissertation. It is obvious that each atom has distinct core shell energy levels and therefore in core level spectroscopy the behavior of different atoms can be easily distinguished.

Table 1.1 Summary of relevant atomic core levels.

Atom	Edge	Energy (eV)
C	K	~285 eV
Cl	L_1	~270 eV
Cl	$L_{2,3}$	~200 eV
N	K	~400 eV
Br	$M_{4,5}$	~75 eV

Apart from energy separations pinpointing element specificity, core-level transitions also carry abundant information about the chemical environment of each atom such as its oxidation state and spin state.[26] In core-level absorption spectroscopy, the technique that will be utilized throughout this dissertation, an XUV/x-ray photon excites an electron from a core orbital to various vacant valence orbitals, as schematically shown in Figure 1.2(a). The absorption energy with its cross section embeds the information of not only the core shell, but also the valence shell. Transitions from the same core orbital will render relative orderings of unoccupied valence molecular orbitals while transitions to the same vacant molecular orbital detail the difference among the core orbitals.

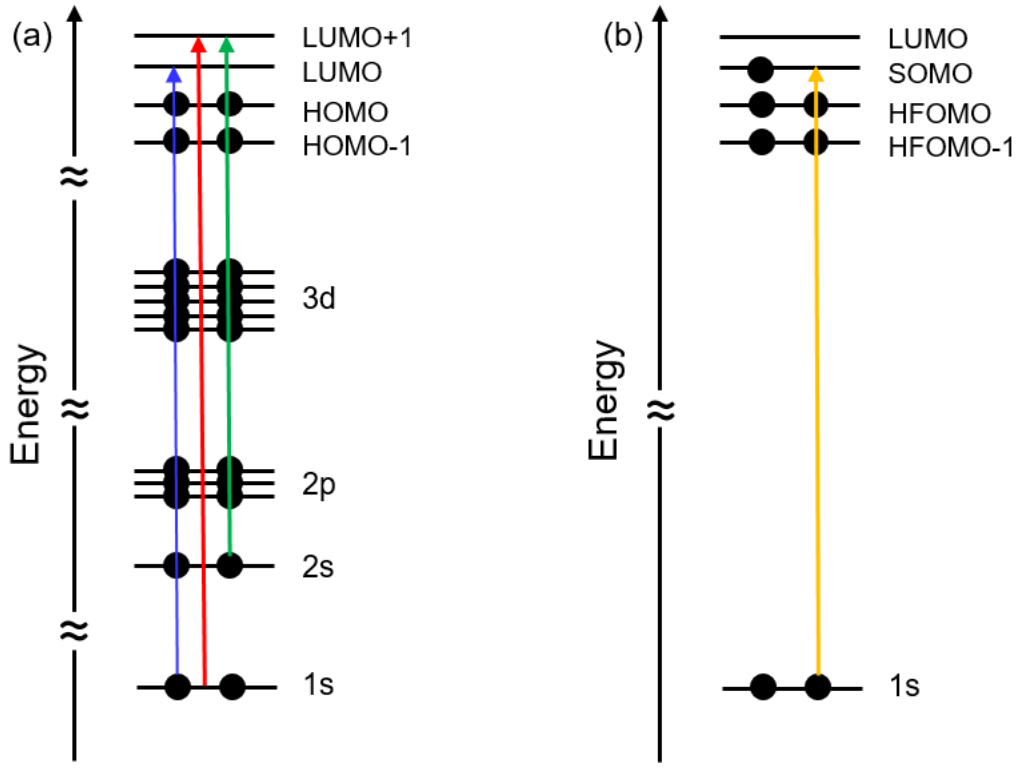

Figure 1.2 (a) A generic schematic diagram showing various possibilities of core-level transitions represented by the blue, red and green arrow. (b) A generic diagram for carbon K edge radical absorption spectroscopy where the orange arrow represents the transition expected to be observed in radicals. HOMO is abbreviated for highest occupied molecular orbital, LUMO lowest unoccupied molecular orbital, SOMO singly occupied molecular orbital and HFOMO highest fully occupied molecular orbital.

For radicals with the unpaired electron centered on carbon, the core-level absorption spectroscopy at the carbon K edge is especially advantageous, since it is capable of probing the SOMO directly from the carbon 1s orbital, as drawn out in Figure 1.2 (b). The orbital selection rules also favor transitions from carbon 1s to orbitals with p character, which allows easy detection of radicals whose SOMO is largely carbon 2p in character.

1.3 Radicals Generated Through Photodissociation

Pyrolysis has been widely used to generate radicals where radicals are produced through thermal decomposition of a particular molecule at elevated temperatures, e.g. $\cdot CH_3$ can be produced through flash pyrolysis of azomethane,[27] tert-butyl radical through pyrolysis of alkyl nitrites[16], etc. However, each radical will require a distinct molecule to decompose from and the conditions vary with materials.

In this work, photodissociation is used as the means to produce radicals. It has been well established that the A band photodissociation of iodides will lead to the carbon-iodine bond

breaking.[28-30] Figure 1.3 shows the uniform broad absorption bands across different iodides.[31-35] With ultraviolet (UV) radiation centered at 260-270 nm, one electron is promoted from the non-bonding iodine 5p orbital to a σ*(C-I) antibonding orbital, leading to repulsive states and photodissociation into a radical and an iodine atom or its spin excited counterpart:

$$\mathbf{R\text{-}I \xrightarrow{UV} R + I(^2P_{3/2})/I^*(^2P_{1/2})}$$

A generic potential energy diagram of this direct photodissociation mechanism of iodides is depicted in Figure 1.4.[36] By changing the functional group attached to the iodine atom, desired radicals can be produced, e.g. CH_2ICl will lead to photodissociation into CH_2Cl, tert-butyl iodide into tert-butyl radical.

Moreover, this is a *selective* bond breaking process, as the UV radiation is not sufficient to trigger C-C or C-H bond breaking. In dihalogenmethanes, such as CH_2ICl and CH_2IBr, the C-Cl[37-38] and the C-Br bond breaking wavelengths[25, 28] are also considerably away from the C-I bond breaking wavelength, allowing the C-I bond breaking to be the predominant pathway.

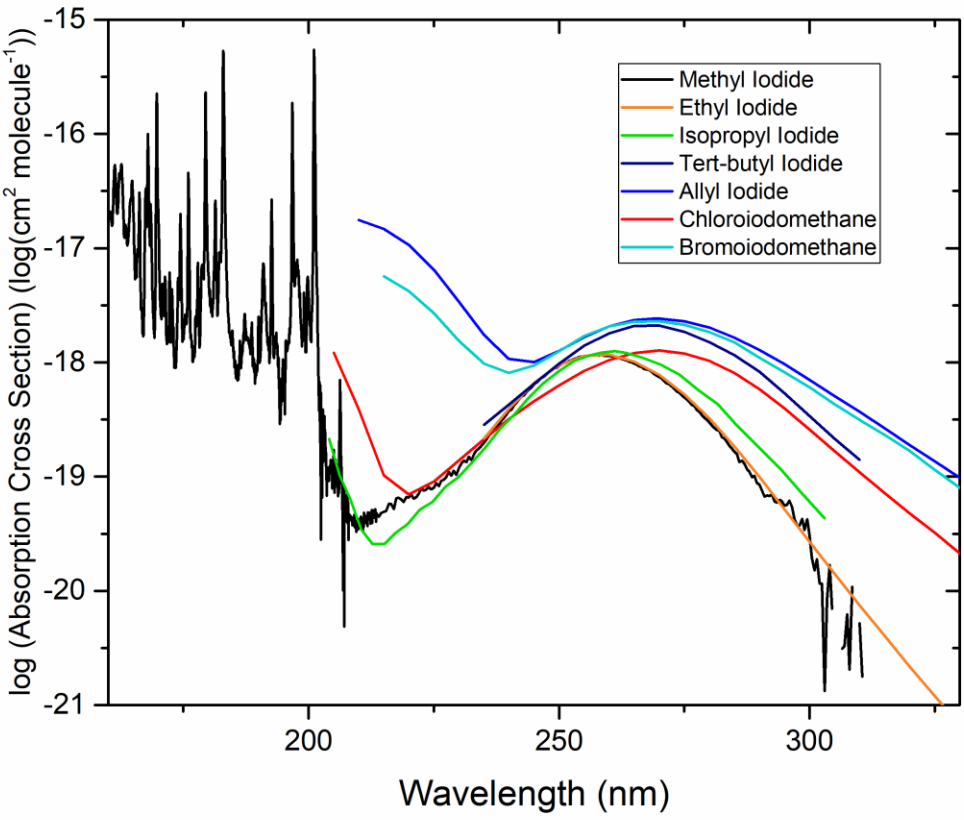

Figure 1.3 The ultraviolet absorption spectra of various iodides.[31-35] The broad band peaking at 260-270 nm corresponds to the A band photodissociation of iodides.

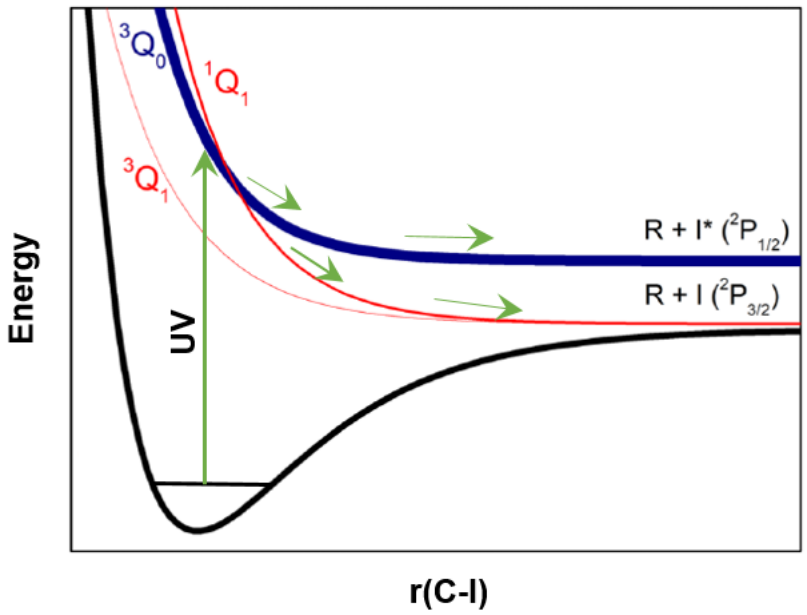

Figure 1.4 A generic potential energy diagram of iodide photodissociation. With UV excitation, an electron is promoted from the ground state to the $^3Q_0$ state (or its equivalent). A portion of the wavepacket will leak through the conical intersection into $^1Q_1$. Both states are repulsive and lead to final dissociation into a radical. Adapted from reference 36.

1.4 Pump Probe Technique and Transient Absorption Spectroscopy

To study the core-level spectroscopy of radicals, a femtosecond pump probe technique is used. A first short UV pulse is used to initiate the photodissociation process of interest and a second XUV/x-ray pulse, at a precisely-controlled time delay, is used to monitor the response of the system. With the femtosecond technique implemented in this dissertation, the two pulses are both on the 100-femtosecond (fs) timescale, close to the photodissociation timescale of iodides. Therefore it is well suited to follow the photodissociation dynamics and probe radicals formed immediately after the photodissociation reaction is complete. Limited by the XUV/x-ray photon flux, the transient absorption technique is employed instead of a photoelectron technique, as photoelectron techniques rely more on absolute photon flux, whereas absorption techniques focus on the change in photon flux.

In the core-level absorption experiments described in this dissertation, an iodide is first probed with the XUV/x-ray radiation in order to observe the electronic structure of the parent molecule before photodissociation. Characteristically, a C(1s)→σ*(C-I) transition is observed, as the σ*(C-I) orbital is the lowest unoccupied molecular orbital (LUMO) in the parent molecule. During the photodissociation process, an electron is promoted by the UV radiation from the iodine 5p to the σ*(C-I) orbital, i.e. σ*(C-I) becomes half-filled instead of fully unoccupied, depleting the transition probability of C(1s)→σ*(C-I). After photodissociation, the σ*(C-I) orbital is broken and a SOMO is formed centered on carbon, which can consequently be observed as a new feature. An overview of changes in electronic configuration and their implications for core-level spectroscopy is demonstrated in Figure 1.5.

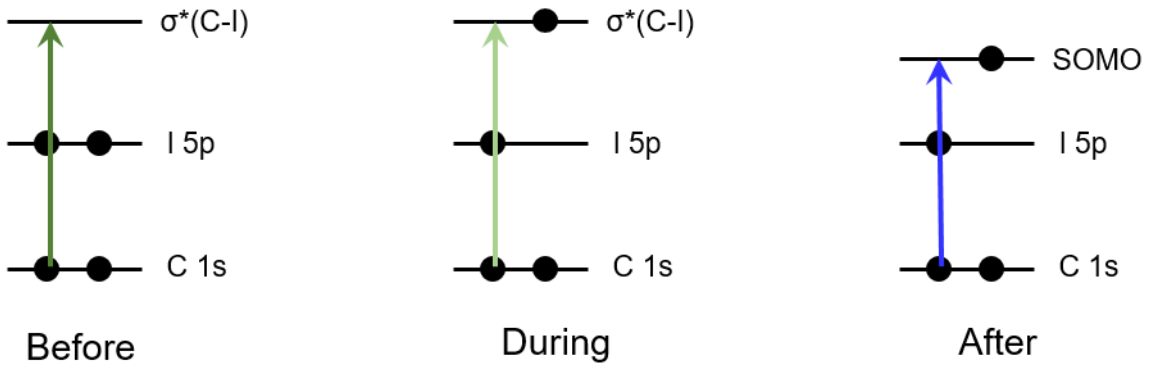

Figure 1.5 An illustration of an iodide photodissociation reaction observed at the carbon K edge.

The following chapters will discuss first the instrument to conduct such core-level absorption experiments (Chapter 2) and then the use of the technique to reveal fundamental factors in organic chemistry, such as the electron withdrawing effect and π backbonding in halogenated radicals (Chapter 3) and hyperconjugation in alkyl substituted radicals (Chapter 4).

1.5 Bibliography

1. Muller, P., Glossary of Terms Used in Physical Organic-Chemistry. *Pure Appl Chem* **1994,** *66* (5), 1077-1184.
2. Studer, A.; Curran, D. P., Catalysis of Radical Reactions: A Radical Chemistry Perspective. *Angew Chem Int Edit* **2016,** *55* (1), 58-102.
3. Pilling, M. J., Radical-radical reactions. *Annual Review of Physical Chemistry* **1996,** *47*, 81-108.
4. Cunningham, M. F., Controlled/living radical polymerization in aqueous dispersed systems. *Prog Polym Sci* **2008,** *33* (4), 365-398.
5. Porter, N. A.; Caldwell, S. E.; Mills, K. A., Mechanisms of Free-Radical Oxidation of Unsaturated Lipids. *Lipids* **1995,** *30* (4), 277-290.
6. Gomberg, M., An instance of trivalent carbon triphenylmethyl. *J Am Chem Soc* **1900,** *22* (11), 757-771.
7. Hicks, R. G., What's new in stable radical chemistry? *Org Biomol Chem* **2007,** *5* (9), 1321-1338.
8. Fernandez, I.; Frenking, G., Direct estimate of the strength of conjugation and hyperconjugation by the energy decomposition analysis method. *Chem-Eur J* **2006,** *12* (13), 3617-3629.
9. Frenking, G.; Fau, S.; Marchand, C. M.; Grutzmacher, H., The pi-donor ability of the halogens in cations and neutral molecules. A theoretical study of AX_3^+, AH_2X^+, YX_3, and YH_2X (A=C, Si, Ge, Sn, Pb; Y=B, Al, Ga, In, Tl; X=F, Cl, Br, I). *J Am Chem Soc* **1997,** *119* (28), 6648-6655.

10. Hung, S. L.; Pfefferle, L. D., A Flow Tube Kinetics Study of Methyl-Chloride Oxidation. *Combust Sci Technol* **1993,** *87* (1-6), 91-107.
11. Violi, A.; D'Anna, A.; D'Alessio, A., A modeling evaluation of the effect of chlorine on the formation of particulate matter in combustion. *Chemosphere* **2001,** *42* (5-7), 463-471.
12. Molina, M. J.; Rowland, F. S., Stratospheric Sink for Chlorofluoromethanes - Chlorine Atomic-Catalysed Destruction of Ozone. *Nature* **1974,** *249* (5460), 810-812.
13. Enami, S.; Hoffmann, M. R.; Colussi, A. J., Halogen Radical Chemistry at Aqueous Interfaces. *J Phys Chem A* **2016,** *120* (31), 6242-6248.
14. Dyke, J.; Ellis, A.; Jonathan, N.; Morris, A., Vacuum Ultraviolet Photoelectron-Spectroscopy of Transient Species .18. The Cyclopropyl, Isopropyl and Normal-Propyl Radicals. *J Chem Soc Farad T 2* **1985,** *81* (Oct), 1573-1586.
15. Dyke, J. M.; Ellis, A. R.; Keddar, N.; Morris, A., A Reinvestigation of the 1st Band in the Photoelectron-Spectrum of the Ethyl Radical. *J Phys Chem-Us* **1984,** *88* (12), 2565-2569.
16. Houle, F. A.; Beauchamp, J. L., Photoelectron-Spectroscopy of Methyl, Ethyl, Isopropyl, and Tert-Butyl Radicals - Implications for the Thermochemistry and Structures of the Radicals and Their Corresponding Carbonium-Ions. *J Am Chem Soc* **1979,** *101* (15), 4067-4074.
17. Chen, L. X.; Zhang, X.; Shelby, M. L., Recent advances on ultrafast X-ray spectroscopy in the chemical sciences. *Chem Sci* **2014,** *5* (11), 4136-4152.
18. Schoenlein, R. W.; Chattopadhyay, S.; Chong, H. H. W.; Glover, T. E.; Heimann, P. A.; Shank, C. V.; Zholents, A. A.; Zolotorev, M. S., Generation of femtosecond pulses of synchrotron radiation. *Science* **2000,** *287* (5461), 2237-2240.
19. Popmintchev, T.; Chen, M. C.; Bahabad, A.; Gerrity, M.; Sidorenko, P.; Cohen, O.; Christov, I. P.; Murnane, M. M.; Kapteyn, H. C., Phase matching of high harmonic generation in the soft and hard X-ray regions of the spectrum. *P Natl Acad Sci USA* **2009,** *106* (26), 10516-10521.
20. Popmintchev, T.; Chen, M. C.; Popmintchev, D.; Arpin, P.; Brown, S.; Alisauskas, S.; Andriukaitis, G.; Balciunas, T.; Mucke, O. D.; Pugzlys, A.; Baltuska, A.; Shim, B.; Schrauth, S. E.; Gaeta, A.; Hernandez-Garcia, C.; Plaja, L.; Becker, A.; Jaron-Becker, A.; Murnane, M. M.; Kapteyn, H. C., Bright Coherent Ultrahigh Harmonics in the keV X-ray Regime from Mid-Infrared Femtosecond Lasers. *Science* **2012,** *336* (6086), 1287-1291.
21. Attar, A. R.; Bhattacherjee, A.; Pemmaraju, C. D.; Schnorr, K.; Closser, K. D.; Prendergast, D.; Leone, S. R., Femtosecond x-ray spectroscopy of an electrocyclic ring-opening reaction. *Science* **2017,** *356* (6333), 54-58.
22. Pertot, Y.; Schmidt, C.; Matthews, M.; Chauvet, A.; Huppert, M.; Svoboda, V.; von Conta, A.; Tehlar, A.; Baykusheva, D.; Wolf, J. P.; Worner, H. J., Time-resolved x-ray absorption spectroscopy with a water window high-harmonic source. *Science* **2017,** *355* (6322), 264-+.
23. Hitchcock, A. P.; Brion, C. E., Inner-Shell Excitation and Exafs-Type Phenomena in Chloromethanes. *J Electron Spectrosc* **1978,** *14* (6), 417-441.
24. Hitchcock, A. P.; Brion, C. E., Inner Shell Excitation of CH_3F, CH_3Cl, CH_3Br and CH_3I by 2.5 Kev Electron-Impact. *J Electron Spectrosc* **1978,** *13* (3), 193-218.
25. Attar, A. R.; Piticco, L.; Leone, S. R., Core-to-valence spectroscopic detection of the CH_2Br radical and element-specific femtosecond photodissociation dynamics of CH_2IBr. *J Chem Phys* **2014,** *141* (16).
26. Stöhr, J., *NEXAFS Spectroscopy*. Springer: 1996.

27. Alagia, M.; Lavollee, M.; Richter, R.; Ekstrom, U.; Carravetta, V.; Stranges, D.; Brunetti, B.; Stranges, S., Probing the potential energy surface by high-resolution x-ray absorption spectroscopy: The umbrella motion of the core-excited CH_3 free radical. *Phys Rev A* **2007,** *76* (2).
28. Murillo-Sánchez, M. L.; Marggi Poullain, S.; Bajo, J. J.; Corrales, M. E.; González-Vázquez, J.; Solá, I. R.; Bañares, L., Halogen-atom effect on the ultrafast photodissociation dynamics of the dihalomethanes CH2ICl and CH2BrI. *Phys Chem Chem Phys* **2018,** *20* (32), 20766-20778.
29. Phillips, D. L.; Lawrence, B. A.; Valentini, J. J., Substituent Effects on Gas-Phase Photodissociation Dynamics - Resonance Raman-Spectra of Ethyl Iodide, Isopropyl Iodide, and Tert-Butyl Iodide. *J Phys Chem-Us* **1991,** *95* (23), 9085-9091.
30. Kim, Y. S.; Kang, W. K.; Kim, D. C.; Jung, K. H., Photodissociation of tert-butyl iodide at 277 and 304 nm: Evidence for direct and indirect dissociation in A-band photolysis of alkyl iodide. *J Phys Chem A* **1997,** *101* (41), 7576-7581.
31. Rattigan, O. V.; Shallcross, D. E.; Cox, R. A., UV absorption cross-sections and atmospheric photolysis rates of CF_3I, CH_3I, C_2H_5I and CH_2ICl. *J Chem Soc Faraday T* **1997,** *93* (16), 2839-2846.
32. Eden, S.; Limao-Vieira, P.; Hoffmann, S. V.; Mason, N. J., VUV spectroscopy of CH_3Cl and CH_3I. *Chem Phys* **2007,** *331* (2-3), 232-244.
33. Boschi, R. A.; Salahub, D. R., Far Ultraviolet-Spectra of Some Branched-Chain Iodo-Alkanes, Iodo-Cyclo-Alkanes, Fluoro-Iodo-Alkanes and Iodo-Alkenes. *Mol Phys* **1972,** *24* (4), 735-&.
34. Phillips, D. L.; Myers, A. B.; Valentini, J. J., Investigation of Solvation Effects on Short-Time Photodissociation Dynamics of Alkyl Iodides. *J Phys Chem-Us* **1992,** *96* (5), 2039-2044.
35. Atkinson, R.; Baulch, D. L.; Cox, R. A.; Crowley, J. N.; Hampson, R. F.; Hynes, R. G.; Jenkin, M. E.; Rossi, M. J.; Troe, J.; Wallington, T. J., Evaluated kinetic and photochemical data for atmospheric chemistry: Volume IV - gas phase reactions of organic halogen species. *Atmos Chem Phys* **2008,** *8* (15), 4141-4496.
36. Bhattacherjee, A.; Attar, A. R.; Leone, S. R., Transition state region in the A-Band photodissociation of allyl iodide-A femtosecond extreme ultraviolet transient absorption study. *J Chem Phys* **2016,** *144* (12).
37. Murillo-Sanchez, M. L.; Poullain, S. M.; Gonzalez-Vazquez, J.; Corrales, M. E.; Balerdi, G.; Banares, L., Femtosecond photodissociation dynamics of chloroiodomethane in the first absorption band. *Chem Phys Lett* **2017,** *683*, 22-28.
38. Senapati, D.; Kavita, K.; Das, P. K., Photodissociation dynamics of CH_2ICl at 222, 236, 266, 280, and-304 nm. *J Phys Chem A* **2002,** *106* (36), 8479-8482.

Chapter 2. Characterization and Optimization of a Table-Top UV-Pump X-Ray-Probe Instrument

2.1 Introduction

To perform core-level spectroscopic studies of radicals, an ultraviolet-pump soft x-ray probe apparatus is needed where the ultraviolet light source facilitates selective bond breaking ("pump") and the soft x-ray source detects electronic excitation from the core levels of radicals ("probe"). This chapter addresses the working principles behind such an apparatus and key factors in improving its performance. Section 2.2 discusses the probe, section 2.3 describes the pump and section 2.4 lays out the data acquisition methods and characterizes the spectral and temporal resolution.

2.2 The Probe – Soft X-Ray by High Harmonic Generation (HHG)

2.2.1 General Description of the Three-Step Model and the Cutoff Equation

While large facilities such as synchrotrons at various sites have provided opportunities to conduct x-ray-related experiments,[1-3] table-top x-ray sources utilizing high harmonic generation have come into the spotlight[4-6] as they are much more easily accessible and have more flexibility in choosing the x-ray wavelength of interest.

The mechanism of high harmonic generation has been explained semi-classically by Paul Corkum[7] using a three-step model. (1) The electric field of a short-pulse laser is strong enough to tunnel ionize gaseous atoms. (2) The emitted electron propagates in the laser field, gaining kinetic energy. It travels away from the parent atom in the first half cycle and back in the second half. (3) The electron recombines with the parent atom with a small probability[8-9] and the energy is conserved by emitting a photon whose energy is given by:

$$E_{HHG} = IP + 3.17U_p = IP + 3.17\,\frac{e^2{E_0}^2}{4m_e{\omega_0}^2} \qquad \text{Equation 2.1}$$

where IP is the ionization potential of the gaseous atom, U_p the ponderomotive energy corresponding to how much kinetic energy the electron has gained in step (2), e the electron charge, E_0 amplitude of the laser field, m_e the electron effective mass, and ω_0 the driving laser frequency.

By inspection of Equation 2.1, it is obvious that the HHG cutoff energy is dependent on the ionization potential of the gaseous atom, the intensity and the frequency of the driving laser. Therefore to achieve high HHG photon energies, not only a gas medium with higher ionization potential is required, but also longer driving wavelength and high intensity. In this dissertation, all the HHG processes use helium as it has the highest ionization potential among all noble gases. Moreover, a tunable optical parametric amplifier is used to convert the 800 nm output of a Ti:Sapphire laser into 1300-1600 nm with high intensity, as previous tabletop HHG sources[10-11] directly using 800 nm to drive HHG have been shown to have a cutoff energy well below the carbon K (1s) edge.

According to the three-step model, the HHG process occurs every half cycle and different orders of high harmonics are emitted in a burst. Therefore for best high harmonic generation flux, phase matching conditions need to be achieved, i.e. the fundamental laser field constructively interferes with the HHG field so that the fundamental and the higher orders of harmonic travel coherently within the gas medium. Several factors control the phase mismatch, including atomic dispersion, plasma dispersion and waveguide dispersion, all of which depend on the refractive index of the respective frequency in the gas medium. Additionally, atomic dispersion and plasma dispersion are related to neutral gas density and plasma density, which are affected by the pressure of the gas medium and the intensity of the driving laser. Waveguide dispersion is influenced by focusing conditions.[4, 12] In summary, by tuning the pressure of helium and focusing conditions, phase mismatch can be minimized to obtain the highest HHG flux and to approach the theoretical cutoff energy given in Equation 2.1.

2.2.2 Optimization of the HHG Source in the Soft X-Ray Regime

2.2.2.1 A Brief Description of HHG Beamline Components

Following the principles of high harmonic generation as described above, an experimental apparatus capable of generating HHG photons in the range of 150-390 eV has been assembled. The system consists of two parts: (1) the commercial laser system delivering the fundamental driving frequency and (2) the home built beamline for high harmonic generation.

(1) The commercial laser system is composed of a MaiTai SP oscillator (purchased from Spectra-Physics) producing 35-fs near infrared pulses centered at 800 nm with a 60 nm bandwidth, a Spitfire Ace amplifier (purchased from Spectra-Physics) outputting 35-fs 800 nm pulses with a 40 nm bandwidth and a tunable high power traveling-wave optical parametric amplifier of superfluorescence (TOPAS, purchased from Light Conversion) converting 800 nm to 1300-1600 nm using amplification of white light generation. The amplifier is seeded by the oscillator and pumps the TOPAS. The typical parameters of the laser elements mentioned above are summarized in Table 2.1.

Table 2.1 Summary of the parameters of each laser element.

Laser Element	Repetition Rate	Wavelength	Ave. Power
MaiTai SP	42.41 MHz	800 nm	650 mW
Spitfire Ace	1 kHz	800 nm	12 W
TOPAS (signal)[a]	1 kHz	1320 nm	2.6 W
TOPAS (idler)	1 kHz	2030 nm	2.4 W

a. Note that the TOPAS is pumped by the 800 nm amplifier. Thus the wavelengths of the signal and the idler follow the relation: $1/800\ \text{nm} = 1/\lambda(\text{signal}) + 1/\lambda(\text{idler})$. The TOPAS outputs the highest power at 1320 nm and decreases over the spectral range of 1320 nm – 1600 nm.

Properties of the laser system delivering the fundamental driving pulse are crucial to the stability and coverage of HHG. The output of the TOPAS defines the fundamental driving frequency. It is highly dependent on the beam mode and pulse duration out of the Spitfire amplifier.

The Spitfire amplifier utilizes the stretching-regenerative amplification-compression scheme put forward by Mourou and Strickland.[13] In this scheme, one optical element of particular importance is the compression grating. Its position largely determines the spectral coverage as well as pulse duration of the amplifier. Figure 2.1 is an example showing the spectrum before and after the laser beam hits the compression grating and the effect of rotating the grating by a small angle (<0.5°). It is very clear that a small angle of rotation will lead to loss or addition of spectral coverage and hence longer or shorter pulse duration. To ensure the broadest spectral coverage and the shortest pulse duration, it is important to rotate the compression grating so that the spectrum after the compression grating resembles the spectrum before.

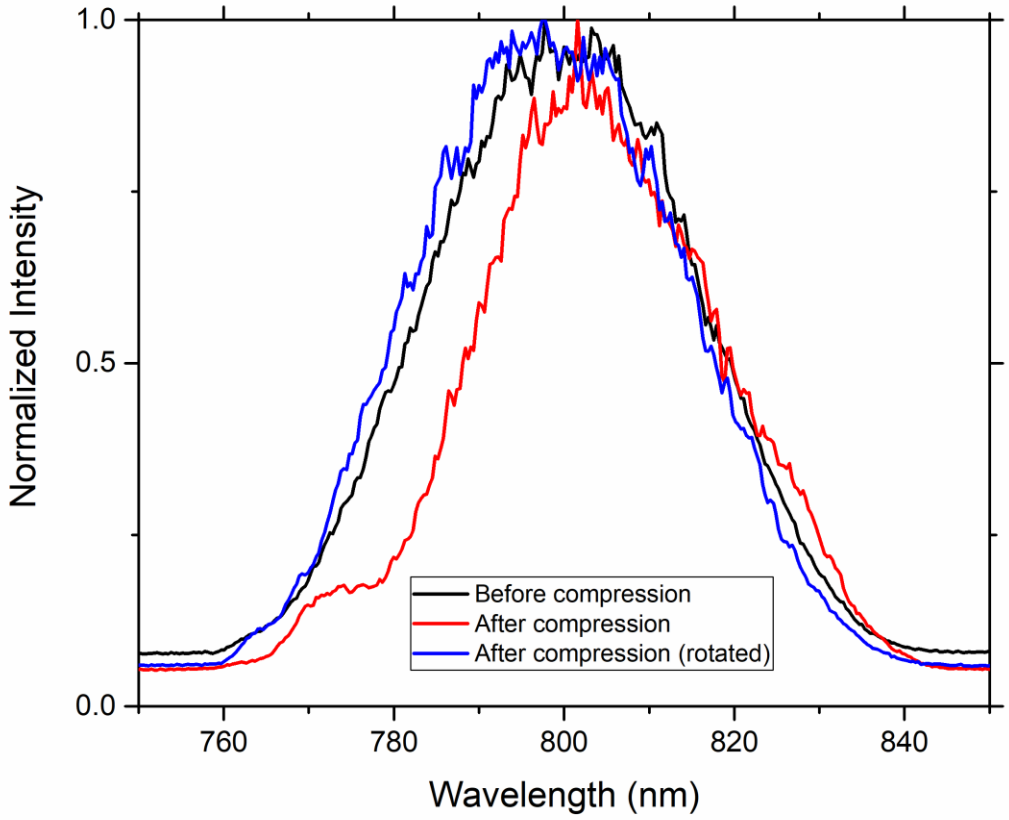

Figure 2.1 An example of the spectrum before and after the laser beam hits the compression grating and the effect of rotating the grating by a small angle (<0.5°). The red line leads to 0.3 W of loss in TOPAS output power (signal+idler).

(2) The beam out of the TOPAS is then focused by a lens into the homebuilt beamline consisting of multiple vacuum chambers outlined in Figure 2.2[14]; the main parts are a differentially pumped semi-infinite gas cell[15] filled with 700-2000 Torr of helium, a 100 nm thick aluminum filter that blocks the residual infrared beam and transmits the soft x-ray, a toroidal mirror (TM) to focus the soft x-ray, a flowing gas cell containing any target gas of interest, an extreme ultraviolet

(XUV)/soft x-ray diffraction grating (Hitachi 001-0659, 1200 lines/mm) with an incidence angle of 87° and a PIXIS charged-couple device (CCD) camera chip with 1340×400 pixels where each pixel occupies 20 microns.

A 40-cm lens is chosen to focus the 1320 nm beam whose maximum average power generated by the TOPAS is 2.6 W. As the power decreases over longer wavelengths out of TOPAS, a lens with a shorter focal distance can be used to produce more peak intensity of the pulses, such as 30 cm, to achieve higher x-ray photon energies as shown in the following section.

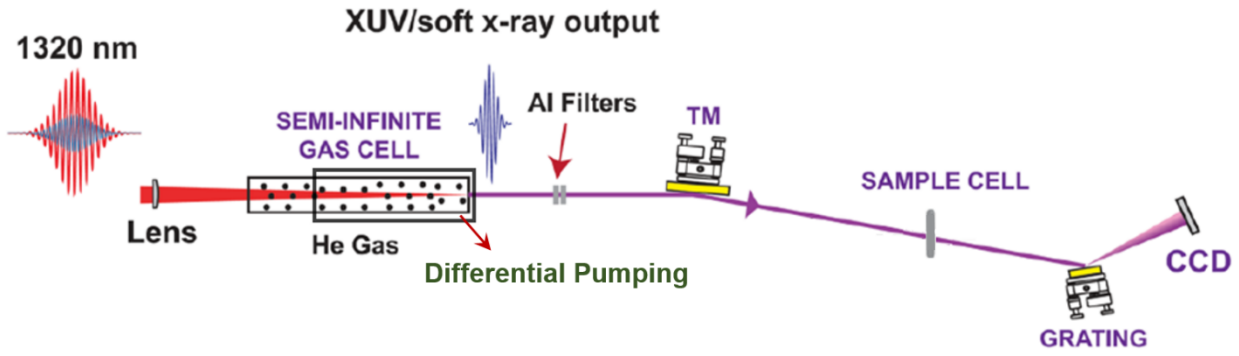

Figure 2.2 A schematic diagram of the homebuilt beamline. Adapted from reference 14.

2.2.2.2 Experimental Parameters to Optimize for Best HHG Coverage and Flux

(1) The quality of helium plays a significant role. The purer the helium gas is, the higher the HHG cutoff energy is. Two different purities of helium have been tested out under same experimental conditions, one with 99.995% (from Liquid Air) and one with 99.999% (from Praxair) and the results are demonstrated in Figure 2.3. It is very clear that the 99.999% helium gas produces higher HHG flux as well as higher cutoff energy.

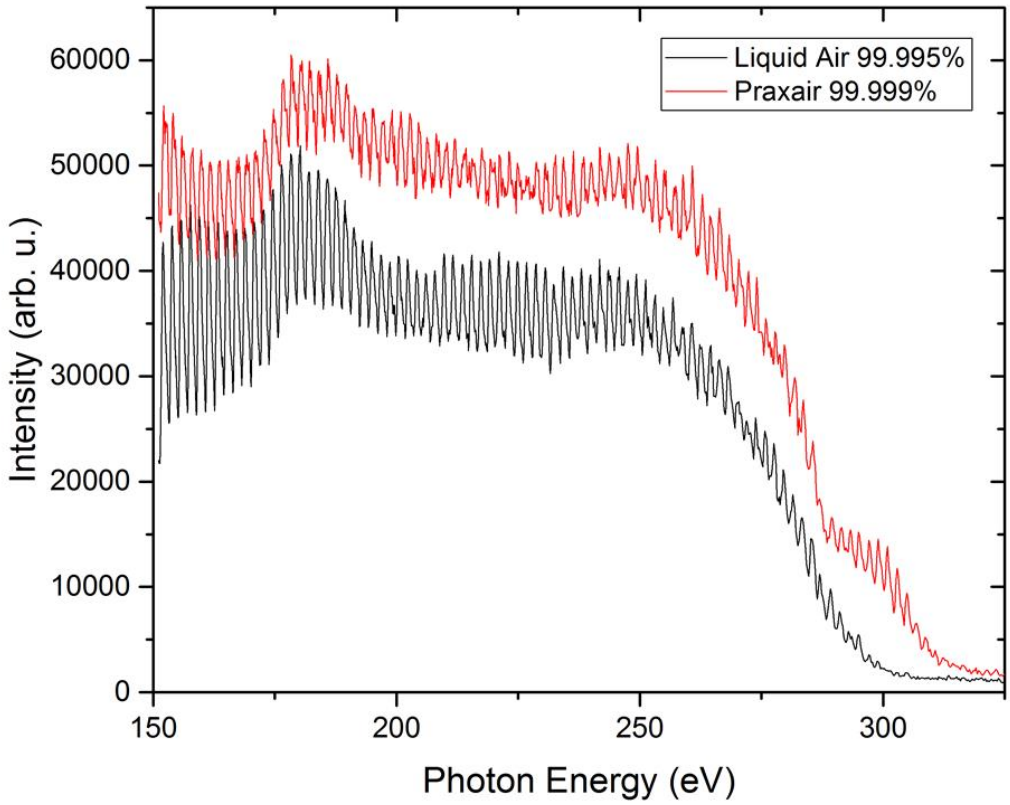

Figure 2.3 The effect of helium gas purity in high harmonic generation where two different purities of He have been used. This demonstrates that the purer the gas is, the higher the HHG cutoff energy is.

(2) According to the cutoff equation, the cutoff energy is related to the driving frequency where the higher photon energy cutoff favors longer driving wavelengths. While longer wavelengths from the TOPAS are delivered with lower intensity, a lens with shorter focal distance, i.e. 30 cm has been used to compensate for this factor. This changes the overall focusing condition and in turn phase matching. Therefore different helium pressures have been used to find the highest cutoff energy that can be achieved with each combination of lens and wavelength. Figure 2.4 compares the highest photon energy under each condition. With a fundamental frequency of 1320 nm, the highest HHG cutoff is ~310 eV while with 1470 nm, the highest cutoff is ~350 eV. The cutoff approaches 390 eV when the driving frequency is 1570 nm. This result clearly shows that by tuning to longer driving frequency, the HHG cutoff energy is significantly extended.

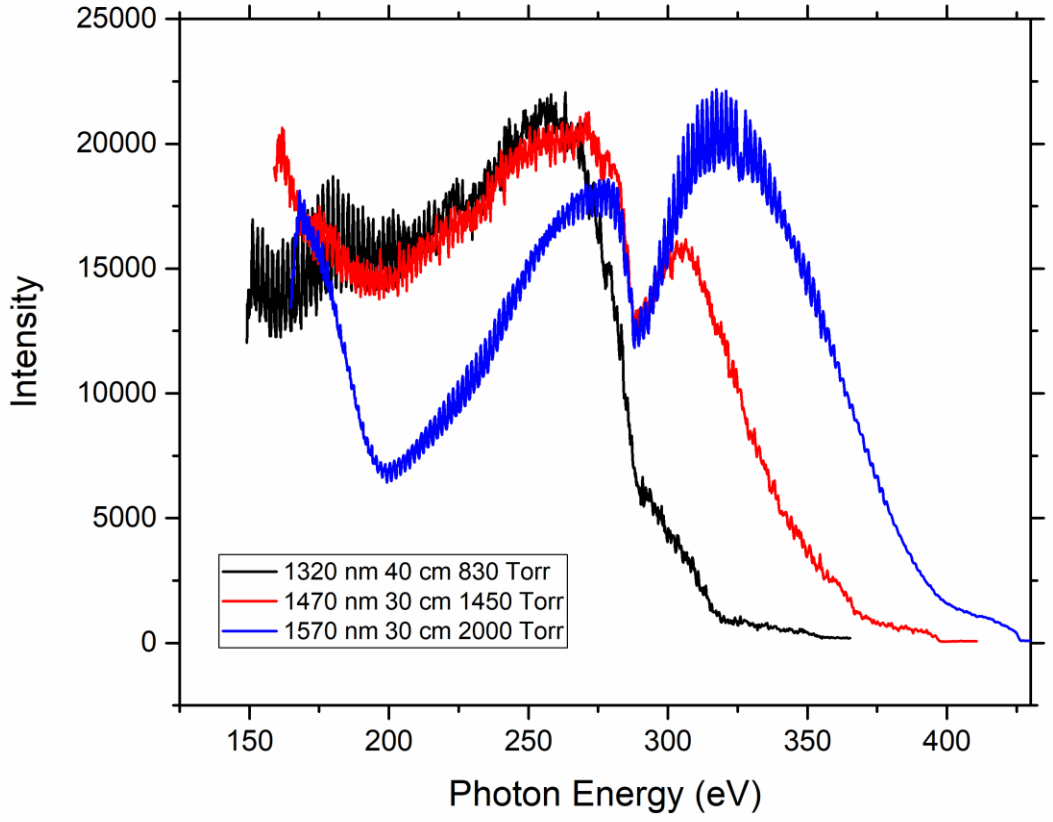

Figure 2.4 The different high harmonic generation cutoffs that can be achieved with different combinations of lens, fundamental driving laser frequency and helium pressure. This shows that the longer the driving frequency is, the higher the cutoff energy will be, following the energy cutoff equation.

2.3 The Pump – Ultraviolet Source by Third Harmonic Generation (THG)

For pump-probe experiments, the output of the 12 mJ pulses, 800 nm-centered, 1 kHz repetition rate, 35-fs from the Ti:Sapphire femtosecond laser is split into two branches in a 9:1 ratio. The 10% branch is used to produce the third harmonic generation with two non-linear crystals to generate ultraviolet pulses. Two schemes have been tested out for third harmonic generation, one using Type II Barium Borate (BBO) crystal and the other using Type I BBO crystal which requires an additional waveplate. The two schemes are shown in Figure 2.5. With a 0.2 mm thick Type II BBO crystal, the highest UV pulse energy is 35 µJ while the 0.3 mm Type I BBO crystal boosts the UV pulse energy up to 100 µJ, opening up possibilities to study molecular behavior under strong UV field, e.g. multiphoton effects and strong field ionization. [16-17] The central wavelength from this third harmonic generator is tunable from 268.3 to 269.0 nm by changing the orientation of the BBO crystals. The bandwidth is ~1.8 nm as shown in Figure 2.6.

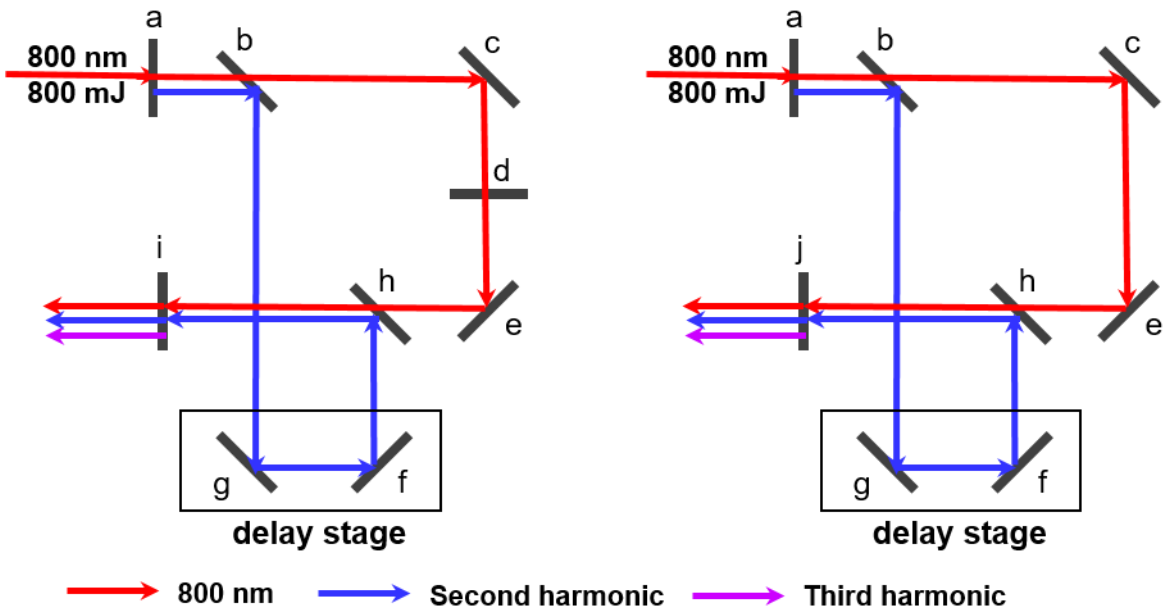

Notes: a: Type I BBO for second harmonic generation, b, h: beam splitter, c, e: 800 nm high reflector, d: 800 nm half waveplate, f, g: 400 nm high reflector, i: Type I BBO (0.3 mm) for third harmonic generation, j: Type II BBO (0.2 mm) for third harmonic generation

Figure 2.5 Two schemes of third harmonic generation. The left scheme uses a Type I BBO crystal for THG, which requires an additional wave plate (element d) and delivers 100 µJ maximum UV pulse energy. The right scheme uses Type II BBO crystal for THG and delivers 35 µJ maximum UV pulse energy.

The ultraviolet (UV) pump beam is attenuated by an iris or a neutral density filter and focused by a 45-cm lens. The UV beam and the x-ray beam overlap in the sample gas cell at approximately 1°. The delay between the two beams hitting the sample gas cell is controlled by a high precision Aerospace mechanical stage. After the sample gas cell, the two beams diverge. The XUV/soft x-ray beam propagates further to be diffracted by the grating while the UV beam hits a black beam blocker.

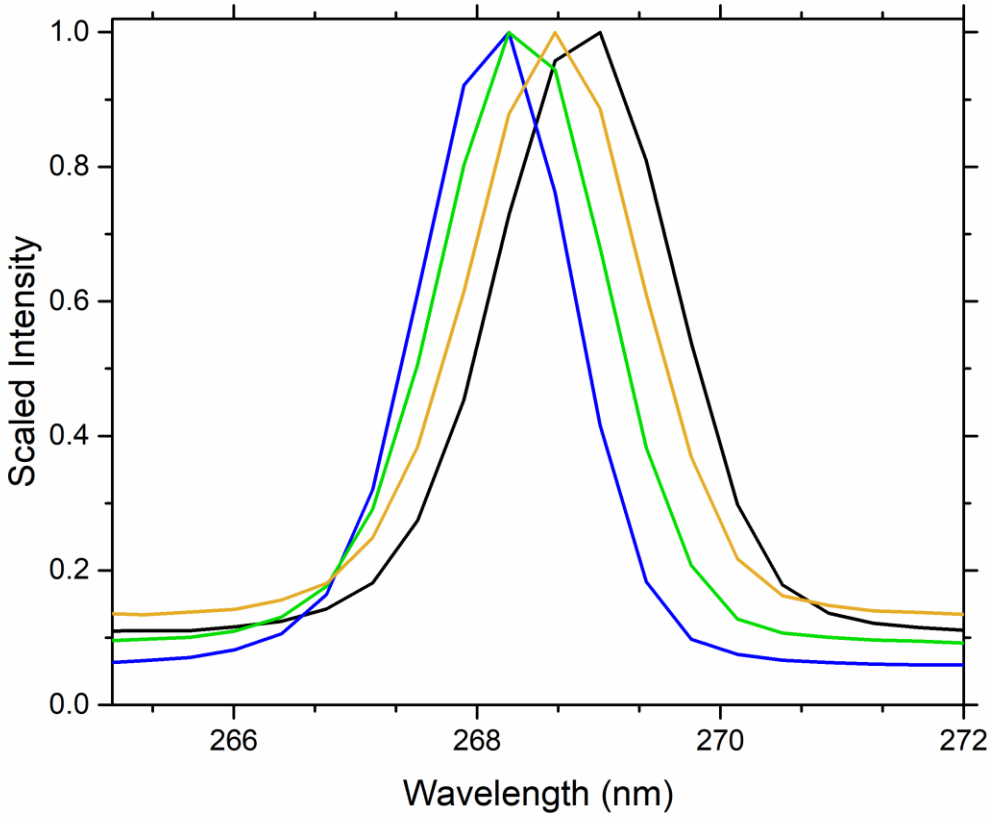

Figure 2.6 Characterization of the third harmonic generation by the Ocean Optics spectrometer. The central wavelength is tunable between 268.3 and 269 nm. The bandwidth is ~1.8 nm.

Two titanium filters need to be used in this apparatus. One 200 nm thick Ti filter is used to block residual 266 nm so that it does not interfere with the XUV/soft x-ray signal on the CCD camera. The other 100 nm thick Ti filter is used to prevent the gas from the sample reservoir from contaminating the toroidal mirror. The HHG flux with and without the two titanium filters are compared in Figure 2.7.

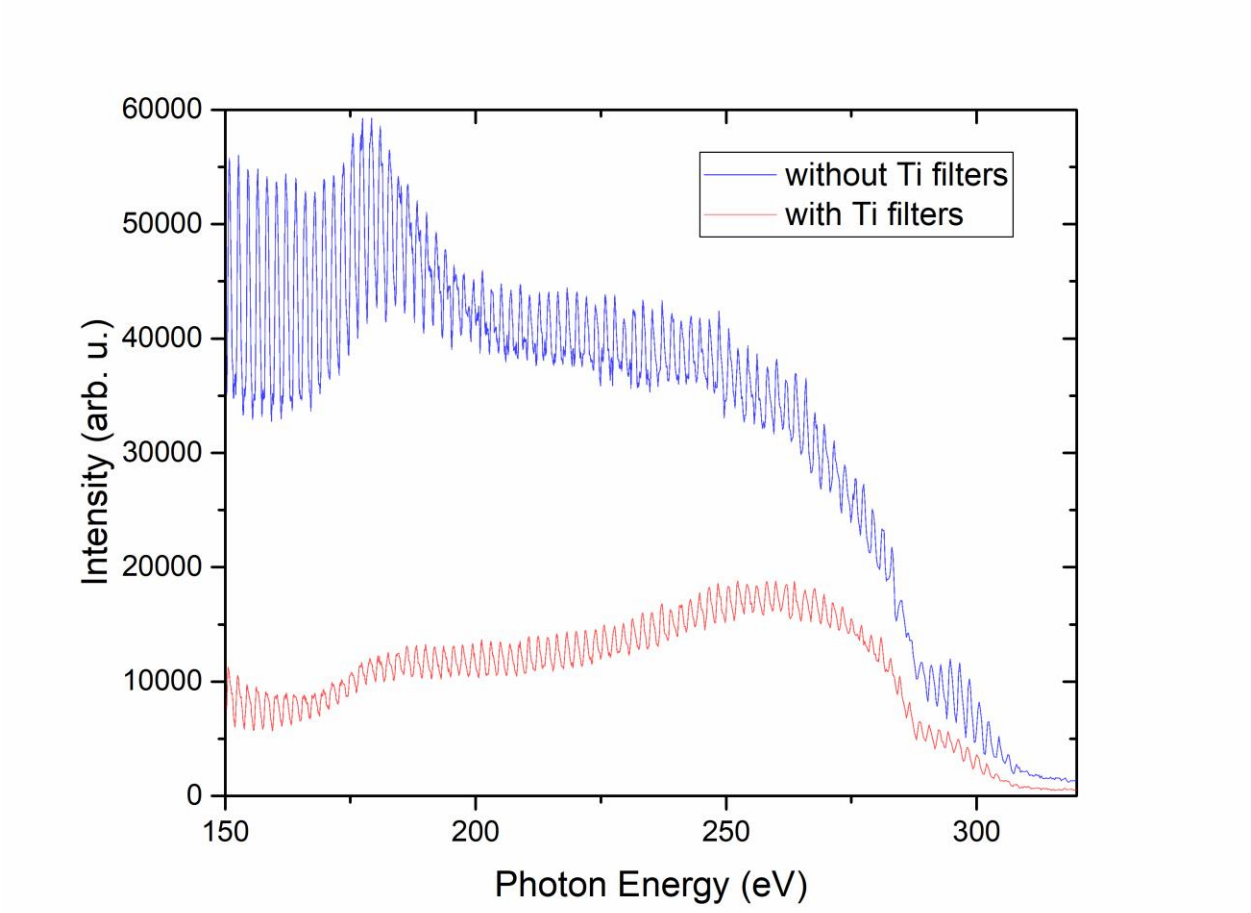

Figure 2.7 Comparing the high harmonic generation flux with and without putting in the two titanium filters.

2.4 Data Acquisition and Analysis Methods

There are two types of spectra to be collected in this dissertation: static absorption spectrum and transient absorption spectrum.

A static absorption spectrum is the absorption spectrum of the target gas itself without initiating any dynamics. To this end, only the x-ray probe is used to acquire this type of spectrum. A typical static absorption spectrum is recorded with one second of camera exposure time, using the spectrum without the target gas as a background. The resultant spectrum, typically averaged over 64 such sets (i.e. 64000 pulses in total with gas, 64000 without) for improved statistics, is then calculated according to the Beer-Lambert law where

$$\text{Absorbance}_{\text{target gas}} = -\log_{10} \frac{\text{flux}_{\text{x-ray}}(\text{with gas})}{\text{flux}_{\text{x-ray}}(\text{without gas})} \qquad \text{Equation 2.2}$$

A transient absorption spectrum is the absorption spectrum of the target gas with UV excitation at various delay times with respect to the soft x-ray beam. Therefore both the pump and the probe are used to acquire this type of spectrum and the delay time is controlled by a motorized stage that is accurate to within 1 fs. A typical transient absorption spectrum is recorded with one second of camera exposure time, using the absorption spectrum without the pump UV beam as a background. The change between the two yields a transient spectrum where

$$\Delta\text{Absorbance}_{\text{target gas, delay timepoint}} = -\log_{10} \frac{\text{flux}_{\text{x-ray}}(\text{with gas, with UV})}{\text{flux}_{\text{x-ray}}(\text{with gas, without UV})} \qquad \text{Equation 2.3}$$

Each delay time is usually repeated 32 times (i.e. 32000 pulses with UV, 32000 pulses without) and coadded for improved statistics. The acquisition time is about two hours for a total of 50 delay times.

2.4.1 Energy Calibration and Determination of Spectral Resolution

After the soft x-ray is dispersed by the diffraction grating onto the CCD camera, an energy-to-pixel relation needs to be established in order to convert pixel numbers into correct photon energies. A raw image of the high harmonic generation spectrum (with 1320 nm, 40 cm lens) is demonstrated in Figure 2.8. Each column symbolizes photons of the same energy whereas the horizontal axis needs to be calibrated to the correct energy values.

The dispersion of x-ray wavelength on a grating follows Equation 2.4 (derived from the grating dispersion equation[18]) where A_0 is an offset term, B is a scaling factor from pixel to distance and α is the actual angle at which the x-ray hits the grating. A_0, B and α are parameters to be fit using species with literature values.

$$Pixel\ number = A_0 - B\tan\left(\frac{\pi}{2} - \sin^{-1}\left(\sin\alpha - \frac{1.4878}{Energy}\right)\right) \qquad \text{Equation 2.4}$$

One such species is argon which has 2p→Rydberg state transitions in 240-260 eV. Using the transitions of $2p_{3/2}$→4s (at 244.4 eV), $2p_{3/2}$→3d (at 246.9 eV), $2p_{3/2}$→4d (at 247.7 eV) and $2p_{1/2}$→3d (249.1 eV)[19] a proper pixel-to-energy relation can be established, as shown in Figure 2.9 after each column of pixel has been integrated.

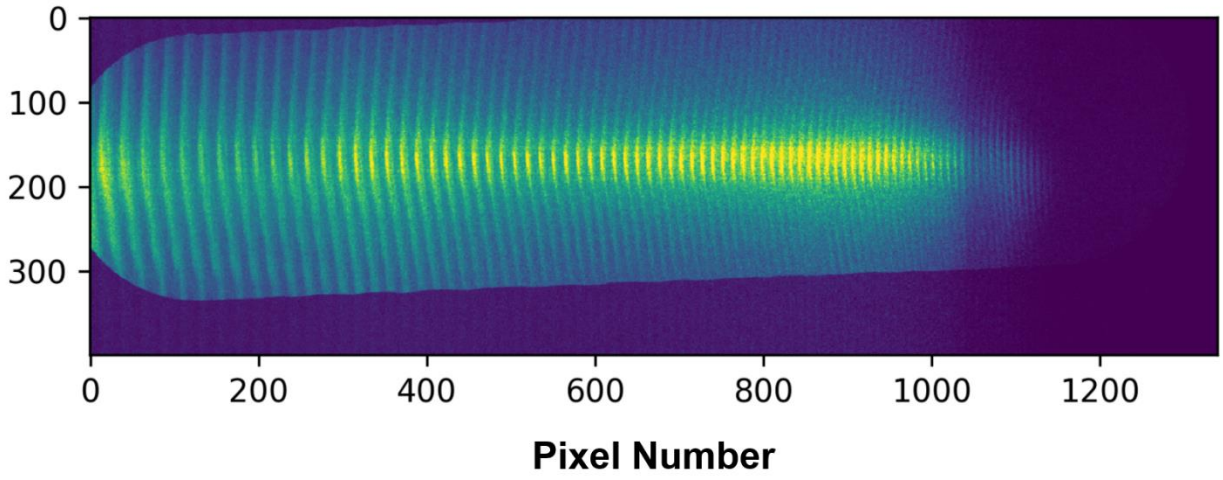

Figure 2.8 A raw image of the high harmonic generation spectrum (with 1320 nm, 40 cm lens). Both vertical and horizontal axes are pixel numbers and the color denotes intensity (blue indicates no counts and yellow indicates large number of counts). Counts on pixels with same horizontal pixel number correspond to the same photon energy while each horizontal pixel needs to be calibrated using known species, such as argon.

Transitions with known Lorentzian linewidths can also be used to determine the spectral resolution. Peak broadening in general results from the natural lifetime of the final state (as reflected in Lorentzian linewidth w_L) and the Gaussian broadening (w_G) due to the Doppler effect of the measured species,[20] dispersion capability of the diffraction grating and the pixel resolution of the CCD camera. The convolution of a broadened peak is given by Voigt function:[21]

$$I(E) = I_0 + A\frac{2\ln 2}{\pi^{3/2}}\frac{w_L}{{w_G}^2}\int_{-\infty}^{+\infty}\frac{e^{-t^2}}{(\sqrt{4\ln 2}\frac{E-E_c}{w_G}-t)^2+(\frac{w_L}{w_G}\sqrt{\ln 2})^2}dt \qquad \text{Equation 2.5}$$

where $I(E)$ is the intensity at a certain energy, E the energy, E_c the peak center, I_0 and A fitting parameters, w_L the Lorentzian linewidth from literatures and w_G the extrapolated spectral resolution.

In argon, the $2p_{3/2}\rightarrow 4s$ transition manifests itself as a single peak well separated from other transitions as shown in Figure 2.9 and has a well-documented lifetime.[19] Therefore it has been used to determine the spectral resolution as in Figure 2.10 where the resolution has been determined to be 360 ± 20 meV after fitting.

The spectral resolution is strongly dependent on the grating of choice. The larger number of lines/mm the grating has, the higher spectral resolution it has. Two XUV/soft x-ray gratings have been utilized to verify the effect of grating on spectral resolution: Hitachi 0010-0660 (1200 lines/mm, higher diffraction efficiency in XUV regime) and Hitachi 0010-0659 (2400 lines/mm, higher diffraction efficiency in soft x-ray regime). The spectral resolution can be improved to 240 ± 20 meV using Hitachi 0010-0659. But due to diffraction efficiency, the data acquisition time has to be extended to be five times longer.

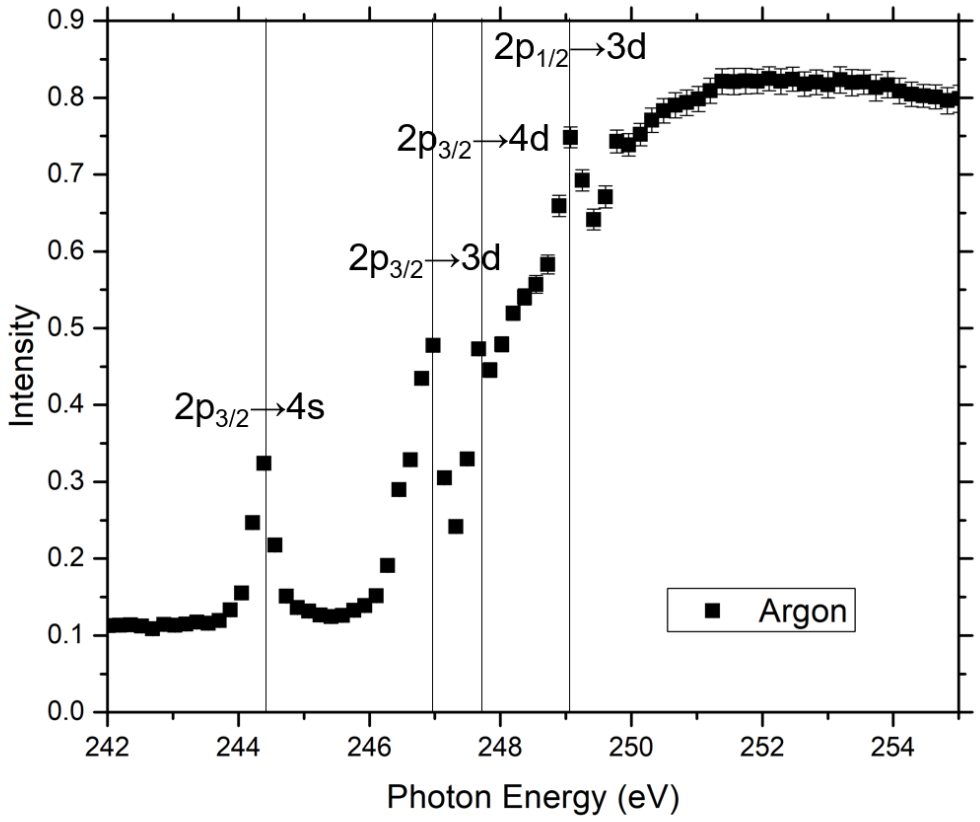

Figure 2.9 A calibrated argon spectrum after using reported literature values[19] to establish the pixel-to-energy relation.

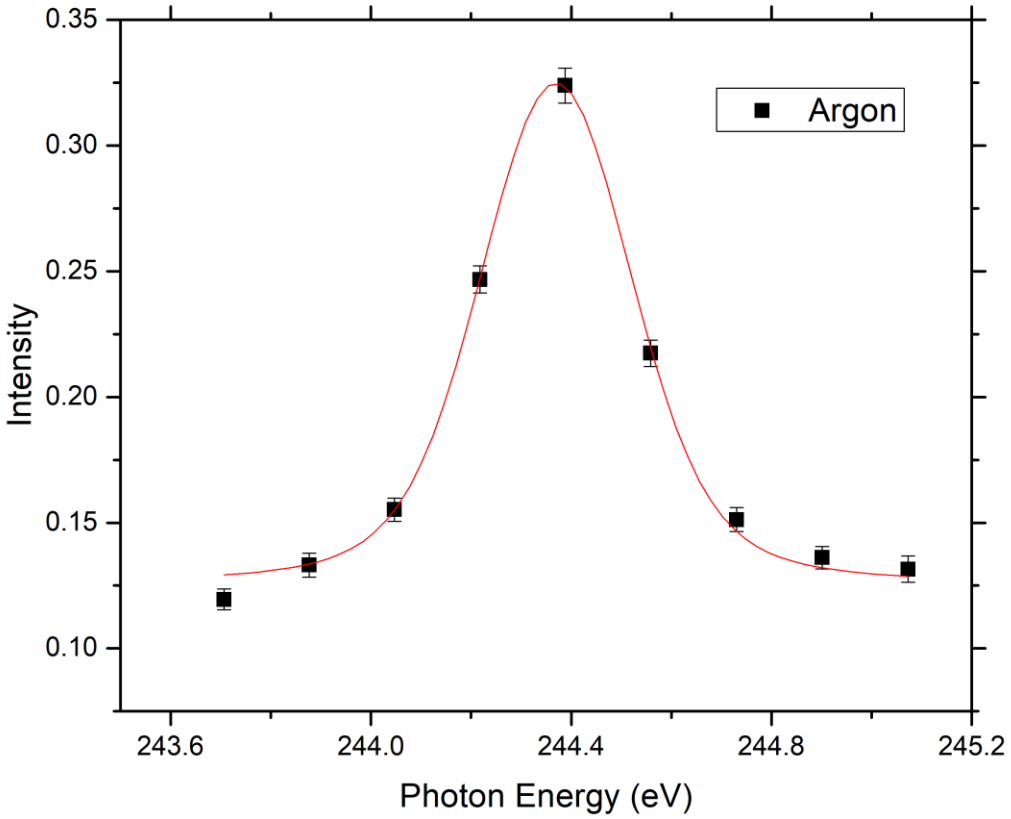

Figure 2.10 The $2p_{3/2} \rightarrow 4s$ transition observed in argon and fitted with the Voigt function using a Lorentzian linewidth of 121 meV.[19] The spectral resolution is thus determined to be 360 ± 20 meV after fitting using the grating model (Hitachi 001-0660).

2.4.2 Measurement of Temporal Resolution

To determine the temporal resolution of this pump-probe apparatus, the ponderomotive shift in the Rydberg states in argon has been monitored with the soft x-ray probe in the presence of a moderately intense UV field with the peak intensity of $0.5\text{-}2\times10^{12}$ W/cm^2. As the shift scales linearly with respect to the UV field, the intensity of the shift directly maps out the cross correlation between the UV pump and soft x-ray probe and thus carries information of the temporal resolution.[14]

A representative transient absorption spectrum of argon subjected to the UV field is shown in Figure 2.11. Four Rydberg transitions ($2p_{3/2} \rightarrow 4s$, $2p_{3/2} \rightarrow 3d$, $2p_{3/2} \rightarrow 4d$ and $2p_{1/2} \rightarrow 3d$) experience an apparent upward shift of ~0.2 eV. Table 2.2 summarizes the transitions with and without the UV field. By fitting the trace of each shift, the temporal resolution with this pump-probe setup can be analyzed as in Figure 2.12.

The temporal resolution is influenced by the UV pulse duration as well as the HHG pulse duration. By changing the compression inside the amplifier, the delay stage inside the TOPAS and the delay stage in the third harmonic generator, the temporal resolution can be optimized to 90±10 fs as shown in Figure 2.13.

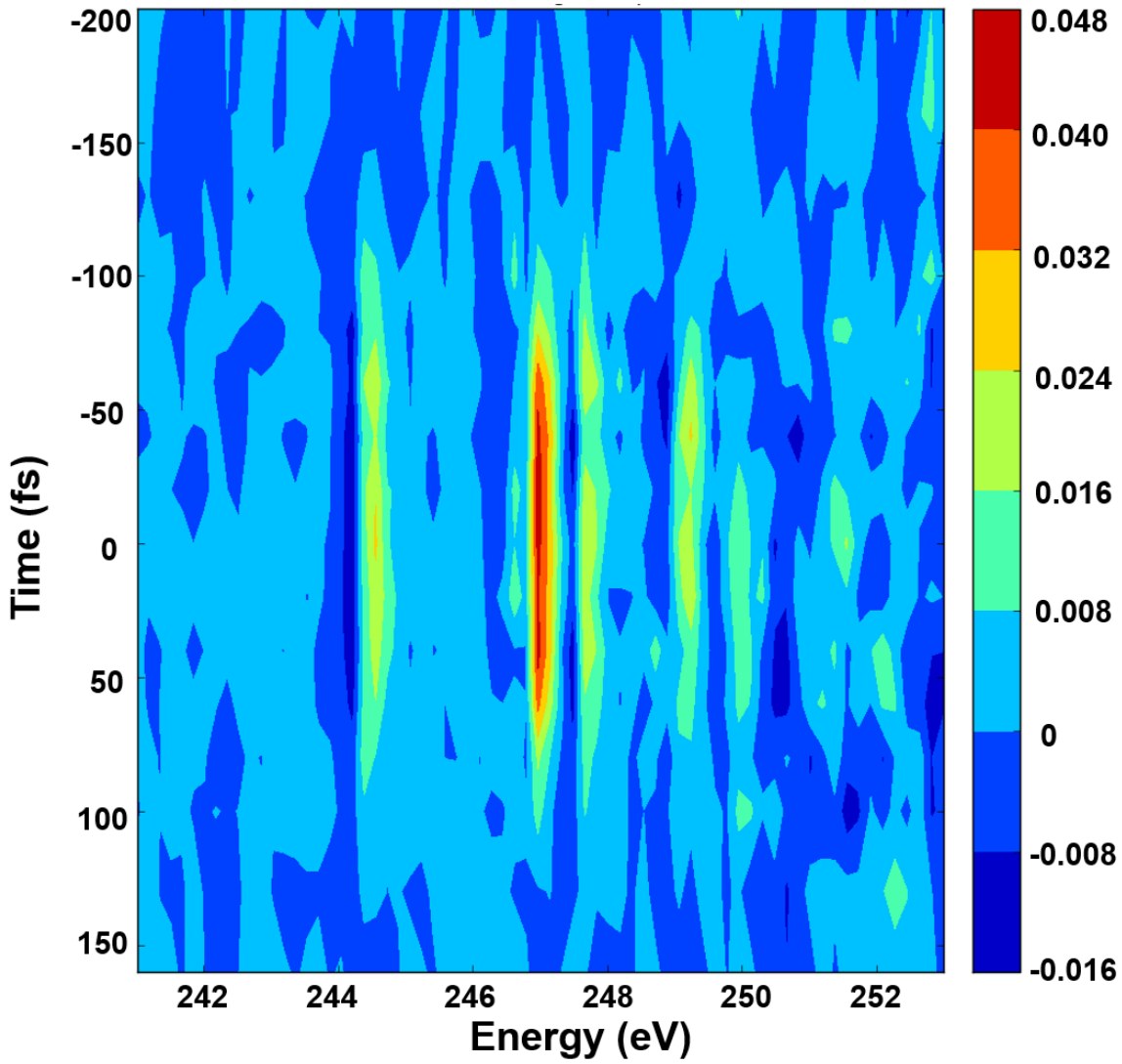

Figure 2.11 Temporal resolution measurement using the ponderomotive shift in Rydberg states in argon with a 30 µJ UV pulse energy focused with a 20 cm lens. Four transitions are observed with an apparent upward shift indicated by the orange-red lines around 244.6 eV, 247.2 eV, 247.8 eV and 249.3 eV.

Table 2.2 Rydberg transitions observed from argon 2p core levels with and without UV field.

Transition	Peak Position Without UV	Peak Shift Position With UV
$2p_{3/2} \rightarrow 4s$	244.4 eV	244.6 eV
$2p_{3/2} \rightarrow 3d$	246.9 eV	247.2 eV
$2p_{3/2} \rightarrow 4d$	247.7 eV	247.8 eV
$2p_{1/2} \rightarrow 3d$	249.1 eV	249.3 eV

In summary, a UV-pump HHG-probe apparatus has been implemented to perform core-level spectroscopic study of radicals at carbon K edge with defined spectral and temporal resolution. Both the UV intensity and HHG coverage have been significantly improved, which paves the way for strong field dynamics as well as experiments at nitrogen K edge (~400 eV).

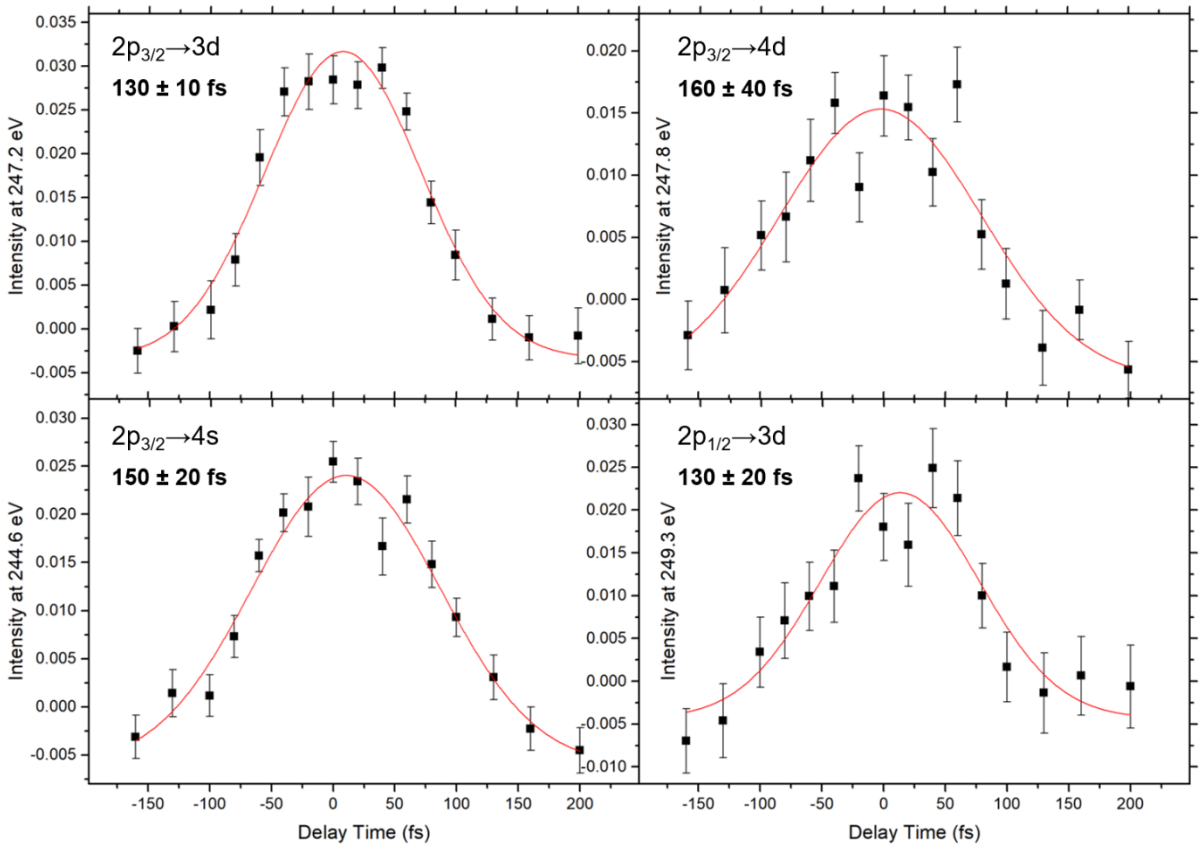

Figure 2.12 Fitting of the temporal traces (i.e. lineout at the respective energy in Figure 2.11) observed in the upward shift in the $2p_{3/2} \rightarrow 4s$, $2p_{3/2} \rightarrow 3d$, $2p_{3/2} \rightarrow 4d$ and $2p_{1/2} \rightarrow 3d$ transitions in argon.

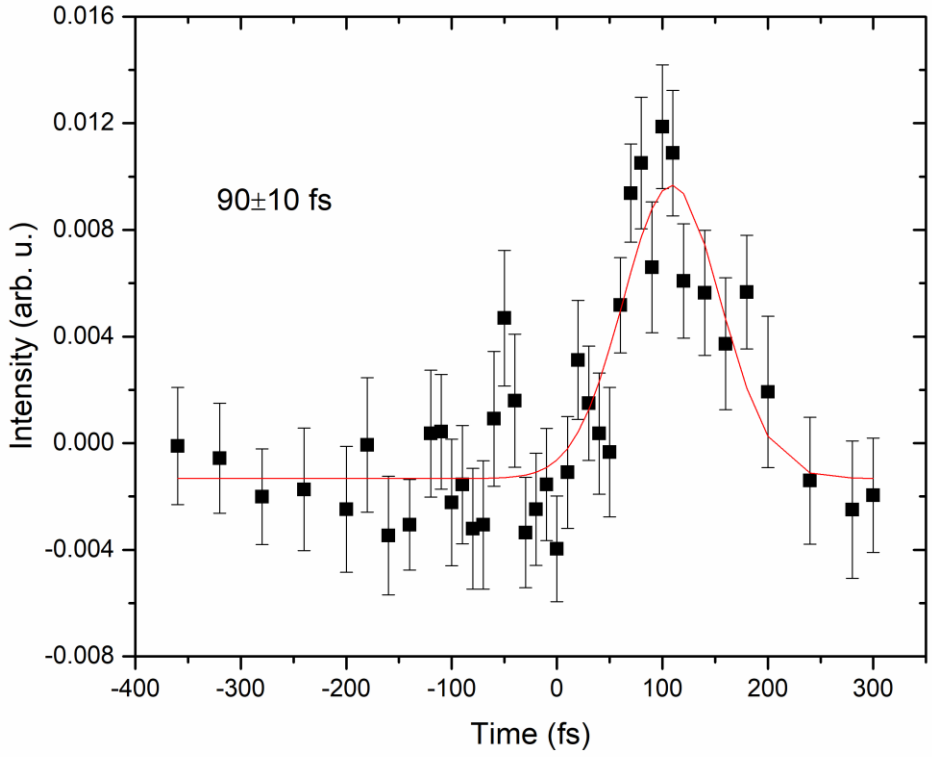

Figure 2.13 Optimized temporal resolution determined to be 90±10 fs using the shift in the $2p_{3/2} \rightarrow 4s$ transition in argon. The UV beam has a pulse energy of 30 µJ and is focused with a 45 cm lens.

2.5 Bibliography

1. Schoenlein, R. W.; Chattopadhyay, S.; Chong, H. H. W.; Glover, T. E.; Heimann, P. A.; Shank, C. V.; Zholents, A. A.; Zolotorev, M. S., Generation of femtosecond pulses of synchrotron radiation. *Science* **2000,** *287* (5461), 2237-2240.
2. Bressler, C.; Chergui, M., Molecular Structural Dynamics Probed by Ultrafast X-Ray Absorption Spectroscopy. *Annu Rev Phys Chem* **2010,** *61*, 263-282.
3. Chen, L. X.; Zhang, X.; Shelby, M. L., Recent advances on ultrafast X-ray spectroscopy in the chemical sciences. *Chem Sci* **2014,** *5* (11), 4136-4152.
4. Popmintchev, T.; Chen, M. C.; Bahabad, A.; Gerrity, M.; Sidorenko, P.; Cohen, O.; Christov, I. P.; Murnane, M. M.; Kapteyn, H. C., Phase matching of high harmonic generation in the soft and hard X-ray regions of the spectrum. *P Natl Acad Sci USA* **2009,** *106* (26), 10516-10521.
5. Xiong, H.; Xu, H.; Fu, Y. X.; Yao, J. P.; Zeng, B.; Chu, W.; Cheng, Y.; Xu, Z. Z.; Takahashi, E. J.; Midorikawa, K.; Liu, X.; Chen, J., Generation of a coherent x ray in the water

window region at 1 kHz repetition rate using a mid-infrared pump source. *Opt Lett* **2009,** *34* (11), 1747-1749.
6. Popmintchev, T.; Chen, M. C.; Popmintchev, D.; Arpin, P.; Brown, S.; Alisauskas, S.; Andriukaitis, G.; Balciunas, T.; Mucke, O. D.; Pugzlys, A.; Baltuska, A.; Shim, B.; Schrauth, S. E.; Gaeta, A.; Hernandez-Garcia, C.; Plaja, L.; Becker, A.; Jaron-Becker, A.; Murnane, M. M.; Kapteyn, H. C., Bright Coherent Ultrahigh Harmonics in the keV X-ray Regime from Mid-Infrared Femtosecond Lasers. *Science* **2012,** *336* (6086), 1287-1291.
7. Corkum, P. B., Plasma Perspective on Strong-Field Multiphoton Ionization. *Phys Rev Lett* **1993,** *71* (13), 1994-1997.
8. Tate, J.; Auguste, T.; Muller, H. G.; Salieres, P.; Agostini, P.; DiMauro, L. F., Scaling of wave-packet dynamics in an intense midinfrared field. *Phys Rev Lett* **2007,** *98* (1).
9. Shiner, A. D.; Trallero-Herrero, C.; Kajumba, N.; Bandulet, H. C.; Comtois, D.; Legare, F.; Giguere, M.; Kieffer, J. C.; Corkum, P. B.; Villeneuve, D. M., Wavelength Scaling of High Harmonic Generation Efficiency. *Phys Rev Lett* **2009,** *103* (7).
10. Attar, A. R.; Piticco, L.; Leone, S. R., Core-to-valence spectroscopic detection of the CH2Br radical and element-specific femtosecond photodissociation dynamics of CH2IBr. *J Chem Phys* **2014,** *141* (16).
11. Jiang, C. M.; Baker, L. R.; Lucas, J. M.; Vura-Weis, J.; Alivisatos, A. P.; Leone, S. R., Characterization of Photo-Induced Charge Transfer and Hot Carrier Relaxation Pathways in Spinel Cobalt Oxide (CO_3O_4). *J Phys Chem C* **2014,** *118* (39), 22774-22784.
12. Lytle, A. L. Phase Matching and Coherence of High-Order Harmonic Generation in Hollow Waveguides. Doctoral thesis, University of Colorado, Boulder, Colorado, 2008.
13. Strickland, D.; Mourou, G., Compression of Amplified Chirped Optical Pulses. *Opt Commun* **1985,** *56* (3), 219-221.
14. Attar, A. Photochemical Reaction Dynamics Studied by Femtosecond Soft X-ray Transient Absorption Spectroscopy. Doctoral Thesis, University of California, Berkeley, California, University of California, Berkeley, 2016.
15. Sutherland, J. R.; Christensen, E. L.; Powers, N. D.; Rhynard, S. E.; Painter, J. C.; Peatross, J., High harmonic generation in a semi-infinite gas cell. *Opt Express* **2004,** *12* (19), 4430-4436.
16. Yu, X. M.; Bian, Q. M.; Chang, Z. H.; Corkum, P. B.; Lei, S. T., Femtosecond laser nanomachining initiated by ultraviolet multiphoton ionization. *Opt Express* **2013,** *21* (20), 24185-24190.
17. Wilbois, T.; Helm, H., Strong-field ionization of H-2 from ultraviolet to near-infrared wavelengths: Photoelectron energy and angular identifications. *Phys Rev A* **2011,** *84* (5).
18. Palmer, C., *Diffraction Grating Handbook*. 5th ed.; Newport Corporation: Rochester, NY, 2000.
19. King, G. C.; Tronc, M.; Read, F. H.; Bradford, R. C., Investigation of Structure near $L_{2,3}$ Edges of Argon, M4,5 Edges of Krypton and N4,5 Edges of Xenon, Using Electron-Impact with High-Resolution. *J Phys B-at Mol Opt* **1977,** *10* (12), 2479-2495.
20. Ward, J.; Cooper, J.; Smith, E. W., Correlation Effects in Theory of Combined Doppler and Pressure Broadening .1. Classical Theory. *J Quant Spectrosc Ra* **1974,** *14* (7), 555-590.
21. Di Rocco, H. O.; Iriarte, D. I.; Pomarico, J., General expression for the Voigt function that is of special interest for applied spectroscopy. *Appl Spectrosc* **2001,** *55* (7), 822-826.

Chapter 3. Core-Level Spectroscopic Studies of Halogenated Radicals – CH_2Cl and CH_2Br

3.1 The Electron-Withdrawing Effect in CH_2Cl

The content and figures in this section are reprinted or adapted with permission from Zheyue Yang , Kirsten Schnorr, Aditi Bhattacherjee, Pierre-Louis Lefebvre, Michael Epshtein, Tian Xue, John F. Stanton, and Stephen R. Leone, "Electron-Withdrawing Effects in the Photodissociation of CH_2ICl To Form CH_2Cl Radical, Simultaneously Viewed Through the Carbon K and Chlorine $L_{2,3}$ X-ray Edges," Journal of the American Chemical Society, 2018, 140(41), 13360, Copyright 2018 ACS Publications

3.1.1 Introduction

Radicals, characterized by partially filled orbitals, have triggered much interest due to their transient nature and ubiquitous role in chemical reactivity. Halogenated radicals, in particular, are common intermediates and byproducts in combustion and atmospheric processes and constitute an important subgroup that has been given significant attention over the last decades.[1-2] As one of the most representative radicals of this kind, CH_2Cl radical has been proposed, with various mechanisms, to be an inhibitor in the combustion of chlorinated fuels[3], an origin of soot formation[4], as well as a key to stratospheric processes such as ozone depletion[5], in addition to marine decomposition where boundary aqueous layers react with these radicals to a non-negligible extent.[6] It is fundamental to explore the electronic structures and energetics of these transient species, which are usually difficult to capture in reactions.

Ultrafast laser techniques, especially transient absorption spectroscopy, provide a robust way to study short-lived reaction intermediates. Selective bond-breaking, made possible by photodissociation at a specific wavelength, produces desirable transient species in a consistent fashion. In particular, the C-I bond, known to dissociate at approximately 270 nm, can be utilized to form specific radicals from iodine-containing organic molecules.[7] Furthermore, transient absorption spectroscopy, as opposed to electron or ion spectroscopy, is capable of detecting not only charged species, but also neutral ones, thus allowing studies of the altered electronic structure resulting from neutral dissociation or ionization. Recent progress toward core-level spectroscopy centered on the carbon K edge demonstrates the power of using x-ray spectroscopic techniques to study the dynamics and the electronic structures of transient species.[8-10]

The UV spectrum of CH_2ICl, like other C-I containing molecules, has a characteristic A band absorption corresponding to the electronic transition from the localized nonbonding iodine atomic orbitals n(I) to the σ*(C-I) molecular orbital.[7, 11-13] The potential energy surface of CH_2ICl resembles that of CH_3I where the 3A' state (equivalent to the $^3Q_0$ state in CH_3I but with a lower symmetry) is excited at ~270 nm and leads to a major channel dissociating into CH_2Cl and $I^*(^2P_{1/2})$ and a minor one into CH_2Cl and $I(^2P_{3/2})$ by passage through a conical intersection, both of which take place within 150 fs.[12] In the pump-probe experiment here, a 266 nm-pump pulse is used to first initiate the C-I bond cleavage of CH_2ICl and broad band soft x-ray pulses then probe the electronic structure of the product CH_2Cl by transient absorption spectroscopy. The transient

radical species is thus characterized from the perspectives of both the carbon and the chlorine atoms by spectroscopic investigations on their core-shell transitions (1s and 2p, respectively).

As the iodine atom departs the parent CH_2ICl molecule and CH_2Cl is formed, the primary effect on the carbon atom as well as a secondary effect on the chlorine atom are captured simultaneously through shifts in the core-to-valence transitions. Iodine, as a strongly electron withdrawing element, significantly impacts the oxidation state of the carbon atom by bonding, which is reflected in a shift of the carbon core level. The molecular geometry will also accommodate the departure of iodine, allowing more space for carbon-chlorine bonding, strengthening the C-Cl bond and consequently changing the valence orbital energy levels. Chlorine, while not directly affected by the electronegativity of iodine, experiences this change through the valence bonding and antibonding orbitals. Since both the carbon and chlorine core-level transitions couple to the same σ^*(C-Cl) antibonding orbital, these energy shifts upon going from the closed shell molecule to the radical are obtained directly in the experiment and corroborated by electronic structure calculations.

3.1.2 Experimental Method

The apparatus to generate the pump pulse of 266 nm and broadband x-ray probe pulse has been described in the previous chapters.[8-9] In brief, the output of a 12 mJ per pulse, 800 nm-centered, 1 kHz repetition rate, 35-fs Ti:Sapphire femtosecond laser is split into two branches in a 9:1 ratio. The 10% branch is used to produce third harmonic generation with two non-linear crystals to generate ultraviolet pulses centered at around 266 nm. The other 90% is used as a pump for a tunable traveling-wave optical parametric amplifier of superfluorescence (TOPAS), which is tuned to output infrared light at 1320 nm with a pulse energy of 2.5-2.8 mJ. These near infrared pulses are subsequently focused by a 40-cm lens into a semi-infinite gas cell filled with 750-800 Torr of helium to emit soft x-ray light ranging from 150 eV to 300 eV through the high harmonic generation (HHG) process. The residual infrared light is blocked by a 100 nm thick aluminum filter whereas the soft x-ray radiation is transmitted and further focused by a toroidal mirror. The 266 nm ultraviolet (UV) pump beam is attenuated by a neutral density filter and focused by a 45-cm lens where the pulse energy can be adjusted between 10-30 μJ and the pump intensity between $2\text{-}5\times10^{11}$ W/cm^2. The soft x-ray and the UV beam overlap at an angle of approximately one degree within a flowing gas cell containing the CH_2ICl sample purchased from Sigma-Aldrich and used at ~60 °C (vapor pressure ~150 Torr, entire gas line heated) after freeze-pump-thaw degassing. The soft x-ray beam is transmitted by the gas cell, diffracted by an x-ray grating onto a charged-couple device (CCD) camera chip with 1340×400 pixels and the UV beam is blocked by a 100 nm thick titanium filter after the gas cell to prevent pump scattering.

A static absorption spectrum of a target gas is recorded with one second of camera exposure time and with the soft x-ray beam only, using the spectrum without the target gas as a background. The resultant spectrum of the parent molecule CH_2ICl, averaged over 64 such sets (64000 pulses in total with gas, 64000 without) for improved statistics, is then calculated according to the Beer-Lambert law where:

$$\text{Absorbance}_{\text{target gas}} = -\log_{10} \frac{\text{flux}_{\text{x-ray}}(\text{with gas})}{\text{flux}_{\text{x-ray}}(\text{without gas})}$$

A transient absorption spectrum is recorded with one second of camera exposure time with both the pump UV and the probe soft x-ray beam, the delay time between which is controlled by a motorized stage to include 50 time points in between -300 fs (x-ray preceding UV) and 1000 fs (UV preceding x-ray), using the absorption spectrum without the pump UV beam as a background. The change between the two yields a transient spectrum where

$$\Delta\text{Absorbance}_{\text{target gas, delay timepoint}} = -\log_{10} \frac{\text{flux}_{\text{x-ray}}(\text{with gas, with UV})}{\text{flux}_{\text{x-ray}}(\text{with gas, without UV})}$$

and averaged over at least 32 such sets (32000 pulses with UV, 32000 pulses without UV at each time delay point) for statistics, which takes typically two hours for 50 points overall.

The energy scale for all spectra are calibrated using known core-to-valence transitions in argon[14], carbon disulfide[15-16] and methyl iodide[17]. The spectral resolution is determined to be 360±20 meV by the Gaussian broadening of the $2p_{3/2} \rightarrow 4s$ transition in argon to match the observed spectra, assuming the core-hole lifetime broadening is 120 meV.[14] The temporal resolution is estimated to be 90±10 fs based on the ponderomotive shift of the $2p_{3/2} \rightarrow 4s$ transition in argon.[9]

The core-level excited states of CH_2ICl and CH_2Cl are calculated with the techniques of coupled-cluster theory. For CH_2ICl, which has a closed-shell ground state, excitation energies are obtained with the EOM-CCSD* method,[18-19] in conjunction with the SFX2C-1e treatment of relativistic effects[20-22] (which are important in the treatment of core-level processes, even in the carbon atom) with relativistic atomic natural orbital basis sets (ANORCC[23]) of triple-zeta quality, truncated to 5s4p2d1f on Cl, 7s6p4d2f1g on I, 4s3p2d1f on C and 3s2p1d on H.[24] Oscillator strengths are also obtained with the same basis sets and SFX2C-1e, but only at the CCSD level. For the CH_2Cl radical, the x-ray excitation energy is computed by taking the difference between the ground state energy and the excited state energy, the latter being calculated using EOMIP-CCSDT theory[25] using the CH_2Cl anion as the reference state. The SFX2C-1e treatment of relativistic effects and the basis sets listed above were again used. All calculations are performed with the CFOUR program suite[24] in the frozen-core approximation, in which all electrons lower in energy than the carbon 1s and chlorine 2s orbitals are omitted from the correlation part of the calculation. In addition, all calculations are performed at geometries optimized at the MP2 level with the SFX2C-1e treatment and the basis sets listed above.

3.1.3 Results and Discussion

3.1.3.1 Static Soft X-Ray Absorption Spectra of CH_2ICl

Figures 3.1(a) and (b) show representative static absorption spectra of CH_2ICl at the carbon K (1s) edge and the chlorine $L_{2,3}$ (spin-orbit split $2p_{1/2}$ and $2p_{3/2}$) edges, respectively, acquired as described earlier. To our knowledge, no Cl L edge or C K edge absorption spectra of CH_2ICl have been reported and assignments are based on peaks observed in similar halogenated molecules (CH_3Cl and CH_3I) and complementary computations shown in Tables 3.1 and 3.2.

In the carbon K edge region, peaks A and B are separated by 1.6 eV, which is the same difference between the reported values for the C(1s) $\rightarrow$ σ^*(C-I) transition in CH_3I and the C(1s) $\rightarrow$ σ^*(C-Cl) transition in CH_3Cl from electron scattering studies.[17] However, peaks A and B are

~1 eV blue shifted from the C(1s) → σ*(C-I) in CH_3I and the C(1s) → σ*(C-Cl) in CH_3Cl, respectively. This leads to the assignment of peak A to the C(1s) → σ*(C-I) and peak B to the C(1s) → σ*(C-Cl) in CH_2ICl. The 1 eV shifts from the monohalomethanes are understood as the additional electron withdrawing effect from the central carbon atom because there are two halogen atoms instead of one, making the carbon atom more electron deficient and leading to a stronger Coulomb attraction between the nucleus and the carbon 1s electrons. The energy thus required to excite an electron from the carbon core level to valence antibonding orbitals is increased by 1 eV. Additionally, based on the equation of motion coupled-cluster theory (EOM-CCSD) from which predictions of peak positions and oscillator strengths convoluted with spectral resolution as well as orbital pictures are shown in Table 3.2, peak A displays a C-I antibonding nature whereas peak B signifies C-Cl antibonding and peaks C and D C-H antibonding. Peak separations match extremely well with the experimental data although the absolute energies from the computations are in general 0.3-0.4 eV higher. Similar relative shifts with respect to the respective monohalogenated methanes suggest that the antibonding character is preserved in CH_2ICl.

In comparison, peaks E and F observed at the chlorine L_3 ($2p_{3/2}$) and L_2 ($2p_{1/2}$) edges, respectively, are very close to the values of the excitation energies of Cl 2p → σ*(C-Cl) transitions observed in CH_3Cl, CH_2Cl_2, $CHCl_3$ and CCl_4,[26-28] as listed in Table 3.1. This highlights the well-known sensitivity of the x-ray absorption spectrum to the localized oxidation state of the reporter atom, as the oxidation state of carbon is significantly more greatly changed upon additional halogenation than the neighboring halogen atoms. The 1.7 eV difference between E and F is consistent with the Cl 2p inner shell spin-orbit splitting observed in these species. The population ratio of the two spin-orbit components is not following the degeneracy factor (2:1) possibly due to multiplet effects which in particular occurs at soft x-ray edges where these core orbitals can overlap with valence orbitals, as reported by de Groot.[29] Peak G and I constitute another spin-orbit pair, which may correspond to transitions to higher lying Rydberg states (such as 4s), according to previous literature.[26-28] A weak and broad feature, observed as peak H, remains unassigned at present.

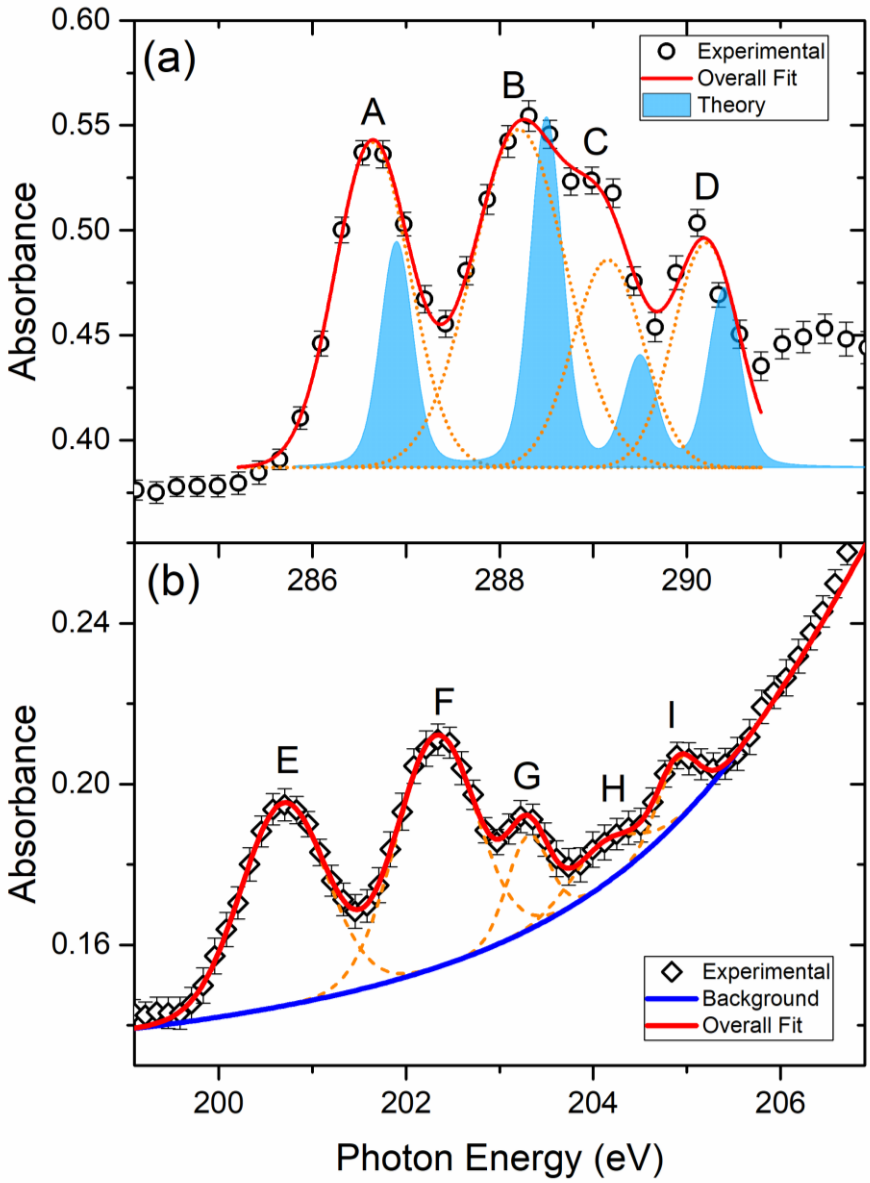

Figure 3.1 Static absorption spectra of CH_2ICl at the (a) carbon K edge and (b) chlorine $L_{2,3}$ edges where the orange dash lines are Gaussian fits to the peaks, the red solid lines summation of all the fitted peaks, the shaded blue area is computational results convoluted with instrumental spectral resolution and the core-hole lifetime from Alagia *et al*[30] and scaled with respect to the experimental absorbance and the blue solid line the extrapolated background (due to core photoionization). The actual core-hole lifetime may be different. Additionally, the experimental peaks can be broadened due to vibronic coupling. The spectral resolution reported here is not able to resolve these fine details and the theoretical ones only compute the transitions from the electronic ground state to the ground core-hole state. Peaks A-F are assigned as in Table 3.1. An overview across the whole spectral range is shown in Figure 3.2.

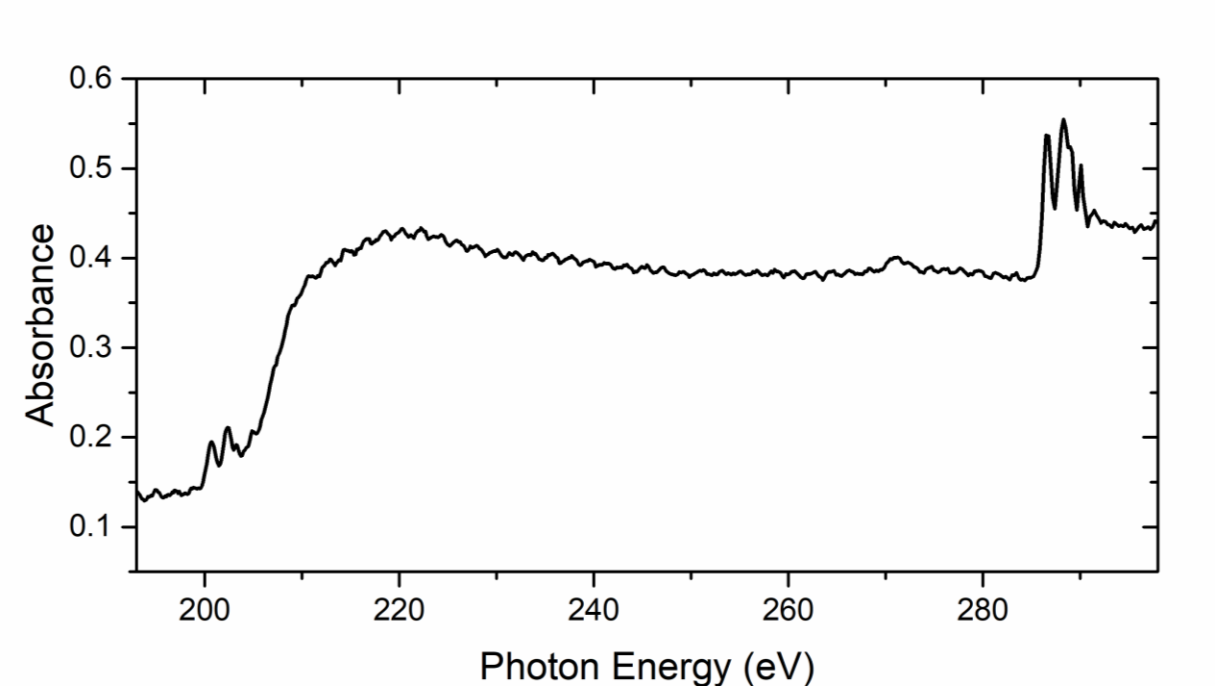

Figure 3.2 An overview of the CH_2ICl absorption spectrum across the whole spectral range to demonstrate the overall absorption structure. Figure 3.1(a) and (b) zoom into the 284-292 eV and the 199-207 eV respectively.

Table 3.1 Assignments of spectral features observed at C K edge and Cl $L_{2,3}$ edges of CH_2ICl.[a]

Peak	Exptl. Energy (eV)	Exptl. Ref. Energy (eV) (Ref. Molecule)	Assignment
A	286.6 ± 0.1	285.6 (CH_3I)[17]	C(1s) → σ*(C-I)
B	288.2 ± 0.1	287.3 (CH_3Cl)[17]	C(1s) → σ*(C-Cl)
C	289.1 ± 0.1	-	C(1s) → σ*(C-H)
D	290.0 ± 0.1	-	C(1s) → σ*(C-H)
E	200.6 ± 0.1	200.8 (CH_3Cl), 200.8 (CH_2Cl_2), 200.6 ($CHCl_3$), 200.5 (CCl_4)[26-28]	Cl($2p_{3/2}$) → σ*(C-Cl)
F	202.3 ± 0.1	202.4 (CH_3Cl), 202.9 (CH_2Cl_2), 202.4 ($CHCl_3$), 202.4(CCl_4)[26-27]	Cl($2p_{1/2}$) → σ*(C-Cl)

a The numbers are averaged Gaussian fitting results of three such representative spectra reproduced on different days. The errors are one standard deviation from these three spectra convoluted with Gaussian fitting errors.

Table 3.2 Absorption of CH_2ICl at the carbon K edge based on EOM-CCSD* calculations.

Peak	A	B	C	D
Energy	286.9 eV	288.5 eV	289.5 eV	290.4 eV
Oscillator Strength	0.029	0.045	0.014	0.023
Orbital	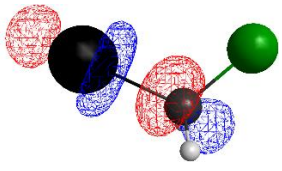	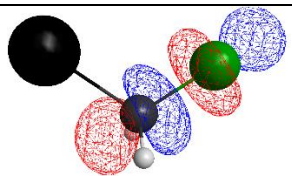	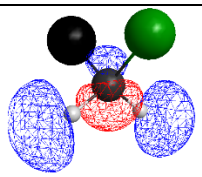	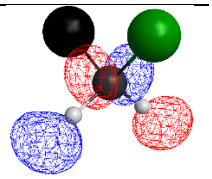

To summarize, by promoting an electron from one of the core orbitals to one vacant valence orbital, core-level spectroscopy not only offers information about the energy difference between core shell and valence shell, but also the relative difference among the valence orbitals.

3.1.3.2 Transient Absorption Spectra of CH_2ICl: Formation of CH_2Cl Radical as a Photodissociation Product

Representative transient absorption spectra of CH_2ICl obtained as mentioned earlier and integrated at long delay time points between 400 fs and 1000 fs are shown in Figure 3.3. CH_2ICl is known to have a C-I bond dissociation timescale of 100-150 fs,[12-13] as verified by the temporal dependence of the features shown in Figure 3.4. Hence at 400 fs, long after the photodissociation is complete, the spectra reflect absorption of the photodissociation products and depletion of the parent molecule. Positive-going features represent new species that occur when UV light excites and dissociates CH_2ICl and negative features indicate changes in the static spectrum when the CH_2ICl molecules are depleted by UV excitation.

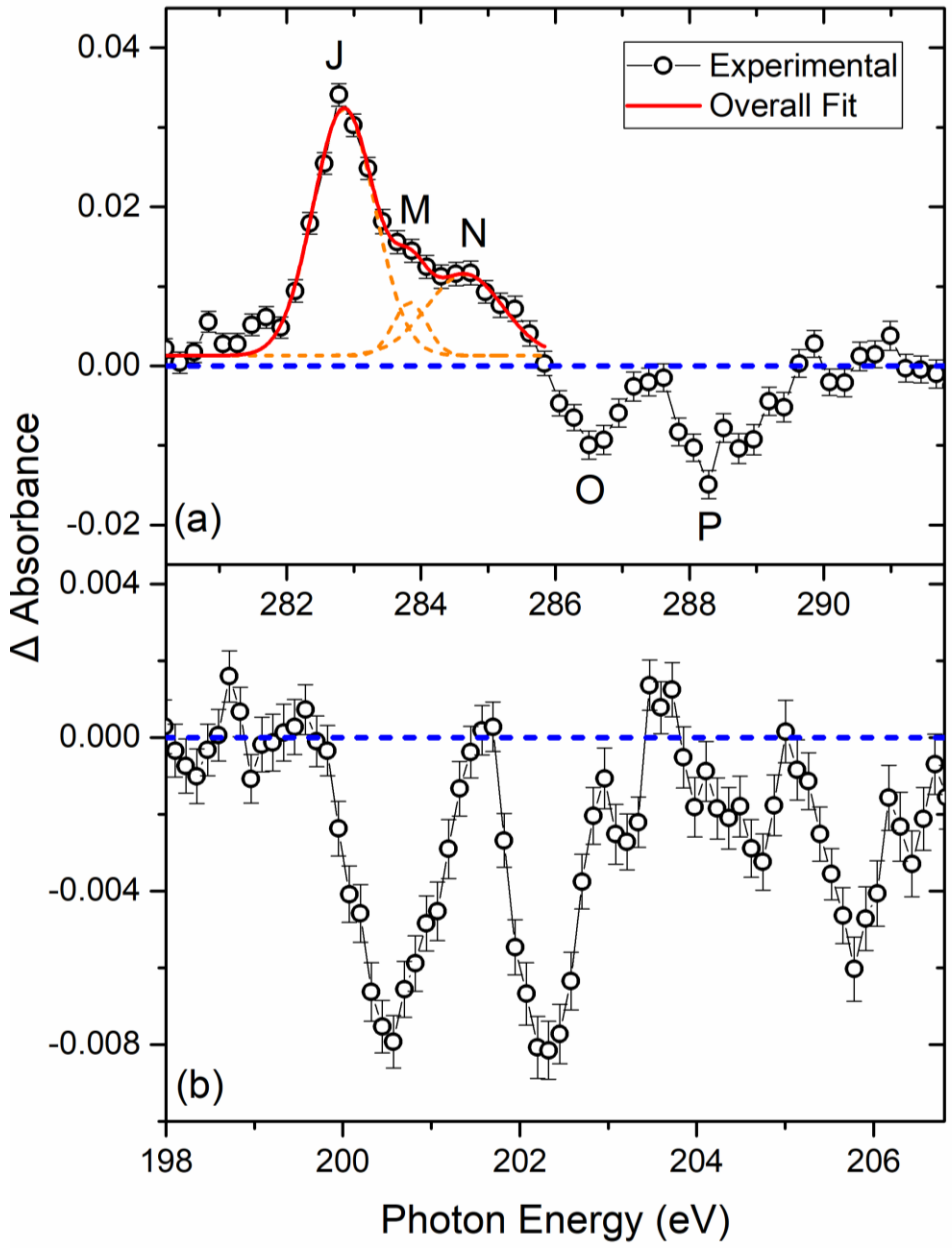

Figure 3.3 Transient absorption spectra of CH_2ICl at the (a) carbon K edge where the orange lines are deconvoluted Gaussian peaks and the red line summation of all the fitted peaks and (b) chlorine $L_{2,3}$ edges. The blue lines are reference zero lines.

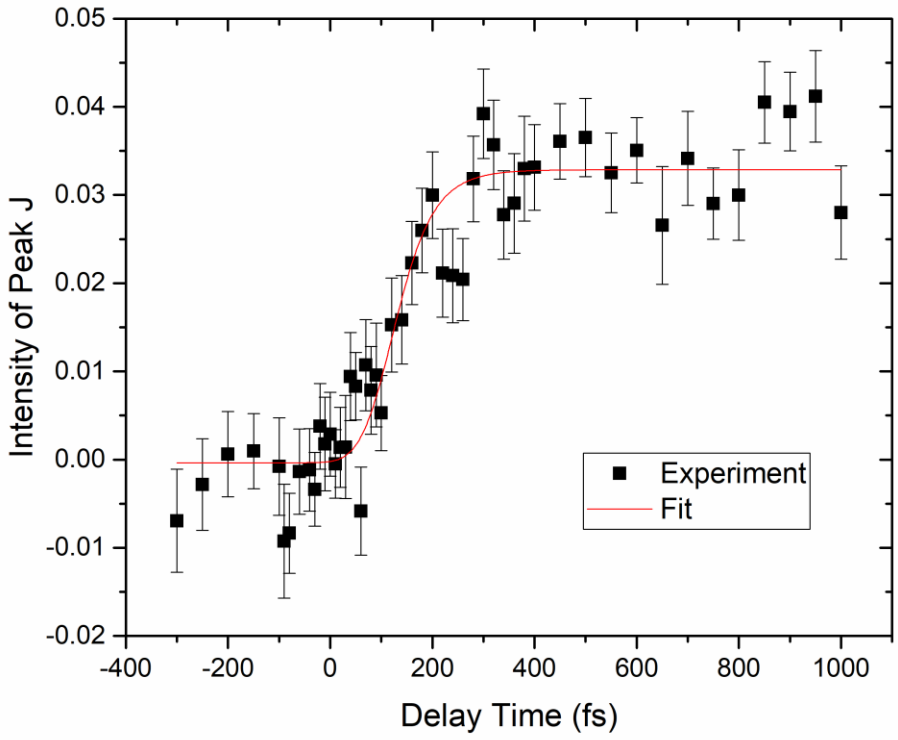

Figure 3.4 Temporal dependence of peak J, which is fit with an exponential rise convoluted with a 90-fs instrumental response. The photodissociation is complete after ~150 fs. The spectra at intermediate delay times (50-150 fs) greatly resemble the spectra at the asymptotic limit but with less intensity. Results from 400 fs to 1000 fs are averaged to get electronic structures of the product. The spectrum is obtained 32 times *in situ* with data taken at all the delay time points and co-added. The whole acquisition time is about 2 hours in total.

A new strong positive feature in the carbon K edge region at 282.8±0.1 eV, peak J, is observed and accompanied by two broad shoulder features M and N at ~284 eV. CH_2ICl photodissociation at 266 nm is dominated by direct dissociation when an iodine 5p electron is promoted to the σ*(C-I) orbital, leading to electronically repulsive states and photodissociation products of CH_2Cl and I or I*.[12] Along the photodissociation coordinate, the σ*(C-I) orbital is broken into nonbonding I 5p and C 2p orbitals. Peak J is thus attributed to the transition of C(1s) → C(2p) in the CH_2Cl radical, as the C 2p orbital of the radical is singly occupied. According to the calculations outlined earlier, this core to the singly occupied molecular orbital (SOMO) transition occurs at 282.8 eV strongly resembles a carbon 2p orbital, perfectly matching the experimental observations. It is worth noting that this transition is 1.5 eV higher in energy than the C(1s) → C(2p) transition observed in CH_3[30] and this difference of 1.5 eV can be rationalized by the electron withdrawing effect of chlorine on the carbon atom. The result is also consistent with the 1.5 eV difference found in the carbon 1s ionization potentials between CH_4 (290.8 eV) and CH_3Cl (292.3 eV) reported in the x-ray photoelectron spectroscopy literature.[26-27]

Features M and N are determined to be related to non-linear (multiphoton) absorption processes. The dependence of both peaks on the UV power, in comparison with peak J, are demonstrated in Figure 3.5, where the log of peak intensity is plotted versus the UV excitation power. Peak J results in a slope of 0.9±0.1 whereas M and N have to a slope of 2.8±0.2 and 2.9±0.4 respectively, a sign of multiphoton processes.[31] One possible source of M and N is ionization of CH_2ICl, which requires three photons.[32] Upon ionization, one electron will be ejected from one of the valence bonding orbitals and these fully occupied orbitals will become half-filled. Peaks M and N could represent absorptions to these half-filled bonding orbitals, and thus they are at lower energies than peaks A and B in the static absorption spectrum (Figure 3.1), which results from absorptions to antibonding orbitals. Dissociative ionization could also be a possibility,[33] but at this time we are not able to make a definitive assignment of peaks M and N.

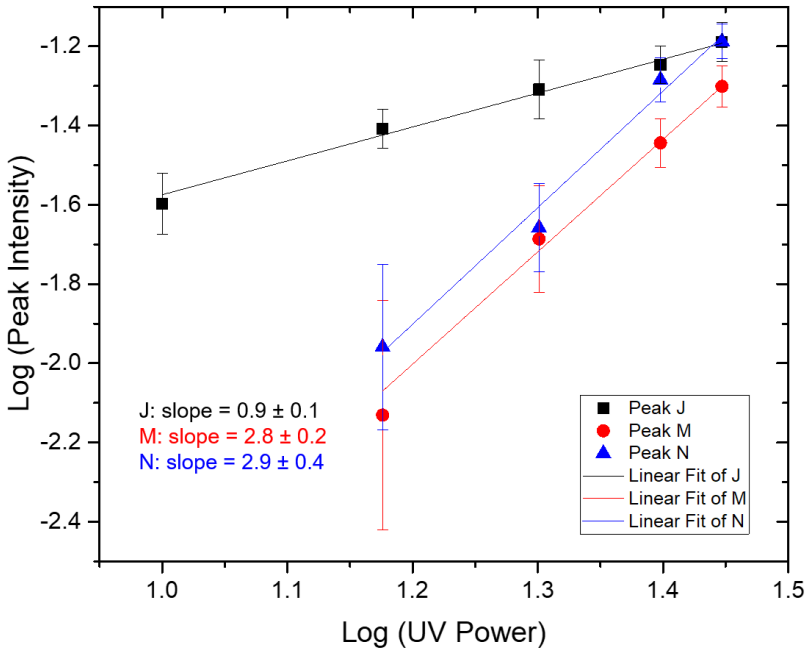

Figure 3.5 Power dependence studies of peaks J, M and N with respective log-log linear fits. While peak J results from linear absorption leading to photodissociation into the CH_2Cl radical, peaks M and N have a slope close to 3, an indicator of multiphoton effects.

Turning to the negative-going features, peak O matches the position of peak A in Figure 3.1. As the C-I bond is broken when CH_2ICl photodissociates at 266 nm, this depletion corresponds to the removal of the C(1s) → σ*(C-I) absorption of the parent molecule after the photodissociation process is complete. More intriguingly, negative features, peaks P at carbon and Q and R at chlorine also show up around the positions of C(1s) → σ*(C-Cl) and Cl(2p) → σ*(C-Cl), respectively (i.e. peaks B, F and G, respectively). The n(Cl) → σ*(C-Cl) transition leading to C-Cl bond cleavage occurs at ~170 nm, which should only contribute to a very minor portion of this depletion.[11] Changes in the C(1s), Cl (2p)→σ*(C-Cl) transition energies, however, are highly

likely, given that the reactant, CH_2ICl, and the product, CH_2Cl, exhibit changing electronic configurations of the carbon atom, which would perturb the energy levels of carbon 1s, chlorine 2p as well as σ*(C-Cl), as a result.

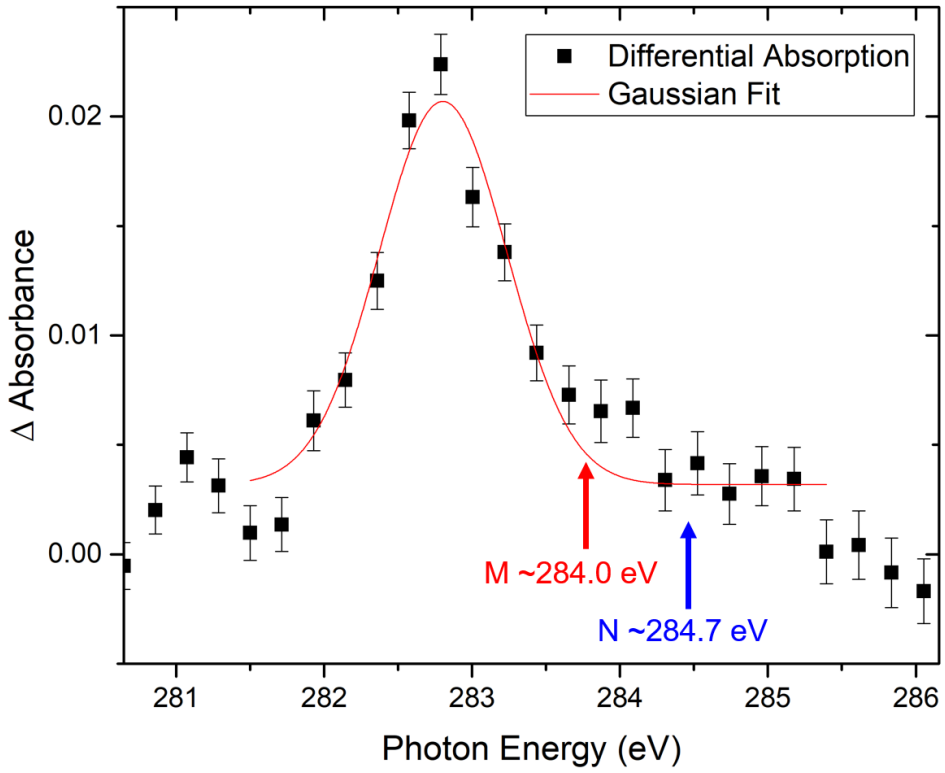

Figure 3.6 A representative spectra used to obtain an added back spectrum such as Figure 3.7; only a moderate UV power is used (15-20 μJ) and ion signals (M at ~284.0 eV and N at ~284.7 eV) are suppressed. Peak N completely disappears, while there is only a small contribution from Peak M.

In order to determine the exact shifts of the C(1s), $Cl(2p_{3/2})$, $Cl(2p_{1/2})$ → σ*(C-Cl) transitions, proportions of a static parent molecule spectrum are added back to the transient absorption spectrum (where only a moderate UV power is used so that the ion features M and N are suppressed as demonstrated in Figure 3.6) to obtain a pure spectrum of the photodissociation products; the added back spectral result is shown in Figure 3.7. The proportions are controlled so that the area around peak A approaches a baseline level, as no transition of C(1s) → σ*(C-I) from the parent molecule should be observed in the product.

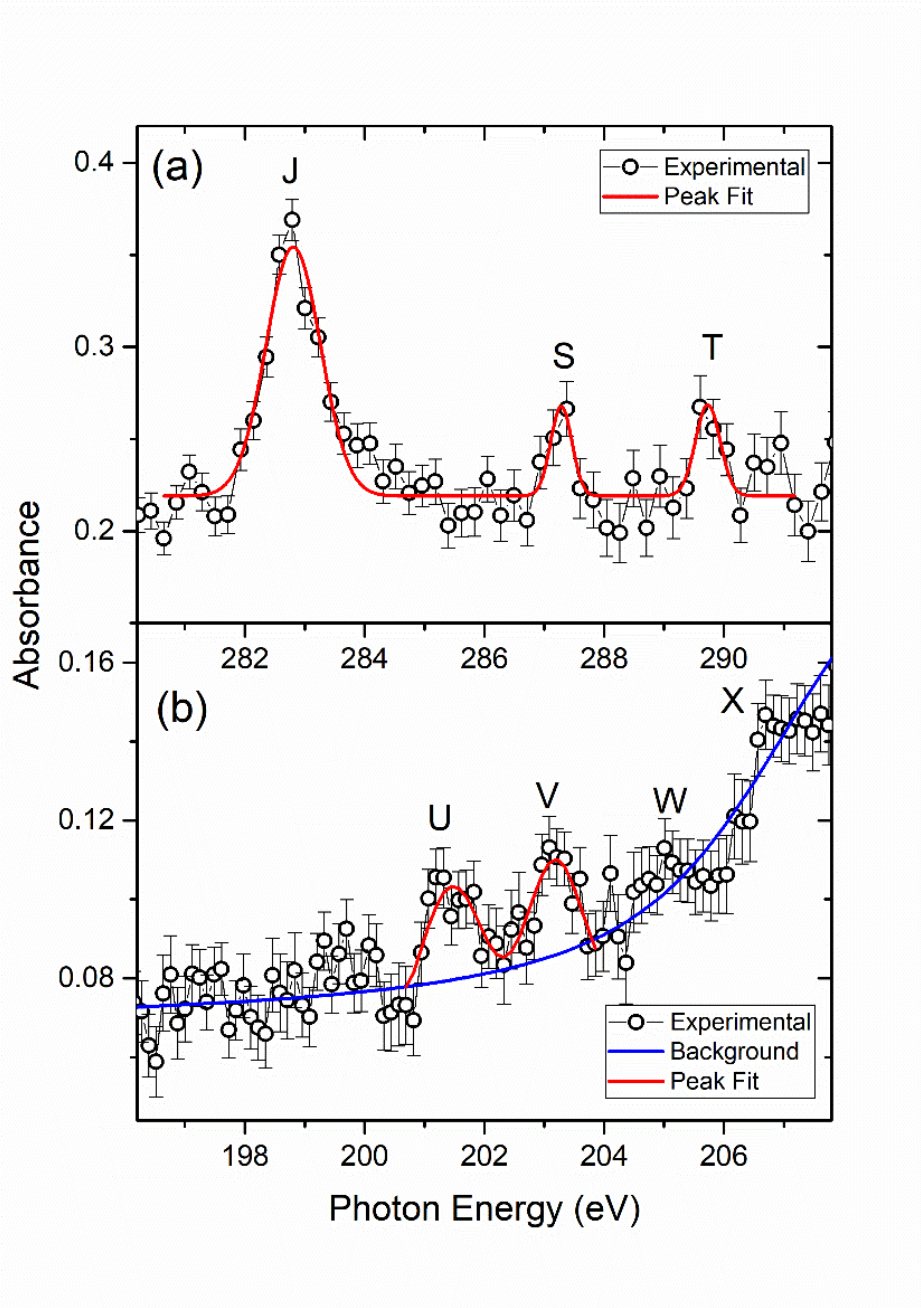

Figure 3.7 The summation of Figure 3.1 and Figure 3.3 spectra, respectively, with controlled proportion so that the signal corresponding to the C(1s)→σ*(C-I) transition in CH_2ICl is removed to the baseline level, which reveals the pure absorption spectrum of the photodissociation product, CH_2Cl, taken at low UV pump intensity so that the ion spectral features are minimized, at the (a) carbon K edge and (b) chlorine $L_{2,3}$ edges where the blue line is the extrapolated background and the red lines are peak fits. Peaks J, S-V are assigned in Table 3.3.

In the added back spectrum, peaks S and T become visible at the carbon K edge in the spectrum of the CH_2ICl photodissociation product. Peak S is assigned as C(1s) → σ*(C-Cl) of the

CH_2Cl radical; as removing the iodine atom from CH_2ICl will make the carbon nucleus less positively charged, hence more repulsive to the core electrons, the energy needed to promote electrons from the core level is decreased. Comparing to peak B, peak S is red shifted by 0.8 eV, similar to the energy difference for the C(1s) → σ*(C-Cl) transition between CH_3Cl and CH_2ICl, as demonstrated earlier in Table 3.1. Peak T is likely a blue-shifted version of peak C or a red shifted version of D, depending on the exact mixing nature of the Rydberg orbitals, which needs to be verified by further theoretical calculations.

Turning to the chlorine $L_{3,2}$ window, peaks U and V differ by ~1.8 eV, close to the spin-orbit splitting between $Cl_{3/2}$ and $Cl_{1/2}$ in CH_2ICl, and these peaks are assigned as Cl($2p_{3/2}$) → σ*(C-Cl) and Cl($2p_{1/2}$) → σ*(C-Cl), respectively. They are blue shifted by ~0.6 eV from peaks E and F. Another two shoulder features labeled W and X, also split by ~1.8 eV, resemble the Rydberg states G and I in Figure 1, also blue shifted. The C-Cl bond distance is shortened when the radicals are produced,[34-39] indicating a stronger C-Cl bond in the radical and thus greater absorption energies to σ*(C-Cl). While the iodine atom departs the dihalomethane molecule, the electron density withdrawn by the iodine atom is given back to the carbon atom and possibly also the chlorine atom, which could have resulted in a lower halogen core binding energy and red shifted Cl($2p_{1/2, 3/2}$) → σ*(C-Cl) resonances. The blue shift shows that shift in the valence bonding orbital is greater than the core shift in the chlorine atom, in contrast to the situation at the carbon atom.

Table 3.3 Summary of spectral features associated with CH_2Cl.[a]

Peak	Exptl. Energy (eV)	Assignment
J	282.8 ± 0.1	C(1s) → C(2p)
S	287.4 ± 0.2	C(1s) → σ*(C-Cl)
T	289.8 ± 0.3	C(1s) → σ*(C-H)
U	201.2 ± 0.3	Cl($2p_{3/2}$) → σ*(C-Cl)
V	203.0 ± 0.3	Cl($2p_{1/2}$) → σ*(C-Cl)

a Peak positions are reported as the average of at least three trials on different days and the error is one standard deviation of those trials convoluted with Gaussian fitting errors.

Transitions from multiple core shells are captured simultaneously in this experiment, in this case to a common antibonding orbital in the radical, as summarized by the energies in Table 3.3 and the scheme drawn in Figure 3.8. When CH_2ICl photodissociates into CH_2Cl at 266 nm, the C-Cl bond is strengthened, associated with a shift (ΔE_{σ^*}) in the valence σ*(C-Cl) orbital, reflected in the blue shift of the Cl($2p_{1/2, 3/2}$) → σ*(C-Cl) transitions. Meanwhile, the red shift in the C(1s)→ σ*(C-Cl) transition signifies that the shift in the carbon 1s core energy (ΔE_C) due to disappearance of the electron withdrawing effect from iodine is larger than the shift in σ*(C-Cl), i.e. $\Delta E_C - \Delta E_{\sigma^*}$ = ~0.8 eV.

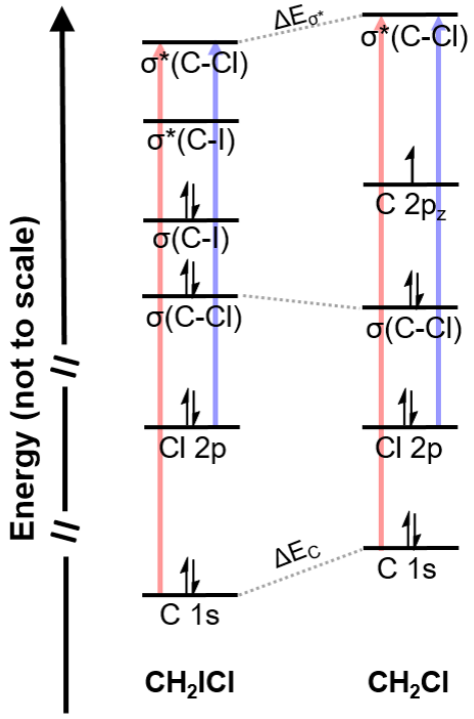

Figure 3.8 Schematic diagram of the molecular orbitals involved in the parent molecule CH_2ICl and the product CH_2Cl radical where C(1s)→σ*(C-Cl) is red shifted and Cl(2p)→σ*(C-Cl) blue shifted going from CH_2ICl to CH_2Cl.

3.1.4 Conclusion

Ultrafast core-level transient absorption spectroscopy combined with a selective bond breaking UV source has allowed the capture of transient radical species. As an example, photodissociation of CH_2ICl into CH_2Cl has been studied at both the carbon K edge and chlorine $L_{2,3}$ edge. The CH_2Cl radical produced from the CH_2ICl photodissociation at 266 nm is characterized by a prominent new carbon 1s→2p feature at 282.8±0.1 eV. The difference in the SOMO between the CH_3 and the CH_2Cl radical is explained by the electron withdrawing effect of chlorine. Removal of an iodine atom also changes the oxidation state of the carbon atom, well reflected in the absorption spectra of CH_2ICl and CH_2Cl at the carbon K edge, a manifestation of valence electrons screening core electrons. In contrast, it imposes only a secondary impact on the chlorine core where the changes in the valence antibonding orbital and shorter C-Cl bond distance govern the core-to-valence transitions in chlorine. This paves the way for further studies on radicals where various types of radicals can be produced by selective bond breaking and substitution or stabilization effects on the SOMO and other valence orbitals can be quantified.

3.2 The π Bonding Effect in CH_2Br

3.2.1 Introduction

Halogenated radicals are known for their anomalously short carbon-halogen bonds compared to their closed-shell analogues.[40] This has been attributed to the back-bonding effect between the carbon 2p and the outermost p shell of halogens, which together form a partial π bond. The heavier the halogen is, the more prominent is this partial bonding effect, due to the polarizability of the outermost p shells of halogens. Based on previous theoretical studies,[31, 41-42] a simple molecular orbital diagram with π bonding is illustrated in Figure 3.9, using the CH_2Br radical as an example, where the atomic carbon 2p forms a partial π bond with one of the bromine 4p orbitals.

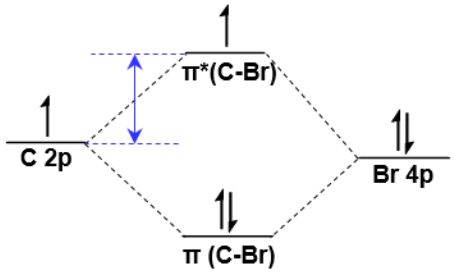

Figure 3.9 Molecular orbital picture to show the π bonding effect in the CH_2Br radical. The SOMO takes on the character of a π* orbital formed by the 2p of C and the 4p of Br. Adapted from reference 31.

In the simplest radical, CH_3, the SOMO (singly occupied molecular orbital) is dominated by a 2p orbital localized on the carbon atom.[43] In contrast, in halogenated radicals, the SOMO can become the half-filled π*(carbon-halogen) orbital. It is debatable whether the SOMO in CH_2Cl is purely atomic 2p in character or consists of π bonding, while calculations agree the SOMO in CH_2Br is an antibonding orbital formed by bromine 4p and carbon 2p with the most contribution from carbon 2p.[36, 41-42] Therefore the energy difference between a localized 2p orbital and the half-filled π*(carbon-halogen) orbital, indicated by the blue arrow in Figure 3.9, directly gives the strength of π bonding in a halogenated radical. Literature is available to characterize the bond distance in such radicals and to compute the bonding nature.[34, 36-37, 40-42] However, to our knowledge, there is no direct experimental evidence of how strong this effect can be.

Core-level spectroscopy at the carbon K edge, favoring transitions from carbon 1s to any p character orbital, by selection rules, is inherently advantageous in probing SOMOs in radicals. This has already been demonstrated in the case of CH_2Cl where the carbon 1s → SOMO transition is intense and well separated from other higher lying σ character orbitals. Consequently, this technique can be easily extended to study other halogenated radicals, such as CH_2Br, which can quantify the π bonding effect.

The preceding section has shown the capability of selective bond breaking to produce targeted radicals by utilizing the A band photodissociation of iodides. CH_2ICl photodissociation yields the CH_2Cl radical. Similarly, photodissociation of CH_2IBr can be used to yield the CH_2Br radical. However, the broad bands leading to C-I bond and the C-Br bond breaking occur at

relatively closer wavelengths, i.e. at 270 nm and 210 nm, respectively.[13, 31] The photodissoication of CH_2IBr at 267 nm into CH_2Br is thus accompanied by a small portion (20%[31]) of CH_2I.

3.2.2 Experimental Method

The experimental method resembles the one described in section 3.1.2. The CH_2IBr sample is purchased from Sigma-Aldrich and used at ~80 °C (vapor pressure ~100 Torr, entire gas line heated). The 266 nm ultraviolet (UV) pump beam is attenuated by an iris and focused by a 45-cm lens, where the pulse energy can be adjusted between 10-30 μJ and the pump intensity between 2-5×10^{11}W/cm^2.

A static absorption spectrum of a target gas is recorded with one second of camera exposure time and with the soft x-ray beam only, using the spectrum without the target gas as a background. The resultant spectrum of the parent molecule CH_2IBr, averaged over 64 such sets (64000 pulses in total with gas, 64000 without) for improved statistics.

$$\text{Absorbance}_{\text{target gas}} = -\log_{10} \frac{\text{flux}_{\text{x-ray}}(\text{with gas})}{\text{flux}_{\text{x-ray}}(\text{without gas})}$$

A transient absorption spectrum is recorded with one second of camera exposure time with both the pump UV and the probe soft x-ray beam, the delay time between which is controlled by a motorized stage to include 50 time points in between -300 fs (x-ray preceding UV) and 1000 fs (UV preceding x-ray), using the absorption spectrum without the pump UV beam as a background. The change between the two spectra yields a transient spectrum where

$$\Delta\text{Absorbance}_{\text{target gas, delay timepoint}} = -\log_{10} \frac{\text{flux}_{\text{x-ray}}(\text{with gas, with UV})}{\text{flux}_{\text{x-ray}}(\text{with gas, without UV})}$$

and averaged over at least 32 such sets (32000 pulses with UV, 32000 pulses without UV at each time delay point) for statistics, which takes typically two hours for 50 time delay points overall.

3.2.3 Results and Discussion

3.2.3.1 Static soft x-ray absorption spectra of CH_2IBr

Figure 3.10 shows a representative static absorption spectrum of CH_2IBr at the carbon K (1s) edge. To our knowledge, no C K edge absorption spectra of CH_2IBr have been reported and assignments are based on peaks observed in similar halogenated molecules (CH_3Br and CH_3I) shown in Table 3.4.

Peaks a and b are separated by 0.8 eV, close to the difference between the reported values for the C(1s) → σ*(C-I) transition in CH_3I and the C(1s) → σ*(C-Br) transition in CH_3Br from electron scattering studies.[17] This leads to the assignment of peak a to the C(1s) → σ*(C-I) transition and peak b to C(1s) → σ*(C-Br) in CH_2IBr. Additionally, peaks a and b are ~0.9 eV blue shifted from the C(1s) → σ*(C-I) in CH_3I and the C(1s) → σ*(C-Cl) in CH_3Br, respectively.

Similar to the case of CH_2ICl, the ~0.9 eV shifts from the monohalomethanes are understood as the additional electron withdrawing effect from the central carbon atom because there are two halogen atoms instead of one.

In summary, by promoting an electron from one of the core orbitals to various vacant valence orbitals, core-level spectroscopy provides insights into the relative difference among the valence orbitals.

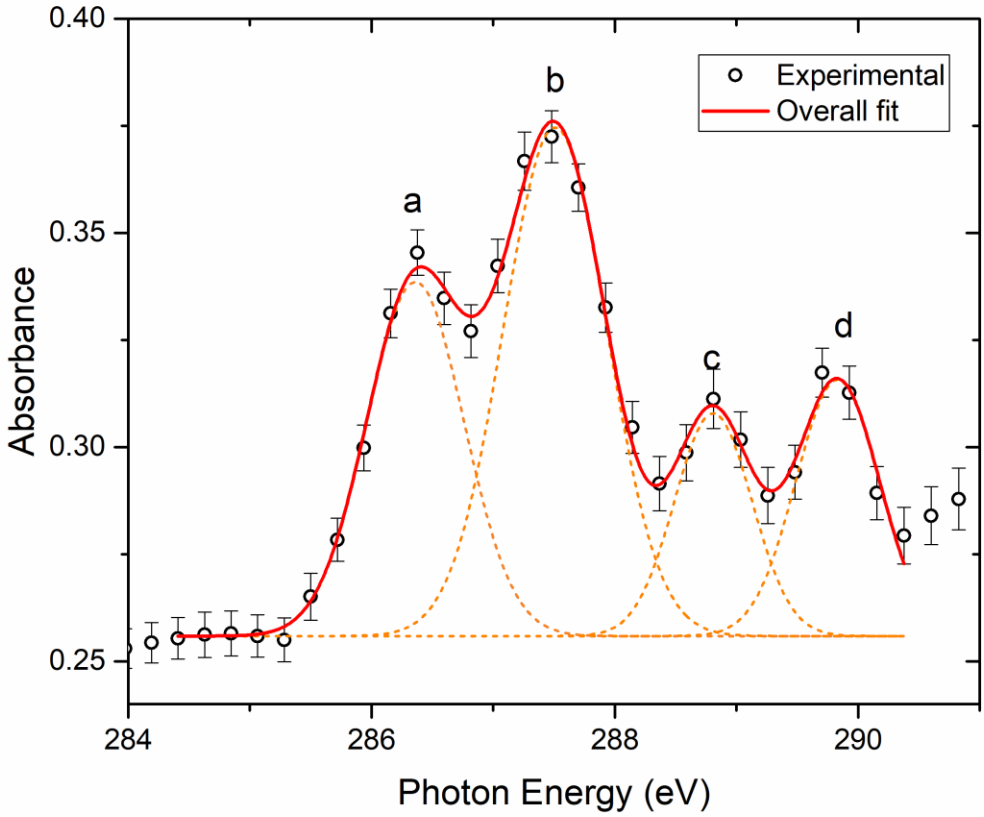

Figure 3.10 Static absorption spectrum of CH_2IBr at the carbon K edge where the orange dashed lines are Gaussian fits to the peaks and the red solid line is the summation of all the fitted peaks. Peaks a-d are assigned as in Table 3.4.

Table 3.4 Assignments of spectral features observed at C K edge of CH_2IBr.

Peak	Exptl. Energy (eV)	Exptl. Ref. Energy (eV) (Ref. Molecule)	Assignment
a	286.3 ± 0.1	285.6 (CH_3I)[17]	C(1s) → σ*(C-I)
b	287.5 ± 0.1	286.5 (CH_3Br)[17]	C(1s) → σ*(C-Br)
c	288.8 ± 0.1	-	C(1s) → σ*(C-H)
d	289.8 ± 0.1	-	C(1s) → σ*(C-H)

3.2.3.2 Transient Absorption Spectra of CH_2IBr: Formation of CH_2Br Radical as a Photodissociation Product

A representative transient absorption spectrum of CH_2IBr obtained as mentioned earlier and integrated at long delay time points between 350 fs and 1000 fs are shown in Figure 3.11. CH_2IBr is known to have a C-I bond dissociation timescale of 100 fs,[13, 31] as verified by the temporal dependence of the features shown in Figure 3.12. Hence at 350 fs, long after the photodissociation is complete, the spectrum reflects absorption of the photodissociation products and depletion of the parent molecule. According to previous photodissociation studies, 80% of the products is CH_2Br + I/I* and 20% CH_2I + Br/Br*. Therefore at the carbon K edge, the photofragment that can be observed is dominated by CH_2Br.

A new strong positive feature in the carbon K edge region at 282.6±0.1 eV, peak e, is observed and accompanied by a weaker feature, peak f, at ~284.2 eV. Peak e is attributed to the transition of C(1s) → SOMO in the CH_2Br radical, as the SOMO of the radical is singly occupied and its p orbital character strongly favored by selection rules, whether it is an atomic 2p orbital or a partial π bond. There is a small shoulder on the left of peak e, which might be the signature of C(1s) → SOMO in the CH_2I radical. However, this remains to be reproduced with improved spectral resolution. Experiments done at higher UV powers as shown in Figure 3.13 suggest that peak f and another feature, peak g (at ~283.7 eV, which shows up only at high UV powers), result from multiphoton effects, possibly ionization of CH_2IBr.

Peak e, the C(1s) → SOMO transition, is 1.3 eV higher in energy than the C(1s) → C(2p) transition observed in CH_3.[30] This difference of 1.3 eV can be partially explained by the electron withdrawing effect of bromine on the carbon atom. There is a 1.0 eV difference in the carbon 1s ionization potential (IPs) between CH_4 (290.8 eV) and CH_3Br (291.8 eV) reported in the x-ray photoelectron spectroscopy literature,[27] which indicates that the mere electron withdrawing effect will lead to a 1.0 eV difference in the C(1s) → SOMO transition between CH_3 and CH_2Br. The π bonding effect in CH_2Br can thus be quantified, i.e. the rest the 0.3±0.1 eV difference is caused the π bonding effect in CH_2Br.

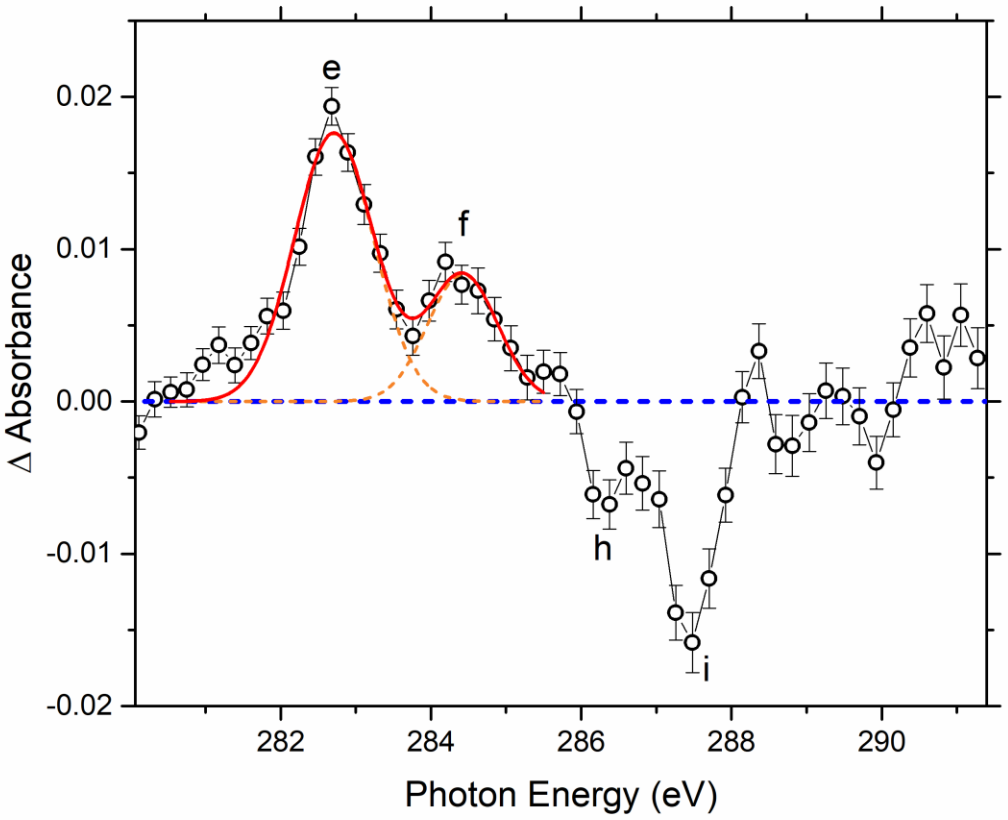

Figure 3.11 Transient absorption spectra of CH_2IBr at the carbon K edge where the orange lines are deconvoluted Gaussian peaks and the red line is the summation of all the fitted peaks. The blue line is the reference zero line. Positive-going features represent new species that occur when UV light excites and dissociates CH_2IBr and negative features indicate changes in the static spectrum when the CH_2IBr molecules are depleted by UV excitation.

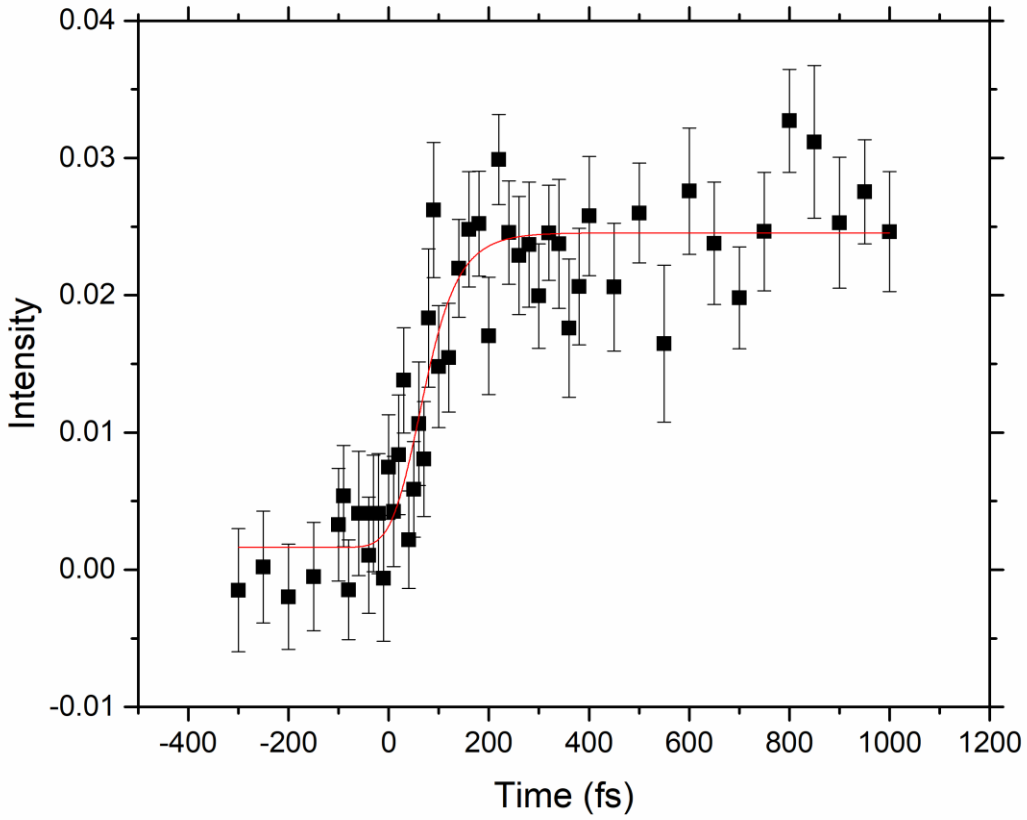

Figure 3.12 Temporal dependence of peak e, which is fit with an exponential rise convoluted with a 90-fs instrumental response. The photodissociation is complete after ~150 fs.

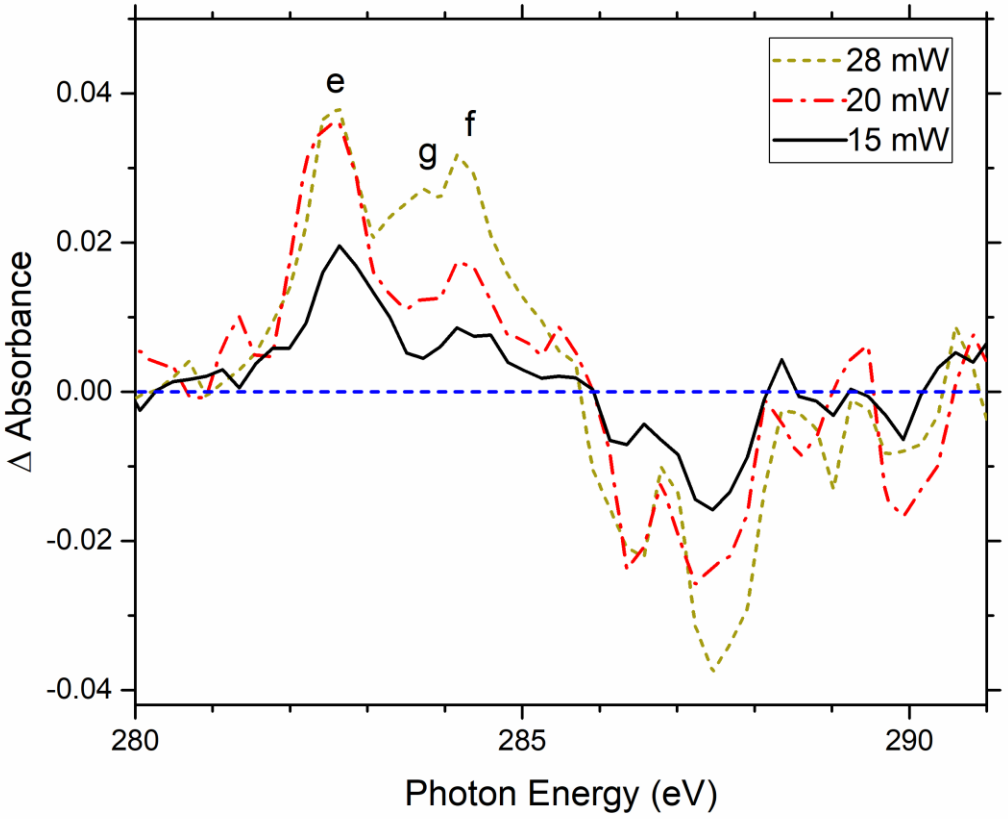

Figure 3.13 Experiments done at various UV powers to power dependence of peaks e, f and g. The legend denotes the UV power used in each experiment. The blue line is the zero reference line. This shows that peak e results from linear absorption, leading to photodissociation into the CH_2Br radical, while peaks f and g result from multiphoton effects, possibly ionization of the parent molecule CH_2IBr.

Comparing to the case of CH_2Cl where the difference in the C(1s) → SOMO transition between CH_3 and CH_2Cl (1.5 eV) is very close to the difference in the carbon 1s IP between CH_4 (290.8 eV) and CH_3Cl (292.3 eV), this result also suggests that the SOMO peak position observed in CH_2Cl is largely atomic carbon 2p orbital, with the possibility of the π bonding effect embedded in its broad structure. Figure 3.14 compares the relative positions of the molecular orbitals across the three radicals. The electron withdrawing effect changes the ionization potential of the central carbon, thus affecting the state where the 1s electron is excited from. On the other hand, the π bonding effect impacts the valence orbital, in particular the SOMO, and takes control over the state where the 1s electron will be excited to.

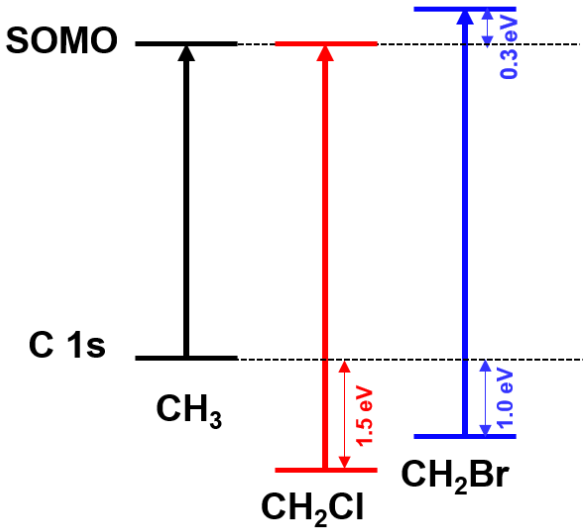

Figure 3.14 Molecular orbitals of CH_3, CH_2Cl and CH_2Br, separating the electron-withdrawing and the π bonding effects. The π bonding effect is not clearly observed in the CH_2Cl radical and thus the SOMO is dominated by an atomic carbon 2p orbital. The core 1s orbital is shifted due to the electron withdrawing effect (1.5 eV). The SOMO in CH_2Br is attenuated by the π bonding (0.3 eV) and the core 1s orbital is shifted by 1.0 eV due to the electron-withdrawing effect.

Turning to the negative features, peaks h and i are close to the position of peaks a and b, respectively, in the static absorption spectrum of CH_2IBr. This indicates that the C(1s) → σ*(C-I) and the C(1s) → σ*(C-Br) transitions in CH_2IBr are depleted. Peak a is depleted as the C-I bond breaking is the major photodissociation pathway at 267 nm. There are two reasons why peak b is depleted: (1) the C-Br bond is broken because of the minor photodissociation pathway; (2) the C(1s) → σ*(C-Br) transition in the CH_2Br radical is different from that in CH_2IBr, similar to the shift of the C(1s) → σ*(C-Cl) transition in the case of CH_2ICl photodissociating to CH_2Cl. On the other hand, the relative ratio of peaks h and i differs from that of peaks a and b, hinting the possible presence of other transitions overlapped with depletion of peaks a and b. To recover hidden transitions, a proportion of the static absorption spectrum (i.e. Figure 3.10) is added back to the transient absorption spectrum (i.e. Figure 3.11). The proportion is controlled so that the baseline in the 285-290 eV region is close to the baseline in the 280-285 eV region, which is shown in Figure 3.15.

Three new features show up in the added back spectrum, peaks j, k and l. It is worth cautioning that the transient absorption spectrum (Figure 3.11) is not free of ion signals, so all these peaks could possibly correspond to the transitions to higher lying states in CH_2IBr^+. This adding back technique is not as accurate in the high UV power schemes as it is in the low UV power ones, since the baseline cannot be easily determined. By comparing the results at Br $M_{4,5}$ edges where the Br($3d_{5/2}$)→π*(C-Br) and Br($3d_{5/2}$)→σ*(C-Br) transitions in CH_2Br differ by ~3 eV, peak j at 285.8 eV, which is also ~3 eV away from the C(1s)→π*(C-Br) transition at 282.6 eV, could possibly be understood as the C(1s)→ σ*(C-Br) transition in CH_2Br. On the other hand, peak k is ~0.9 eV away from peak b, the C(1s)→σ*(C-Br) transition in the parent molecule CH_2IBr.

As seen in the case of CH_2ICl, removal of the iodine atom causes a ~0.8 eV shift in the C(1s)→σ*(C-Cl) transition from the parent molecule to the radical. Therefore peak k could also be a candidate for the C(1s)→σ*(C-Br) transition in CH_2Br. Peak m could be a shifted peak c or an ion peak. Experiments in ion-free conditions (i.e. with low UV power and high signal-to-noise ratio) need to be repeated and computational efforts made in order to confirm the peak assignments.

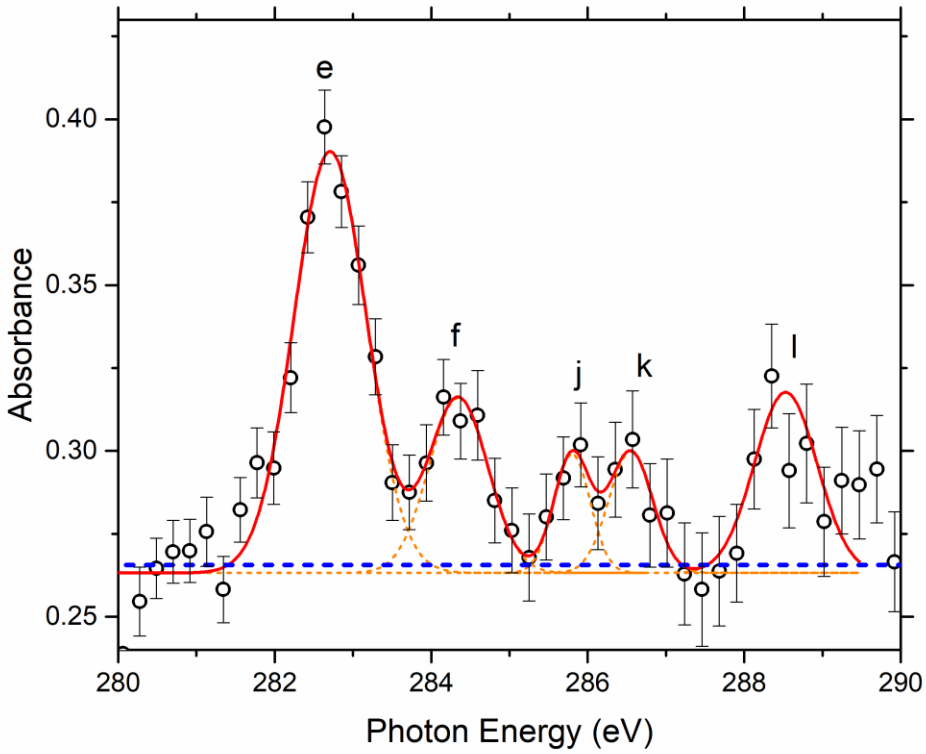

Figure 3.15 The summation of Figure 3.10 and Figure 3.11, with a controlled proportion so that the baseline level in the 285-290 eV region is close to that in the 280-285 eV region. Based on this proportion, about 14% of the parent molecules are excited in this photodissociation process. The blue line corresponds to the baseline level.

The peak assignments from the transient absorption spectrum and the added back spectrum are summarized in Table 3.4.

Table 3.4 Assignments of spectral features observed after photodissociation of CH_2IBr.

Peak	Energy (eV)	Transition
e	282.6	C(1s) → SOMO in CH_2Br
f	284.2	CH_2IBr^+
g	283.7	CH_2IBr^+
j	285.8	C(1s) → σ*(C-Br) in CH_2Br / CH_2IBr^+
k	286.6	C(1s) → σ*(C-Br) in CH_2Br / CH_2IBr^+
l	288.3	C(1s) → σ*(C-H) in CH_2Br / CH_2IBr^+

Comparison with experimental results at the other edges not only guides the peak assignments at the carbon K edge, but also puts forward intriguing questions. Table 3.5 recapitulates the transitions in CH_2IBr and CH_2Br observed at Br $M_{4,5}$ edges.[31] By inspecting the transitions within the same species, e.g. CH_2Br, the difference between σ*(C-Br) and π*(C-Br) observed at bromine M_5 edge is found to be similar to that observed at the carbon K edge (if peak j is taken as the C(1s) → σ*(C-Br) transition). However, when comparing the results across different species at different edges, the orbital difference is not conserved, e.g. the difference between C(1s)→σ*(C-Br) in CH_2IBr (peak b, 287.5 eV) and C(1s)→π*(C-Br) (peak e, 282.6 eV) are ~5 eV apart whereas Br($3d_{5/2}$)→σ*(C-Br) in CH_2IBr (70.5 eV) and Br($3d_{5/2}$)→π*(C-Br) in CH_2Br (68.5 eV) are only ~2 eV apart, where there is a non-negligible gap. This implies the two atomic cores are differently impacted during the photodissociation reaction. One obvious factor to explain this gap is the electron withdrawing effect, which influences the carbon core significantly, but the bromine core to a much less degree. Nevertheless pure electron withdrawing effect will lead to a 1-2 eV shift as seen consistently in the preceding sections. Other factors play a role but are yet to be investigated by high-level calculations.

Table 3.5 Summary of transitions observed in CH_2IBr and CH_2Br at Br $M_{4,5}$ edges

Species	Transition	Energy (eV)
CH_2IBr	Br($3d_{5/2}$)→σ*(C-Br)	70.5
CH_2IBr	Br($3d_{3/2}$)→σ*(C-Br)	71.5
CH_2Br	Br($3d_{5/2}$)→π*(C-Br)	68.5
CH_2Br	Br($3d_{3/2}$)→π*(C-Br)	69.5
CH_2Br	Br($3d_{5/2}$)→σ*(C-Br)	~71.5[a]

a Due to spectral limit in this study, this peak is only an approximate position; the Br($3d_{5/2}$)→σ*(C-Br) in CH_2Br is also beyond the limit and thus not observed.

3.2.4 Conclusion

Photodissociation of CH_2IBr into CH_2Br observed at the carbon K edge elucidates the strength of the π bonding effect in halogenated radicals. By comparing the carbon 1s→SOMO transitions in CH_3, CH_2Cl and CH_2Br, the π bonding effect is quantified to be ~0.3±0.1 eV in CH_2Br and not clearly observed in CH_2Cl. This showcases the capability of core-level spectroscopy at the carbon K edge in identifying substitution and stabilization effects on the SOMO. Aided by the experimental results at bromine $M_{4,5}$ edges, this study also suggests how different atomic cores might be impacted differently in a given chemical reaction, thus affecting the relative difference observed among valence orbitals across different species.

3.3 Bibliography

1. Marshall, P.; Srinivas, G. N.; Schwartz, M., A computational study of the thermochemistry of bromine- and iodine-containing methanes and methyl radicals. *J Phys Chem A* **2005,** *109* (28), 6371-6379.
2. Olleta, A. C.; Lane, S. I., Ab initio studies of the gas-phase thermodynamic properties and bond dissociation energies for haloethanes and halomethyl radicals. *Phys Chem Chem Phys* **2001,** *3* (5), 811-818.
3. Hung, S. L.; Pfefferle, L. D., A Flow Tube Kinetics Study of Methyl-Chloride Oxidation. *Combust Sci Technol* **1993,** *87* (1-6), 91-107.
4. Violi, A.; D'Anna, A.; D'Alessio, A., A modeling evaluation of the effect of chlorine on the formation of particulate matter in combustion. *Chemosphere* **2001,** *42* (5-7), 463-471.
5. Molina, M. J.; Rowland, F. S., Stratospheric Sink for Chlorofluoromethanes - Chlorine Atomic-Catalysed Destruction of Ozone. *Nature* **1974,** *249* (5460), 810-812.
6. Enami, S.; Hoffmann, M. R.; Colussi, A. J., Halogen Radical Chemistry at Aqueous Interfaces. *J Phys Chem A* **2016,** *120* (31), 6242-6248.
7. Rattigan, O. V.; Shallcross, D. E.; Cox, R. A., UV absorption cross-sections and atmospheric photolysis rates of CF_3I, CH_3I, C_2H_5I and CH_2ICl. *J Chem Soc Faraday T* **1997,** *93* (16), 2839-2846.
8. Attar, A. R.; Bhattacherjee, A.; Pemmaraju, C. D.; Schnorr, K.; Closser, K. D.; Prendergast, D.; Leone, S. R., Femtosecond x-ray spectroscopy of an electrocyclic ring-opening reaction. *Science* **2017,** *356* (6333), 54-58.
9. Bhattacherjee, A.; Das Pennaraju, C.; Schnorr, K.; Attar, A. R.; Leone, S. R., Ultrafast Intersystem Crossing in Acetylacetone via Femtosecond X-ray Transient Absorption at the Carbon K-Edge. *J Am Chem Soc* **2017,** *139* (46), 16576-16583.
10. Pertot, Y.; Schmidt, C.; Matthews, M.; Chauvet, A.; Huppert, M.; Svoboda, V.; von Conta, A.; Tehlar, A.; Baykusheva, D.; Wolf, J. P.; Worner, H. J., Time-resolved x-ray absorption spectroscopy with a water window high-harmonic source. *Science* **2017,** *355* (6322), 264-+.
11. Senapati, D.; Kavita, K.; Das, P. K., Photodissociation dynamics of CH2ICl at 222, 236, 266, 280, and-304 nm. *J Phys Chem A* **2002,** *106* (36), 8479-8482.
12. Murillo-Sanchez, M. L.; Poullain, S. M.; Gonzalez-Vazquez, J.; Corrales, M. E.; Balerdi, G.; Banares, L., Femtosecond photodissociation dynamics of chloroiodomethane in the first absorption band. *Chem Phys Lett* **2017,** *683*, 22-28.
13. Murillo-Sánchez, M. L.; Marggi Poullain, S.; Bajo, J. J.; Corrales, M. E.; González-Vázquez, J.; Solá, I. R.; Bañares, L., Halogen-atom effect on the ultrafast photodissociation dynamics of the dihalomethanes CH_2ICl and CH_2BrI. *Phys Chem Chem Phys* **2018,** *20* (32), 20766-20778.
14. King, G. C.; Tronc, M.; Read, F. H.; Bradford, R. C., Investigation of Structure near $L_{2,3}$ Edges of Argon, $M_{4,5}$ Edges of Krypton and $N_{4,5}$ Edges of Xenon, Using Electron-Impact with High-Resolution. *J Phys B-at Mol Opt* **1977,** *10* (12), 2479-2495.
15. Hedin, L.; Eland, J. H. D.; Karlsson, L.; Feifel, R., An x-ray absorption and a normal Auger study of the fine structure in the S $2p^{-1}$ region of the CS_2 molecule. *J Phys B-at Mol Opt* **2009,** *42* (8).
16. Wight, G. R.; Brion, C. E., K- and Lii,Iii-Shell Excitations in CS_2 and COS by 2.5 Kev Electron-Impact. *J Electron Spectrosc* **1974,** *4* (4), 335-345.
17. Hitchcock, A. P.; Brion, C. E., Assignment of the Carbon K-Shell Spectra of the Methyl Halides. *J Electron Spectrosc* **1979,** *17* (3), 139-147.

18. Saeh, J. C.; Stanton, J. F., Application of an equation-of-motion coupled cluster method including higher-order corrections to potential energy surfaces of radicals. *J Chem Phys* **1999,** *111* (18), 8275-8285.
19. Stanton, J. F.; Gauss, J., A simple correction to final state energies of doublet radicals described by equation-of-motion coupled cluster theory in the singles and doubles approximation. *Theor Chim Acta* **1996,** *93* (5), 303-313.
20. Dyall, K. G., Interfacing relativistic and nonrelativistic methods .1. Normalized elimination of the small component in the modified Dirac equation. *J Chem Phys* **1997,** *106* (23), 9618-9626.
21. Liu, W. J.; Peng, D. L., Exact two-component Hamiltonians revisited. *J Chem Phys* **2009,** *131* (3).
22. Cheng, L.; Gauss, J., Analytic energy gradients for the spin-free exact two-component theory using an exact block diagonalization for the one-electron Dirac Hamiltonian. *J Chem Phys* **2011,** *135* (8).
23. Roos, B. O.; Lindh, R.; Malmqvist, P. A.; Veryazov, V.; Widmark, P. O., New relativistic ANO basis sets for transition metal atoms. *J Phys Chem A* **2005,** *109* (29), 6575-6579.
24. Stanton, J. F.; Gauss, J.; Cheng, L.; Harding, M. E.; Matthews, D. A.; Szalay, P. G., CFOUR, coupled-cluster techniques for computational chemistry, www.cfour.de (accessed August 1, 2018)
25. Musial, M.; Kucharski, S. A.; Bartlett, R. J., Equation-of-motion coupled cluster method with full inclusion of the connected triple excitations for ionized states: IP-EOM-CCSDT. *J Chem Phys* **2003,** *118* (3), 1128-1136.
26. Hitchcock, A. P.; Brion, C. E., Inner-Shell Excitation and Exafs-Type Phenomena in Chloromethanes. *J Electron Spectrosc* **1978,** *14* (6), 417-441.
27. Hitchcock, A. P.; Brion, C. E., Inner Shell Excitation of CH_3F, CH_3Cl, CH_3Br and CH_3I by 2.5 Kev Electron-Impact. *J Electron Spectrosc* **1978,** *13* (3), 193-218.
28. Osullivan, G., Chlorine L-Edge Absorption in CCl_4 and CCl_2F_2. *J Phys B-at Mol Opt* **1982,** *15* (15), 2385-2390.
29. Degroot, F. M. F., Differences between L_3 and L_2 X-Ray-Absorption Spectra. *Physica B* **1995,** *208* (1-4), 15-18.
30. Alagia, M.; Lavollee, M.; Richter, R.; Ekstrom, U.; Carravetta, V.; Stranges, D.; Brunetti, B.; Stranges, S., Probing the potential energy surface by high-resolution x-ray absorption spectroscopy: The umbrella motion of the core-excited CH_3 free radical. *Phys Rev A* **2007,** *76* (2).
31. Attar, A. R.; Piticco, L.; Leone, S. R., Core-to-valence spectroscopic detection of the CH_2Br radical and element-specific femtosecond photodissociation dynamics of CH_2IBr. *J Chem Phys* **2014,** *141* (16).
32. Lago, A. F.; Kercher, J. P.; Bodi, A.; Sztaray, B.; Miller, B.; Wurzelmann, D.; Baer, T., Dissociative photoionization and thermochemistry of dihalomethane compounds studied by threshold photoelectron photoion coincidence spectroscopy. *J Phys Chem A* **2005,** *109* (9), 1802-1809.
33. Loh, Z. H.; Leone, S. R., Ultrafast strong-field dissociative ionization dynamics of CH_2Br_2 probed by femtosecond soft x-ray transient absorption spectroscopy. *J Chem Phys* **2008,** *128* (20).
34. Li, Z. J.; Francisco, J. S., High level ab initio molecular orbital study of the structures and vibrational spectra of CH_2Br and CH_2Br^+. *J Chem Phys* **1999,** *110* (2), 817-822.
35. Bailleux, S.; Duflot, D.; Taniguchi, K.; Sakai, S.; Ozeki, H.; Okabayashi, T.; Bailey, W. C., Fourier Transform Microwave and Millimeter-Wave Spectroscopy of Bromoiodomethane, CH_2BrI. *J Phys Chem A* **2014,** *118* (50), 11744-11750.

36. Li, Y. M.; Francisco, J. S., CASSCF and MRCl studies of the electronic excited states of CH_2Cl and CH_2Br. *J Chem Phys* **2001,** *114* (7), 2879-2882.
37. Levchenko, S. V.; Krylov, A. I., Electronic structure of halogen-substituted methyl radicals: Equilibrium geometries and vibrational spectra of CH_2Cl and CH_2F. *J Phys Chem A* **2002,** *106* (20), 5169-5176.
38. Kim, H.; Park, Y. C.; Lee, Y. S., Spin-orbit Effects on the Structure of Haloiodomethane Cations CH_2XI^+ (X=F, Cl, Br, and I). *B Korean Chem Soc* **2014,** *35* (3), 775-782.
39. Ohkoshi, I.; Niide, Y.; Takano, M., Microwave-Spectrum and Quadrupole Coupling-Constant Tensor of Chloroiodomethane. *J Mol Spectrosc* **1987,** *124* (1), 118-129.
40. Frenking, G.; Fau, S.; Marchand, C. M.; Grutzmacher, H., The pi-donor ability of the halogens in cations and neutral molecules. A theoretical study of AX_3^+, AH_2X^+, YX_3, and YH_2X (A=C, Si, Ge, Sn, Pb; Y=B, Al, Ga, In, Tl; X=F, Cl, Br, I). *J Am Chem Soc* **1997,** *119* (28), 6648-6655.
41. Levchenko, S. V.; Krylov, A. I., Electronic structure of halogen-substituted methyl radicals: Excited states of CH_2Cl and CH_2F. *J Chem Phys* **2001,** *115* (16), 7485-7494.
42. Pakiari, A. H.; Azami, S. M., A localized picture of back bonding in $CH_{3-n}X_n$ (X = F, Cl and Br; n=1, 2 or 3) radical and cation systems. *J Mol Struc-Theochem* **2009,** *901* (1-3), 96-102.
43. Fleming, I., *Molecular Orbitals and Organic Chemical Reactions*. Student ed.; John Wiley & Sons: Chichester, U.K., 2009.

Chapter 4. Core-Level Spectroscopic Studies of Alkyl Substituted Radicals – The Methyl, Ethyl, Isopropyl and Tert-Butyl Radical

4.1 Introduction

Radicals, characterized by partially filled orbitals, i.e. singly occupied molecular orbital (SOMO), have triggered much interest due to their transient nature and ubiquitous role in chemical reactivity.[1-4] Methyl substituted radicals represent the simplest class of radicals. From a planar geometry in the methyl radical ($\cdot CH_3$) to a slightly non-planar geometry in the tert-butyl radical,[5] the increasing stability due to factors such as hyperconjugation and resonance[6] has invoked research into their structures, molecular orbitals, ionization energies and valence absorption spectra.[5-9] Results on radicals are often convoluted with higher-lying states in the valence shell and complications within ionic states that could be nearby. Nevertheless it is crucial to resolve how the SOMOs of the radicals are changed by substitution from a fundamental perspective. Core-level spectroscopy, with its element specificity and sensitivity to chemical environment, will provide such insights. Recent progress toward core-level spectroscopy centered on the carbon K edge demonstrates the power of using x-ray spectroscopic techniques to study the dynamics and the electronic structures of transient species.[10-12] As core-level transitions involve both core and valence orbitals, employing core-level spectroscopy to substituted radicals will demonstrate the impact of substitution on both core orbitals and valence shells.

Moreover, ultrafast laser techniques, especially transient absorption spectroscopy, provide a robust way to study short-lived reaction intermediates. Selective bond-breaking, made possible by photodissociation at a specific wavelength, produces desirable transient species in a consistent fashion. In particular, the C-I bond, known to dissociate at approximately 270 nm, can be utilized to form specific radicals from iodine-containing organic molecules. Figure 4.1 shows the uniform broad absorption bands across different iodides.[13-16] With ultraviolet (UV) radiation centered at 260-270 nm, one electron is promoted from the non-bonding iodine 5p orbital to a σ*(C-I) antibonding orbital, leading to repulsive states and photodissociation into a radical and an iodine atom or its spin excited counterpart.[17-18] Therefore to study a series of alkyl-substituted radicals, a series of alkyl substituted iodides is used as the parent molecules of photodissociation as listed in Table 4.1.

Combining core-level spectroscopy at the carbon K edge and transient absorption techniques, i.e. core-level transient absorption spectroscopy, various radicals can be studied at the carbon K edge to understand their fingerprints in core-to-valence transitions.

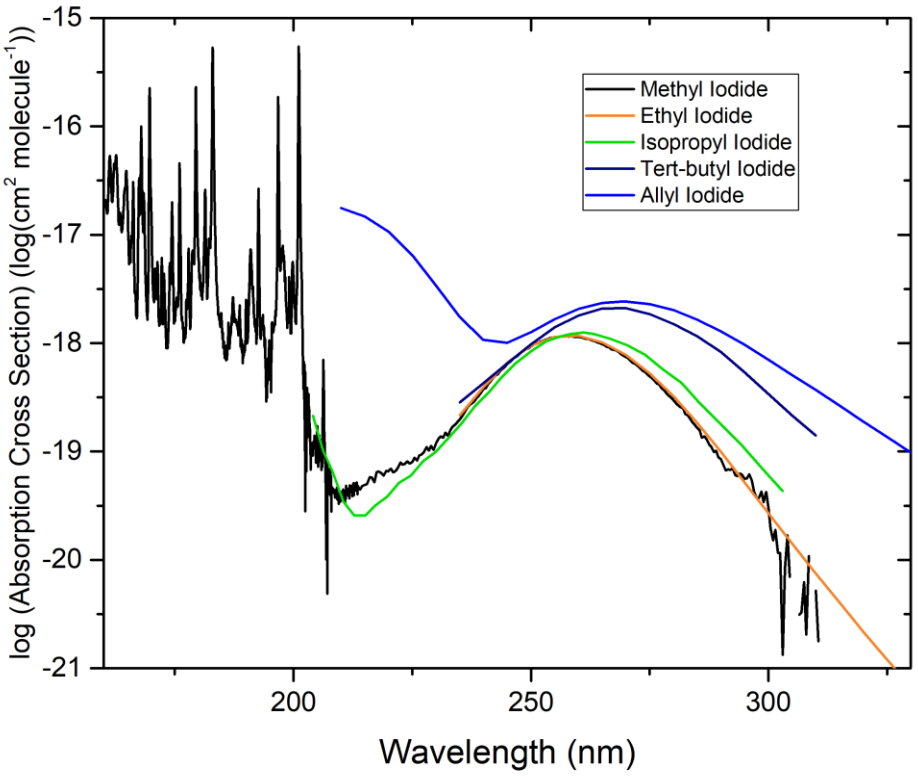

Figure 4.1 Ultraviolet absorption spectra of various iodides.[13-16] The uniform broad band absorption peaking at 260-270 cm corresponds to the A band photodissocation leading to radical production.

Table 4.1 Summary of alkyl substituted iodides and the radicals to be produced through photodissociation.

Parent Molecule	Radical	Chemical Formula
Methyl iodide	Methyl	$\cdot CH_3$
Ethyl iodide	Ethyl	$\cdot CH_2CH_3$
Isopropyl iodide	Isopropyl	$\cdot CH(CH_3)_2$
Tert-butyl iodide	Tert-butyl	$\cdot C(CH_3)_3$

4.2 Experimental Method

The apparatus to generate the pump pulse of 266 nm and broadband x-ray probe pulse has been described in the previous chapters. In brief, the output of a 12 mJ per pulse, 800 nm-centered, 1 kHz repetition rate, 35-fs Ti:Sapphire femtosecond laser is split into two branches in a 9:1 ratio.

The 10% branch is used to produce third harmonic generation with two non-linear crystals to generate ultraviolet pulses centered at around 266 nm. The other 90% is used as a pump for a tunable traveling-wave optical parametric amplifier of superfluorescence (TOPAS), which is tuned to output infrared light at 1320 nm with a pulse energy of 2.5-2.8 mJ. These near infrared pulses are subsequently focused by a 40-cm lens into a semi-infinite gas cell filled with 750-800 Torr of helium to emit soft x-ray light ranging from 150 eV to 300 eV through the high harmonic generation (HHG) process. The residual infrared light is blocked by a 100 nm thick aluminum filter whereas the soft x-ray radiation is transmitted and further focused by a toroidal mirror. The 266 nm ultraviolet (UV) pump beam is attenuated by an iris and focused by a 45-cm lens where the pulse energy can be adjusted between 10-30 μJ and the pump intensity between $2\text{-}5\times10^{11}$ W/cm^2. The soft x-ray and the UV beam overlap at an angle of approximately one degree within a flowing gas cell containing the methyl iodide, ethyl iodide, isopropyl iodide or tert-butyl iodide sample purchased from Sigma-Aldrich (vapor pressure 50~100 Torr) after freeze-pump-thaw degassing. The soft x-ray beam is transmitted by the gas cell, diffracted by an x-ray grating onto a charged-couple device (CCD) camera chip with 1340×400 pixels and the UV beam is blocked by a 100 nm thick titanium filter after the gas cell to block pump scattering.

A static absorption spectrum of a target gas is recorded with one second of camera exposure time and with the soft x-ray beam only, using the spectrum without the target gas as a background. The resultant spectrum of the parent molecule averaged over 64 such sets (64000 pulses in total with gas, 64000 without) for improved statistics, is then calculated according to the Beer-Lambert law where:

$$\text{Absorbance}_{\text{target gas}} = -\log_{10} \frac{\text{flux}_{\text{x-ray}}(\text{with gas})}{\text{flux}_{\text{x-ray}}(\text{without gas})}$$

A transient absorption spectrum is recorded with one second of camera exposure time with both the pump UV and the probe soft x-ray beam, the delay time between which is controlled by a motorized stage to be at 1000 fs (UV preceding x-ray), using the absorption spectrum without the pump UV beam as a background. The change between the two yields a transient spectrum where

$$\Delta\text{Absorbance}_{\text{target gas, delay timepoint}} = -\log_{10} \frac{\text{flux}_{\text{x-ray}}(\text{with gas, with UV})}{\text{flux}_{\text{x-ray}}(\text{with gas, without UV})}$$

and averaged over at least 32 such sets (32000 pulses with UV, 32000 pulses without UV at each time delay point) for statistics.

The energy scale for all spectra are calibrated using known core-to-valence transitions in argon and allyl radical. The spectral resolution is determined to be 360±20 meV by the Gaussian broadening of the $2p_{3/2}\rightarrow4s$ transition in argon[19] to match the observed spectra, assuming the core-hole lifetime broadening is 120 meV. The temporal resolution is estimated to be 90±10 fs based on the ponderomotive shift of the $2p_{3/2}\rightarrow4s$ transition in argon.

The core ionization potentials and valence ionization energies are all computed by Katherine Oosterbaan in Professor Martin Head-Gordon's group at University of California, Berkeley using time-dependent density functional theory (TDDFT) with the cc-pcvdz basis set[20] and the SRC1-R1 functional.[21-27]

4.3 Results and Discussion

4.3.1 Static Soft X-Ray Absorption Spectra of Methyl Iodide, Ethyl Iodide, Isopropyl Iodide and Tert-Butyl Iodide

Representative soft x-ray absorption spectra of methyl iodide, ethyl iodide, isopropyl iodide and tert-butyl iodide at the carbon K edge are shown in Figure 4.2, 4.3, 4.4 and 4.5, respectively. The absorption spectrum of methyl iodide is available in the literature for comparison where peak 1 at 285.6 ± 0.1 eV is assigned to the C(1s)→σ*(C-I) transition, peak 2 at 287.8 ± 0.1 eV to the combination of C(1s)→6sa$_1$ and/or C(1s)→σ*(C-H) and peak 3 at 288.9 ± 0.1 eV to the combination of C(1s)→6p$_e$ and 6p$_e$+ν(C-H).[28-29] The peak positions are well aligned with literature values, which verifies the accuracy of energy calibration. As the functional group attached to the iodine atoms gets more substituted, the number of bonds, molecular orbitals and hence possible core-level transitions also increases. Therefore it is diagnostic to inspect the C(1s)→σ*(C-I) transition in different iodides in order to gain a perspective into substitution effects on the central carbon.

Table 4.2 Summary of the C(1s)→σ*(C-I) transitions and the calculated C 1s ionization potentials (IPs) of the iodides.

Molecule	C(1s)→σ*(C-I)	Computed IP of the central carbon by TDDFT
Methyl Iodide	285.6 ± 0.1 eV	293.3 eV
Ethyl Iodide	285.7 ± 0.1 eV	293.2 eV
Isopropyl Iodide	285.8 ± 0.1 eV	293.0 eV
Tert-Butyl Iodide	286.0 ± 0.1 eV	293.2 eV

Based on the similarity of the iodides, peaks 4, 5 and 6 are assigned to the C(1s)→σ*(C-I) transitions in ethyl iodide, isopropyl iodide and tert-butyl iodide, respectively. Table 4.2 summarizes the energy at which each transition occurs. The peaks in methyl and ethyl iodide are fit with Gaussian functions as they are fairly separated from the onset of core photoionization. However, in the case of isopropyl iodide and tert-butyl iodide, the peaks are convoluted with core photoionization whose onset is not obvious. Therefore only the peak positions are reported in Table 4.2.

Comparing the positions of the C(1s)→σ*(C-I) transitions across the iodides, there is a small shift toward higher energy as the central carbon is more substituted. However, as the peaks in isopropyl iodide and tert-butyl iodide are both riding on the carbon 1s photoionization whose onset is yet to be determined, they can be slightly overestimated in their energies. Based on the experimental values in Table 4.1, methyl substitution will lead to a shift of at most 0.1 eV/methyl group. Additionally, the TDDFT computations on the carbon 1s ionization potentials show that there is indeed a very small difference across the series of methylsubstituted iodides. To our knowledge, there are no experimental results on the core ionization potentials of these iodides for comparison other than methyl iodide (291.8 eV)[28-29], so the computed carbon 1s ionization

energies might be 1.5 eV higher than the experimental ones and only the relative difference across the species should be used for comparison.

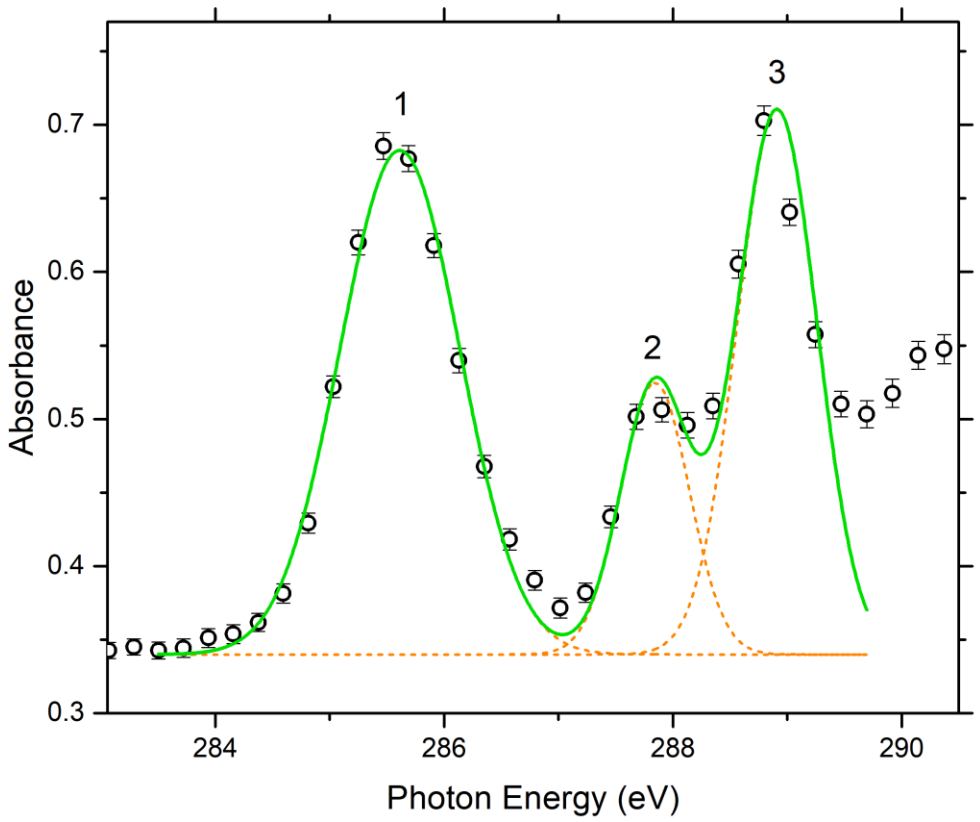

Figure 4.2 Static absorption spectrum of methyl iodide at the carbon K edge. The orange dash lines represent Gaussian fits to the peaks and the green solid line is the summation of all the fitted peaks.

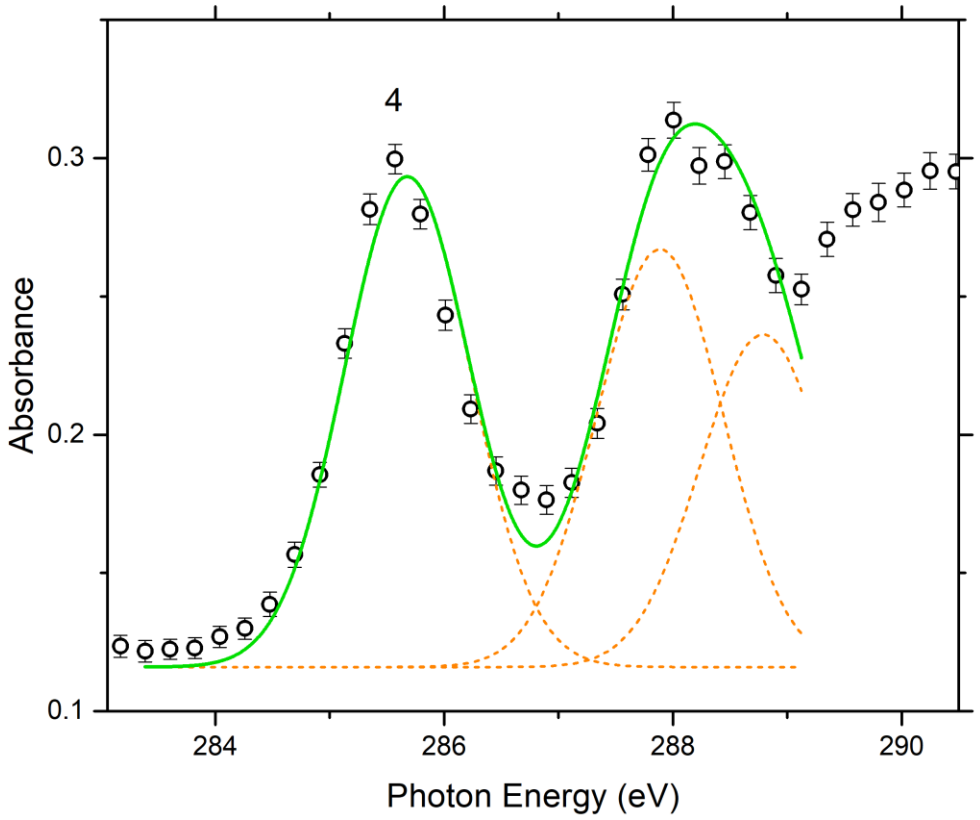

Figure 4.3 Static absorption spectrum of ethyl iodide at the carbon K edge. The orange dash lines represent Gaussian fits to the peaks and the green solid line is the summation of all the fitted peaks.

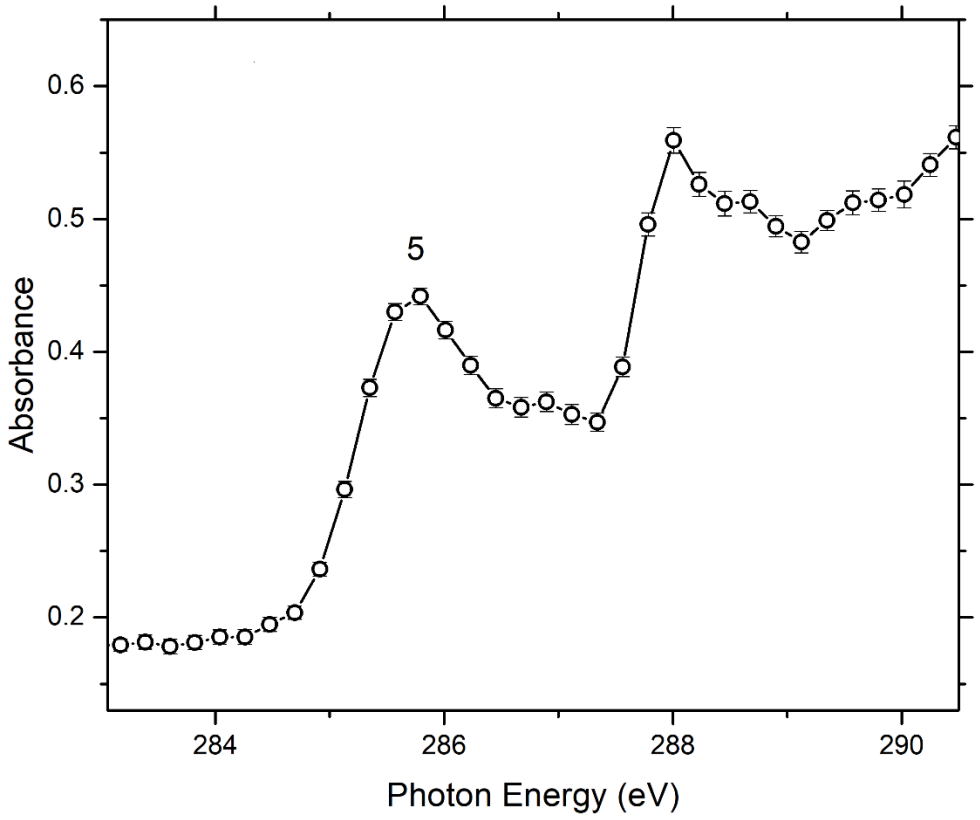

Figure 4.4 Static absorption spectrum of isopropyl iodide at the carbon K edge. Peak 5, the peak corresponding to the carbon 1s→SOMO transition is convoluted with core photoionization whose onset is yet to be determined and thus the peak is not fitted.

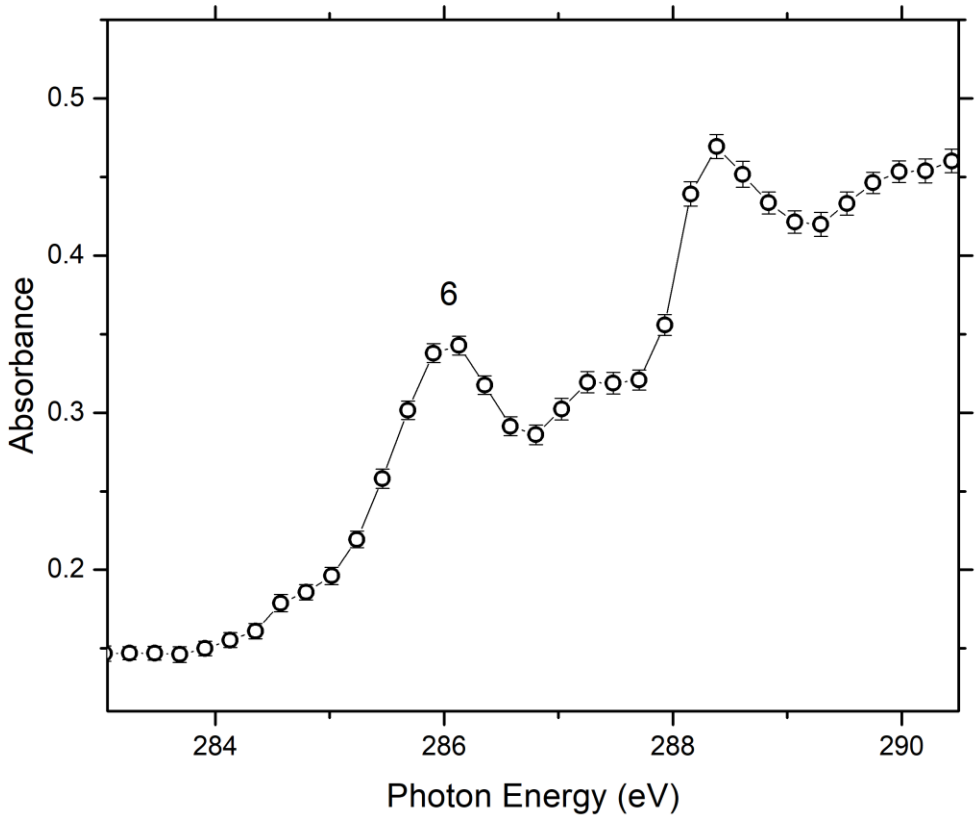

Figure 4.5 Static absorption spectrum of tert-butyl iodide at the carbon K edge. Peak 6, the peak corresponding to the carbon 1s→SOMO transition is convoluted with core photoionization whose onset is yet to be determined and thus the peak is not fitted.

4.3.2 Transient Absorption Spectra of Methyl Iodide, Ethyl Iodide, Isopropyl Iodide and Tert-Butyl Iodide Under UV Radiation

Representative transient absorption spectra of methyl iodide, ethyl iodide, isopropyl iodide and tert-butyl iodide at the carbon K edge are shown in Figure 4.6, 4.7, 4.8 and 4.9, respectively. Positive-going features represent new species that occur when UV light excites and dissociates the parent molecules and negative features indicate changes in the static spectrum when the parent molecules are depleted by UV excitation.

A new strong positive feature in the carbon K edge region is observed at 281.4±0.1 eV (peak 7) in methyl iodide, 281.7±0.1 eV (peak 10) in ethyl iodide, 282.2±0.1 eV (peak 13) in isopropyl iodide and 282.6±0.1 eV (peak 16) in tert-butyl. Each peak is also accompanied with a weaker peak at higher energy (peaks 8, 11, 14, 17), which is assigned by studies at higher UV power (blue lines in Figure 4.7-10) to result from multiphoton effects, possibly ionization of the parent molecules. The values are summarized in Table 4.3.

Table 4.3 Summary of the C(1s)→SOMO transitions in the substituted radicals.

Molecule	C(1s)→SOMO	Relative difference compared to $\cdot CH_3$
Methyl radical	281.4 eV ±0.1	0 eV
Ethyl radical	281.7 eV ±0.1	0.3 eV
Isopropyl radical	282.2 eV ±0.1	0.8 eV
Tert-butyl radical	282.6 eV ±0.1	1.2 eV

The photodissociation of all the iodides shown here at 266 nm is dominated by direct dissociation when an iodine 5p electron is promoted to the σ*(C-I) orbital, leading to electronically repulsive states and photodissociation products of a radical and I or I*.[30-32] Along the photodissociation coordinate, the σ*(C-I) orbital is broken into nonbonding I 5p and a new SOMO on the central carbon in the radical. Peaks 7, 10, 13 and 16 are thus attributed to the transition of C(1s) → SOMO in the methyl, ethyl, isopropyl, and tert-butyl radical, respectively. In methyl, the SOMO resembles the atomic carbon 2p orbital and the peak position reported here is very close to the result from CH_3 radical produced from flash pyrolysis of azomethane (281.3 eV).[33] The peak contains a vibrational sub-structure (on its right shoulder) that cannot be fully resolved with the current spectral resolution. All the C(1s) → SOMO transitions have an amplitude that is about twice as much as the depletion amplitude of the C(1s)→σ*(C-I) transitions (peaks 9, 12, 15 and 18), which suggests that the SOMOs in the substituted radicals may retain strong p character.

Based on the peak positions, the tert-butyl radical has a carbon 1s→SOMO transition 1.2 eV higher than the methyl radical, which is in sharp contrast to the small shift in the carbon 1s→σ*(C-I) transitions across the parent iodides. This poses an intriguing question on the character of the SOMOs as well as the carbon 1s orbitals, since a core-level transition involves both orbitals.

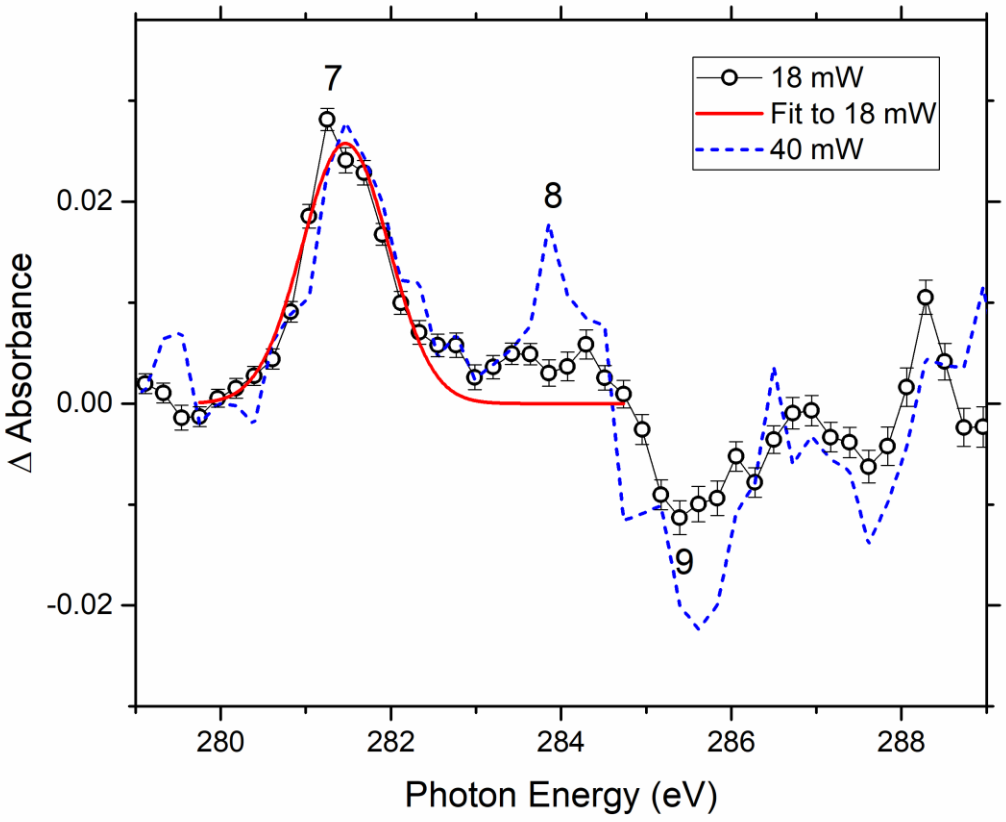

Figure 4.6 Transient absorption spectrum of methyl iodide under UV radiation. The black circles are the experimental values measured at a low UV power, the red line is the fit to the experimental peak and the blue dash line is the result at a much higher UV power.

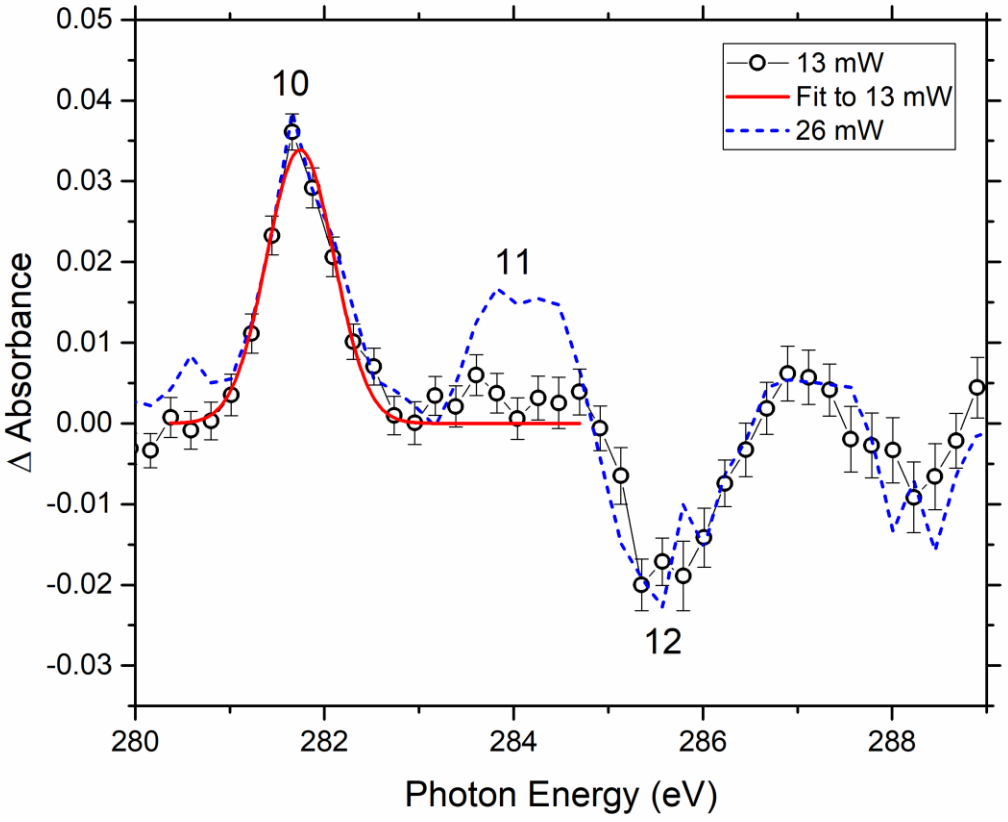

Figure 4.7 Transient absorption spectrum of ethyl iodide under UV radiation. The black circles are the experimental values measured at a low UV power, the red line is the fit to the experimental peak and the blue dash line is the result at a much higher UV power.

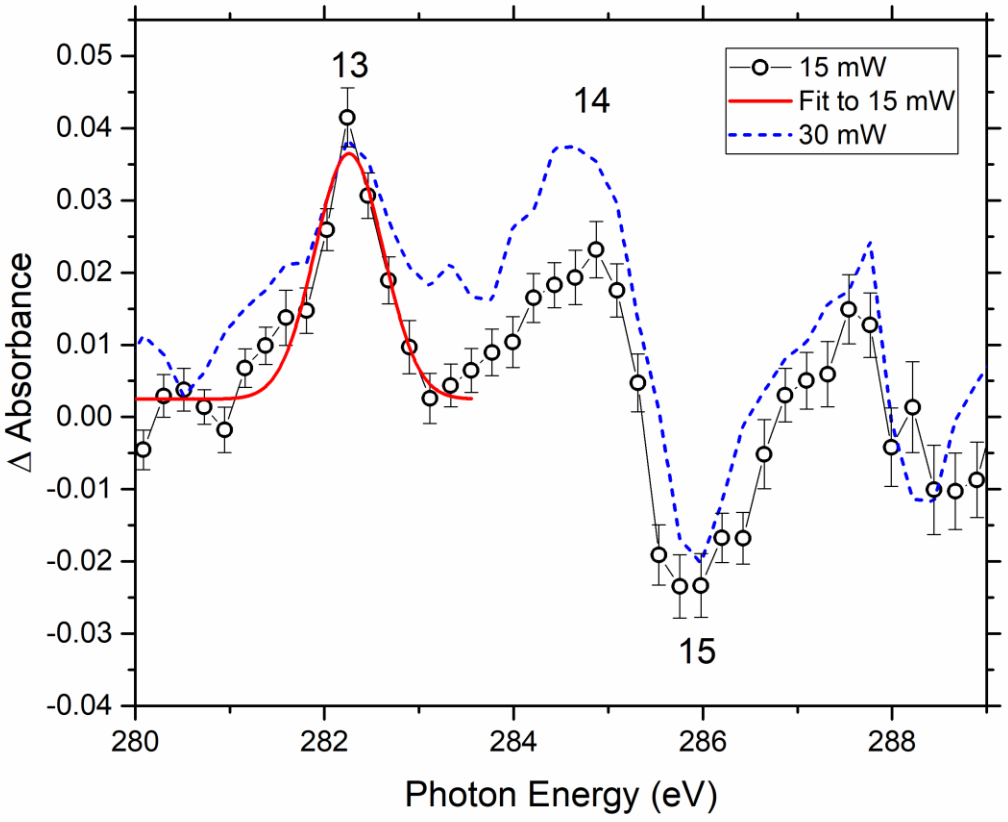

Figure 4.8 Transient absorption spectrum of isopropyl iodide under UV radiation. The black circles are the experimental values measured at a low UV power, the red line is the fit to the experimental peak and the blue dash line is the result at a much higher UV power.

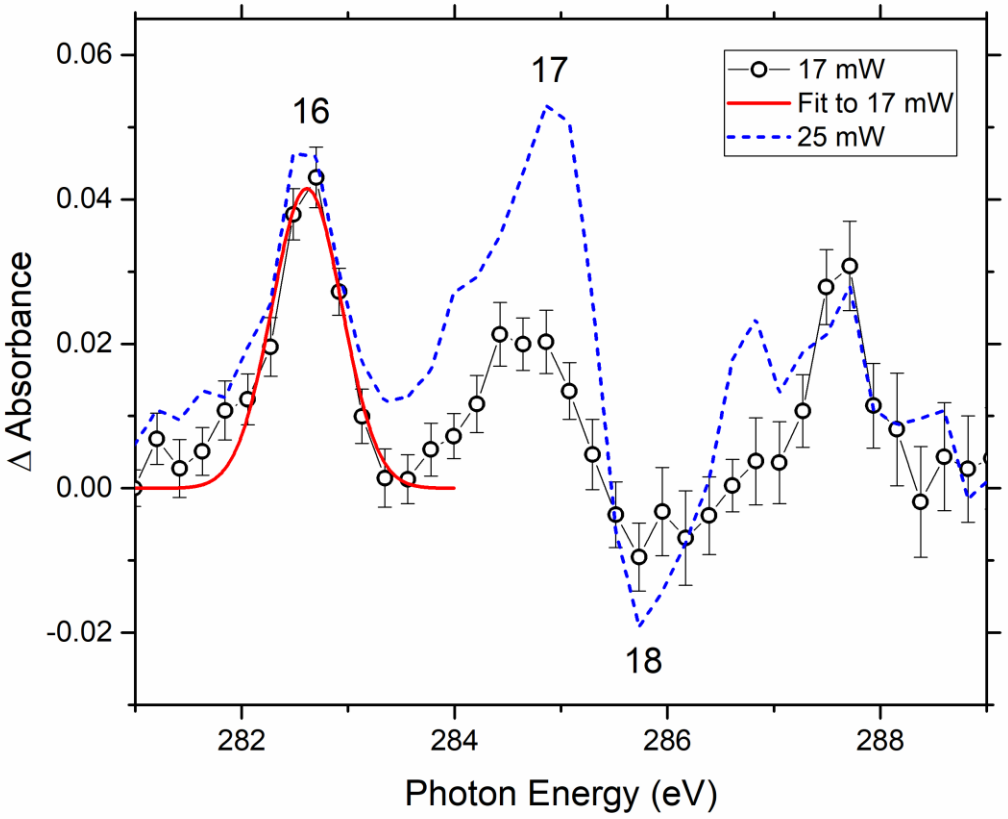

Figure 4.9 Transient absorption spectrum of tert-butyl iodide under UV radiation. The black circles are the experimental values measured at a low UV power, the red line is the fit to the experimental peak and the blue dash line is the result at a much higher UV power.

Hyperconjugation is an effect that is well known to stabilize the radicals by conjugating neighboring σ(C-H) orbitals with the atomic 2p orbital, stabilizing σ(C-H) and destabilizing the carbon 2p orbital, as shown in Figure 4.10.[6, 34] Thus the SOMOs of substituted radicals may be attenuated by such an effect and they will differ from a pure atomic 2p orbital. However, currently there is no good measure of how strong this effect is in modifying the orbital energy of a SOMO.

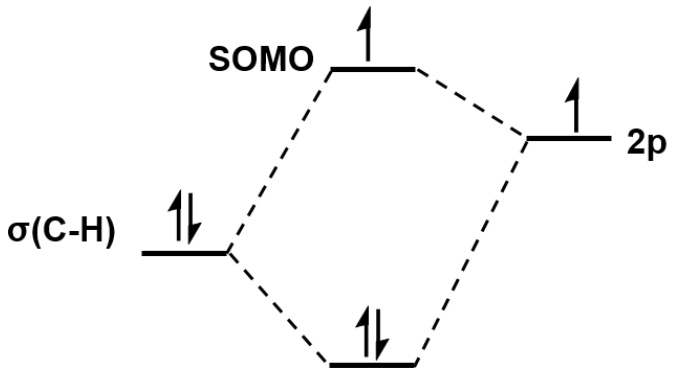

Figure 4.10 A schematic diagram showing the hyperconjugation effect.

Traditionally, the stability of a radical is compared by the radical stabilization energy (RSE) given by:[35]

$$RSE_H[R\cdot] = D[CH_3–H] - D[R–H] \text{ or } RSE_{Et}[R\cdot] = 1/2(D[CH_3–CH_3] - D[R–R])$$

where RSE_H and RSE_{Et} are different reference standards to define stability and D represents the bond dissociation energy. The tert-butyl radical, which is the most stabilized radical in this series, has an RSE_{Et} of 0.3 eV.[35] This measure compares how much energy is released when a radical forms a new bond and is not conclusive about how much the frontier SOMO orbital is different from an atomic 2p orbital, since it is heavily dependent on the new bond that is being formed.

On the other hand, by comparing the experimental valence ionization energy of the radicals where the methyl radical is measured at 9.84 eV and the tert-butyl radical at 6.7 eV,[5] the SOMO energy can possibly vary dramatically across the series, up to 2.1 eV from the methyl to the tert-butyl radical, although these ionization energies are complicated by the structures in the ionic states.

The C(1s)→SOMO transitions could be taken as a new way to measure the stabilization of the SOMO compared to the reference methyl radical. However, there are several limitations in directly drawing conclusions on the strength of hyperconjugation in modifying the SOMO. Two such factors are the Franck-Condon principle between the ground state and the core state and vibrational excitation from photodissociation.

As previous other studies have shown, there can be vibrational structure hidden in the broad peak shape of the radical, e.g. in the case of methyl radical, the right shoulder of the main peak is broadened due to a vibrational progression on the core excited state and the energy gap between the two vibrational bands has been resolved to be 0.4 eV in a previous study.[36] Therefore a broadening due to Franck-Condon overlaps is likely possible for substituted radicals and the peak position could correspond not to 0→0 transitions, but some other higher vibrationally core excited states, as the peak shapes in the substituted radicals, especially in the isopropyl and the tert-butyl radical, are not symmetric and visibly broadened on the left shoulder, as compared in Figure 4.11.

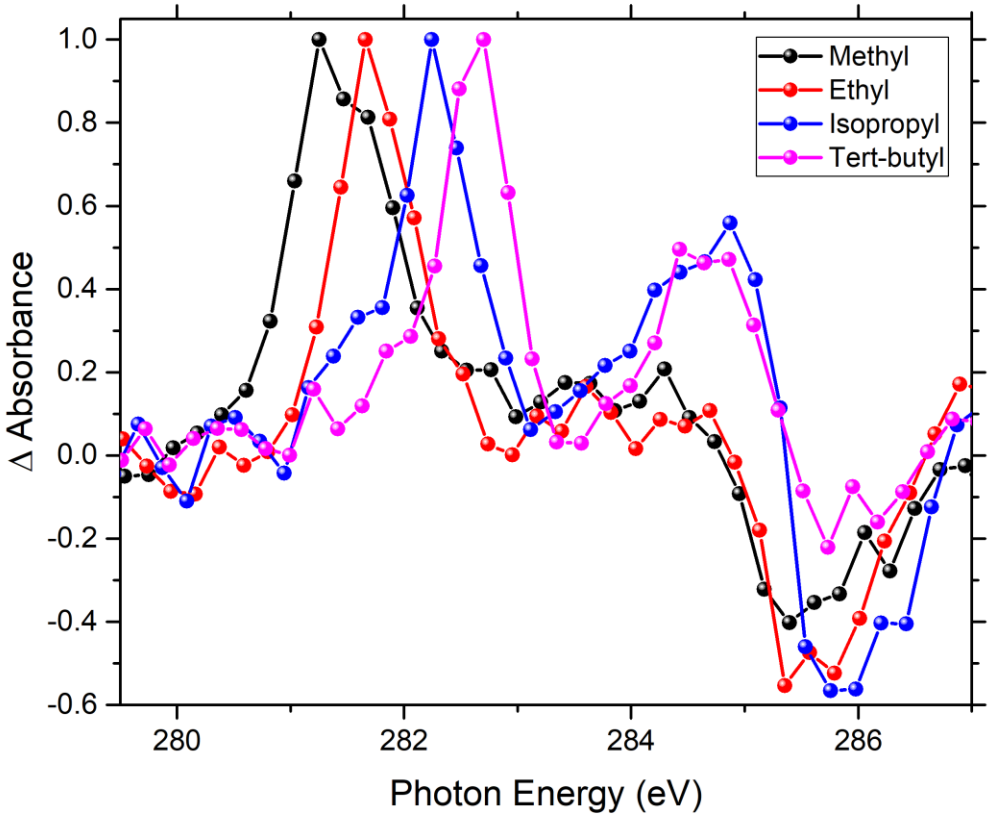

Figure 4.11 A comparison of the peak shapes of all the substituted radicals.

Apart from the Franck-Condon principle, there is also the possibility that the radicals produced from photodissociation carry vibrational excitation, which has been demonstrated in previous studies where a methyl radical produced from 266 nm photodissociation of methyl iodide can be excited into an umbrella motion.[37-38] As the series progresses toward more substituted radicals, there are more vibrational modes available and there is significant energy left in internal excitation after photodissociation.[30-31] These vibrational modes can possibly change the overlap between the ground state and the core-excited state, impacting the observed peak positions. Further theoretical investigations on the vibrational modes of the radicals produced from photodissociation along with their core-excited states would be required in order to deconvolute these effects.

Nevertheless, the TDDFT computations on the vertical core ionization energies and the vertical valence ionization energies (as shown in Table 4.4) can possibly give another explanation to the difference observed in the C(1s)→SOMO transitions. As shown in Figure 4.12, assuming the ionic state from the valence ionization and from the core ionization are close in the structure, the C(1s)→SOMO transition can be approximated as the difference between the valence vertical ionization energy and core vertical ionization energy. Using this method, as Table 4.4 shows, the relative difference across the series is very close to the experimental values (Table 4.3). The

TDDFT computations on the valence ionization energies are very similar to the experimental values mentioned earlier, although in general 0.2 eV lower, which shows that the SOMO is greatly affected by methyl substitution. Moreover, in contrast to the core ionization energies computed in the parent molecules as in Table 4.2 where there is only a small shift across various substituted iodides, radicals are also much more affected by the energy value of the core orbitals due to substitution. The two changes, combined together, make up the overall difference in the C(1s)→SOMO transitions.

Table 4.4 Summary of the carbon 1s ionization potentials (IP) and valence ionization potentials in the substituted radicals using the TDDFT methods.

Molecule	C 1s IP	Valence IP	Core IP - Valence IP	Relative difference compared to $\cdot CH_3$
Methyl Radical	293.8 eV	9.6 eV	284.2 eV	0 eV
Ethyl Radical	293.2 eV	8.4 eV	284.8 eV	0.4 eV
Isopropyl Radical	292.7 eV	7.6 eV	285.1 eV	0.9 eV
Tert-Butyl Radical	292.5 eV	7.0 eV	285.5 eV	1.1 eV

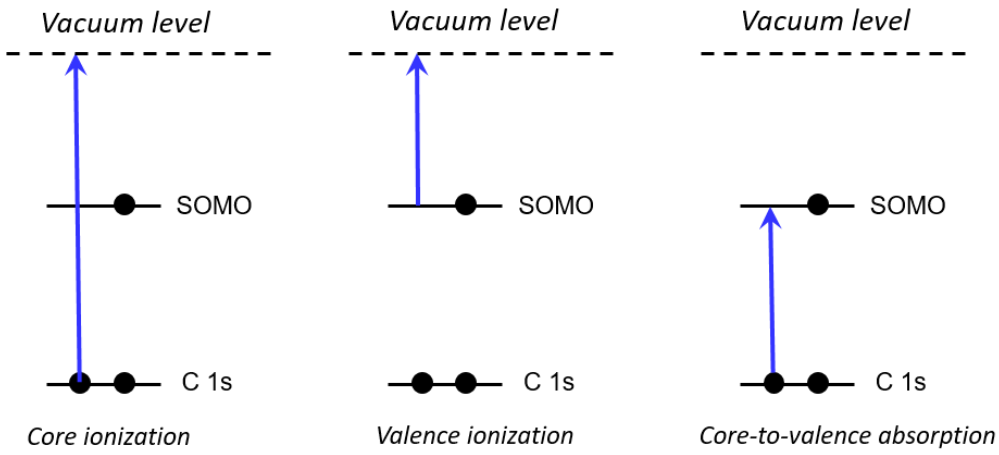

Figure 4.12 A schematic diagram to show a potential way to calculate the C(1s)→SOMO transitions using the core ionization and the valence ionization energies.

4.4 Conclusions

Methyl, ethyl, isopropyl and tert-butyl iodide have been used to produce the methyl, ethyl, isopropyl and tert-butyl radical through photodissociation at 266 nm and the SOMOs of the radicals have been probed from the carbon K edge. While substitution only induces a small shift in the characteristic C(1s)→σ*(C-I) transitions in the parent molecules, the C(1s)→SOMO

transitions demonstrate much more dramatic differences from the methyl to the tert-butyl radical. This difference could be understood as a convolution of an elevated SOMO by the hyperconjugation effect and vibrational excitation in the ground state or the core-excited state of the radicals. The TDDFT computations on the core ionization potentials show that while the parent molecules are only slightly affected by alkyl substitution (<0.3 eV), the radicals can be modified to a much greater degree in the core ionization potentials based on the TDDFT computations. The results point to new directions for core-level theoretical investigations.

4.5 Acknowledgement

I would like to acknowledge Katherine Oosterbaan and Professor Martin Head-Gordon for performing the computations and discussion of this project.

4.6 Bibliography

1. Pilling, M. J., Radical-radical reactions. *Annual Review of Physical Chemistry* **1996,** *47*, 81-108.
2. Cunningham, M. F., Controlled/living radical polymerization in aqueous dispersed systems. *Prog Polym Sci* **2008,** *33* (4), 365-398.
3. Hicks, R. G., What's new in stable radical chemistry? *Org Biomol Chem* **2007,** *5* (9), 1321-1338.
4. Studer, A.; Curran, D. P., Catalysis of Radical Reactions: A Radical Chemistry Perspective. *Angew Chem Int Edit* **2016,** *55* (1), 58-102.
5. Houle, F. A.; Beauchamp, J. L., Photoelectron-Spectroscopy of Methyl, Ethyl, Isopropyl, and Tert-Butyl Radicals - Implications for the Thermochemistry and Structures of the Radicals and Their Corresponding Carbonium-Ions. *J Am Chem Soc* **1979,** *101* (15), 4067-4074.
6. Fleming, I., *Molecular Orbitals and Organic Chemical Reactions*. Student ed.; John Wiley & Sons: Chichester, U.K., 2009.
7. Dyke, J.; Ellis, A.; Jonathan, N.; Morris, A., Vacuum Ultraviolet Photoelectron-Spectroscopy of Transient Species .18. The Cyclopropyl, Isopropyl and Normal-Propyl Radicals. *J Chem Soc Farad T 2* **1985,** *81* (Oct), 1573-1586.
8. Dyke, J. M.; Ellis, A. R.; Keddar, N.; Morris, A., A Reinvestigation of the 1st Band in the Photoelectron-Spectrum of the Ethyl Radical. *J Phys Chem-Us* **1984,** *88* (12), 2565-2569.
9. Parkes, D. A., The Ultraviolet-Absorption Spectra of the Acetyl Radical and the Kinetics of the CH_3+CO Reaction at Room-Temperature. *Chem Phys Lett* **1981,** *77* (3), 527-532.
10. Attar, A. R.; Bhattacherjee, A.; Pemmaraju, C. D.; Schnorr, K.; Closser, K. D.; Prendergast, D.; Leone, S. R., Femtosecond x-ray spectroscopy of an electrocyclic ring-opening reaction. *Science* **2017,** *356* (6333), 54-58.
11. Bhattacherjee, A.; Das Pennaraju, C.; Schnorr, K.; Attar, A. R.; Leone, S. R., Ultrafast Intersystem Crossing in Acetylacetone via Femtosecond X-ray Transient Absorption at the Carbon K-Edge. *J Am Chem Soc* **2017,** *139* (46), 16576-16583.
12. Pertot, Y.; Schmidt, C.; Matthews, M.; Chauvet, A.; Huppert, M.; Svoboda, V.; von Conta, A.; Tehlar, A.; Baykusheva, D.; Wolf, J. P.; Worner, H. J., Time-resolved x-ray absorption spectroscopy with a water window high-harmonic source. *Science* **2017,** *355* (6322), 264-+.

13. Eden, S.; Limao-Vieira, P.; Hoffmann, S. V.; Mason, N. J., VUV spectroscopy of CH_3Cl and CH_3I. *Chem Phys* **2007,** *331* (2-3), 232-244.
14. Boschi, R. A.; Salahub, D. R., Far Ultraviolet-Spectra of Some Branched-Chain Iodo-Alkanes, Iodo-Cyclo-Alkanes, Fluoro-Iodo-Alkanes and Iodo-Alkenes. *Mol Phys* **1972,** *24* (4), 735-&.
15. Rattigan, O. V.; Shallcross, D. E.; Cox, R. A., UV absorption cross-sections and atmospheric photolysis rates of CF_3I, CH_3I, C_2H_5I and CH_2ICl. *J Chem Soc Faraday T* **1997,** *93* (16), 2839-2846.
16. Jenkin, M. E.; Murrells, T. P.; Shalliker, S. J.; Hayman, G. D., Kinetics and Product Study of the Self-Reactions of Allyl and Allyl Peroxy-Radicals at 296-K. *J Chem Soc Faraday T* **1993,** *89* (3), 433-446.
17. Bhattacherjee, A.; Attar, A. R.; Leone, S. R., Transition state region in the A-Band photodissociation of allyl iodide-A femtosecond extreme ultraviolet transient absorption study. *J Chem Phys* **2016,** *144* (12).
18. Rubio-Lago, L.; Garcia-Vela, A.; Arregui, A.; Amaral, G. A.; Banares, L., The photodissociation of CH_3I in the red edge of the A-band: Comparison between slice imaging experiments and multisurface wave packet calculations. *J Chem Phys* **2009,** *131* (17).
19. King, G. C.; Tronc, M.; Read, F. H.; Bradford, R. C., Investigation of Structure near $L_{2,3}$ Edges of Argon, $M_{4,5}$ Edges of Krypton and $N_{4,5}$ Edges of Xenon, Using Electron-Impact with High-Resolution. *J Phys B-at Mol Opt* **1977,** *10* (12), 2479-2495.
20. Pople, J. A.; Gill, P. M. W.; Johnson, B. G., Kohn-Sham Density-Functional Theory within a Finite Basis Set. *Chem Phys Lett* **1992,** *199* (6), 557-560.
21. Besley, N. A.; Peach, M. J. G.; Tozer, D. J., Time-dependent density functional theory calculations of near-edge X-ray absorption fine structure with short-range corrected functionals. *Phys Chem Chem Phys* **2009,** *11* (44), 10350-10358.
22. Roper, I. P. E.; Besley, N. A., The effect of basis set and exchange-correlation functional on time-dependent density functional theory calculations within the Tamm-Dancoff approximation of the x-ray emission spectroscopy of transition metal complexes. *J Chem Phys* **2016,** *144* (11).
23. Besley, N. A.; Noble, A., Time-dependent density functional theory study of the X-ray absorption spectroscopy of acetylene, ethylene, and benzene on Si(100). *J Phys Chem C* **2007,** *111* (8), 3333-3340.
24. Stener, M.; Fronzoni, G.; de Simone, M., Time dependent density functional theory of core electrons excitations. *Chem Phys Lett* **2003,** *373* (1-2), 115-123.
25. George, S. D.; Petrenko, T.; Neese, F., Time-dependent density functional calculations of ligand K-edge X-ray absorption spectra. *Inorg Chim Acta* **2008,** *361* (4), 965-972.
26. Ekstrom, U.; Norman, P., X-ray absorption spectra from the resonant-convergent first-order polarization propagator approach. *Phys Rev A* **2006,** *74* (4).
27. Ekstrom, U.; Norman, P.; Carravetta, V., Relativistic four-component static-exchange approximation for core-excitation processes in molecules. *Phys Rev A* **2006,** *73* (2).
28. Hitchcock, A. P.; Brion, C. E., Inner Shell Excitation of CH_3F, CH_3Cl, CH_3Br and CH_3I by 2.5 Kev Electron-Impact. *J Electron Spectrosc* **1978,** *13* (3), 193-218.
29. Hitchcock, A. P.; Brion, C. E., Assignment of the Carbon K-Shell Spectra of the Methyl Halides. *J Electron Spectrosc* **1979,** *17* (3), 139-147.

30. Phillips, D. L.; Lawrence, B. A.; Valentini, J. J., Substituent Effects on Gas-Phase Photodissociation Dynamics - Resonance Raman-Spectra of Ethyl Iodide, Isopropyl Iodide, and Tert-Butyl Iodide. *J Phys Chem-Us* **1991,** *95* (23), 9085-9091.
31. Kim, Y. S.; Kang, W. K.; Kim, D. C.; Jung, K. H., Photodissociation of tert-butyl iodide at 277 and 304 nm: Evidence for direct and indirect dissociation in A-band photolysis of alkyl iodide. *J Phys Chem A* **1997,** *101* (41), 7576-7581.
32. Riley, S. J.; Wilson, K. R., Excited Fragments from Excited Molecules - Energy Partitioning in Photodissociation of Alkyl Iodides. *Faraday Discuss* **1972,** *53*, 132-146.
33. Alagia, M.; Bodo, E.; Decleva, P.; Falcinelli, S.; Ponzi, A.; Richter, R.; Stranges, S., The soft X-ray absorption spectrum of the allyl free radical. *Phys Chem Chem Phys* **2013,** *15* (4), 1310-1318.
34. Alabugin, I. V.; Gilmore, K. M.; Peterson, P. W., Hyperconjugation. *Wires Comput Mol Sci* **2011,** *1* (1), 109-141.
35. Coote, M. L.; Lin, C. Y.; Zavitsas, A. A., Inherent and transferable stabilization energies of carbon-and heteroatom-centred radicals on the same relative scale and their applications. *Phys Chem Chem Phys* **2014,** *16* (18), 8686-8696.
36. Alagia, M.; Lavollee, M.; Richter, R.; Ekstrom, U.; Carravetta, V.; Stranges, D.; Brunetti, B.; Stranges, S., Probing the potential energy surface by high-resolution x-ray absorption spectroscopy: The umbrella motion of the core-excited CH_3 free radical. *Phys Rev A* **2007,** *76* (2).
37. Eppink, A. T. J. B.; Parker, D. H., Energy partitioning following photodissociation of methyl iodide in the A band: A velocity mapping study. *J Chem Phys* **1999,** *110* (2), 832-844.
38. Baughcum, S. L.; Leone, S. R., Photofragmentation Infrared-Emission Studies of Vibrationally Excited Free-Radicals CH_3 and CH_2I. *J Chem Phys* **1980,** *72* (12), 6531-6545.